

INFORMATION TO USERS

This manuscript has been reproduced from the microfilm master. UMI films the text directly from the original or copy submitted. Thus, some thesis and dissertation copies are in typewriter face, while others may be from any type of computer printer.

The quality of this reproduction is dependent upon the quality of the copy submitted. Broken or indistinct print, colored or poor quality illustrations and photographs, print bleedthrough, substandard margins, and improper alignment can adversely affect reproduction.

In the unlikely event that the author did not send UMI a complete manuscript and there are missing pages, these will be noted. Also, if unauthorized copyright material had to be removed, a note will indicate the deletion.

Oversize materials (e.g., maps, drawings, charts) are reproduced by sectioning the original, beginning at the upper left-hand corner and continuing from left to right in equal sections with small overlaps.

ProQuest Information and Learning
300 North Zeeb Road, Ann Arbor, MI 48106-1346 USA
800-521-0600

UMI[®]

Intraoperative Ultrasound Imaging for the Detection and Correction of Tissue Movement in Image-guided Neurosurgery

By

Roch Comeau

Department of Biomedical Engineering
McGill University, Montréal
April, 2000

A Thesis Submitted to the
Faculty of Graduate Studies and Research
in Partial Fulfillment of the Requirements for the Degree of

Doctor of Philosophy

©Roch Comeau, 2000



**National Library
of Canada**

**Acquisitions and
Bibliographic Services**

**395 Wellington Street
Ottawa ON K1A 0N4
Canada**

**Bibliothèque nationale
du Canada**

**Acquisitions et
services bibliographiques**

**395, rue Wellington
Ottawa ON K1A 0N4
Canada**

Your file Votre référence

Our file Notre référence

The author has granted a non-exclusive licence allowing the National Library of Canada to reproduce, loan, distribute or sell copies of this thesis in microform, paper or electronic formats.

The author retains ownership of the copyright in this thesis. Neither the thesis nor substantial extracts from it may be printed or otherwise reproduced without the author's permission.

L'auteur a accordé une licence non exclusive permettant à la Bibliothèque nationale du Canada de reproduire, prêter, distribuer ou vendre des copies de cette thèse sous la forme de microfiche/film, de reproduction sur papier ou sur format électronique.

L'auteur conserve la propriété du droit d'auteur qui protège cette thèse. Ni la thèse ni des extraits substantiels de celle-ci ne doivent être imprimés ou autrement reproduits sans son autorisation.

0-612-69861-0

Canada

Abstract

Pre-operative image based image guided neurosurgery (IGNS) systems involve the mapping of intraoperative real world coordinates and trajectories to one or more pre-operative image data spaces. This is accomplished using a rigid body transformation from patient to image coordinate systems, which is usually obtained by identifying external landmarks on the patient and on the images, and employing a least squares minimization technique. The validity of the rigid body transformation relies on the assumption that the patient and localizing device form a completely rigid body for the duration of the procedure. It has been observed that the brain tissue moves significantly within the skull, particularly after large open craniotomies, violating this assumption of rigidity.

A surgical guidance system has been developed that combines pre-operative image information (e.g. MRI or CT) and intraoperative ultrasound imaging to detect brain tissue deformation during IGNS. The system includes hardware and software to track the ultrasound transducer during image acquisition, and visualization software to view the live ultrasound and co-planar MRI images. The software includes tools to delineate structures in either modality and overlay these images on one another, and warp the pre-operative image based on the delineated structures.

The thesis includes a discussion of techniques, instruments and results, using a novel calibration tool and a multi-modality deformable phantom. Finally, the clinical experience from the use of this system in the operating room are presented.

Résumé

La neurochirurgie guidée par imagerie, basée sur images préopératoires, implique la relation entre coordonnées et trajectoires intraopératoires réelles et le ou les espaces-image(s) préopératoires. Ceci est effectué par l'entremise d'une transformée rigide du patient au référentiel image, que l'on obtient habituellement en identifiant des repères externes sur le patient et sur les images, et en employant une minimization par le moindre des carrés. La validité de la transformée rigide s'appuie sur l'assomption que le patient et l'outil de localisation constituent un corps rigide pour la durée de la procédure. Or, il a été établi que le cerveau se déplace de façon significative, à l'intérieur du crâne, particulièrement après de crantomies béantes, violant cette assomption de rigidité.

Nous avons conçu un système de guidage chirurgical qui combine l'information préopératoire (ex.: IRM ou tomographie pas rayons X) et les images échographiques intraopératoires pour détecter la déformation du tissu nerveux pendant l'intervention chirurgicale. Le système inclut du matériel et du logiciel pour assurer le suivi du transducteur échographique pendant l'acquisition d'images, et du logiciel de visualisation pour visionner les images échographiques en direct ainsi que des images IRM coplanaires. Le logiciel comprend des outils pour délinéer les structures anatomiques dans l'une ou l'autre modalité, recouvrir ces images l'une sur l'autre, et recalcr de façon nonrigide l'image préopératoire en vertu de ces structures délinéées.

Cette thèse comprend une discussion des techniques, des instruments et des résultats, employant un nouvel outil de calibration et un phantôme déformable et utilisable avec diverses modalités. Enfin, l'expérience clinique intégrant ce système est présentée.

Original Contribution

This work contributes the following original ideas, methods and tools to IGNS:

- A novel design of a multimodality calibration phantom, which minimizes the error contribution from partial volume effects on the calibration of the US based IGNS system. The phantom also serves as a tool to evaluate the accuracy of the IGNS system in mapping intraoperative ultrasound image pixels to homologous pre-operative computed tomography or magnetic resonance images.
- A complete intraoperative US based IGNS system which incorporates novel designs that allow the surgeon to qualitatively and quantitatively compare the intraoperative and pre-operative images.
- Several display techniques to superimpose the deformation information on the pre-operative images, including a novel interactive region of interest (ROI) tool that allows the surgeon to easily and quickly compare the intraoperative and pre-operative images. The surgeon can qualitatively assess the extent of brain shift, and its effects on the accuracy of the pre-operative information, as well as to monitor the progress of the procedure. Point and line annotation tools were developed to manually identify homologous features in the pre and intraoperative images to allow quantitative information on the extent of brain shift to be acquired.
- A simple propagation and interpolation algorithm that uses the quantitative deformation information obtained using the point and line delineation tools to warp the pre-operative images to effectively correct them for the deformation.
- A novel multimodality deformable phantom to test the IGNS system's ability to visualize and correct for the deformation. The phantom can be imaged using magnetic resonance imaging to simulate pre-operative images, and using ultrasound to simulate

● intraoperative imaging. The phantom contains two hemispheres, each with simulated cortical surfaces, ventricles and blood vessels, all visible in both modalities.

Acknowledgements

I would like to thank Dr. Peters for his kind support, wisdom and friendship. Certainly his guidance and friendship has had, and will continue to have, a profound influence in my career.

I thank my parents, whose love and unquestioned support gave me the confidence to take on this challenge and succeed. I want to thank my sister Janet for her friendship and for being my organizational guru throughout this project. Also I thank my brother Jacques for his support and friendship.

I am grateful to the Radiology staff at the Montreal Neurological Institute and Hospital for their cooperation, insights into clinical Radiology, and for allowing me access to their equipment. I also thank the Neurosurgical staff at the Montreal Neurological Hospital for their cooperation and valuable assistance in the operating room.

I owe an even greater dept of thanks to the Neurosurgeons, particularly Dr. Abbas Sadikot and Dr. André Olivier for sharing their expertise and ideas, as well as showing great patience while allowing me into their operating room. I thank Dr. Mario Alonso for his friendship as well as his Neurosurgical wisdom.

I would like to thank everyone at the McConnell Brain Imaging Center, particularly Alexandre, Reza, Michel, Jeff, Lauren and Sridar for their friendship, editing help and insightful discussions in and out of the lab. I thank Rebecca for her assistance in editing this manuscript.

I would also like to thank the students and staff at the Robarts Research Institute for their help in the phantom design and construction.

Finally, I thank the Medical Research Council of Canada and the Natural Sciences and Engineering Research Council (NSERC) for financial support and Advanced Technology Laboratories (ATL) for supplying the ultrasound transducer used in this project.

List of Figures

Figure 2-1: Illustration of the concept of the stereotactic frame. A: A typical stereotactic frame: The Olivier-Bertrand-Tipal (OBT) frame, with imaging plates and tools attached. B: Illustration of the position of the ball-bearing fiducial marker configuration for 2D X-ray images. C: N-bar fiducial configuration for computed tomography or magnetic resonance imaging. 10

Figure 2-2: Design of the N-bar fiducial marker..... 11

Figure 2-3: Display of a computerized planning system used in the planning of the implantation of a deep brain stimulator into the globus pallidus for the treatment of Parkinson’s disease. Both Ventriculography and volumetric MRI are employed to calculate the position of the stimulator prior to implantation..... 12

Figure 2-4: Typical IGNS setup: A pointer is attached to a tracked tool holder; in this example, an LED array, whose position and orientation is monitored by a tracking device. The tracker frame-of-reference is assumed to be rigidly fixed to the head. A computer monitors the tracker and displays a representation of the tool within the image data. 14

Figure 2-5: Illustration of the coordinate systems and the transformations relating them to each other. Tools are attached to a tool holder, while the holder’s position and orientation are monitored by the tracking device and returned to a computer. The transformation from the tracking device to the image frame-of-reference is obtained by identifying homologous points on the patient with the pointer, and on the images with the computer mouse. 16

Figure 2-6: Typical six degree of freedom articulated arm (Faro Technologies, Lake Mary, FL). 18

Figure 2-7: Schematic illustration of the Polaris optical tracking system in use at our institution. A reference tracker is rigidly connected to the head fixation device to provide a rigid-body connection between the tracker and the patient’s skull. Using both the fixed reference tracker, and the tracked tool, one can calculate the position and orientation of the tool with respect to the reference tracker and thus the patient.20

Figure 2-8: Image of the VISLAN pointer. The tool includes a pattern object which can localized automatically using machine vision techniques.....22

Figure 2-9: Example of an IGNS system (Viewing Wand, ISG Technologies, Mississauga, ON) using volumetric CT data for the resection of a tumour in the spinal canal. Bottom right window shows a 3D reconstruction of the skull, spinal segments, spinal chord dura and tumour. Probe is shown touching the skull base. 24

Figure 2-10: A: Typical IGNS (ISG Viewing Wand) screen using Gadolinium enhanced MRI to highlight tumour nodules. Brain surface and tumour nodules were segmented and are displayed as colour coded surfaces in the bottom right view. B: Maximum intensity projection image of a magnetic resonance angiogram of a patient with an arterial venous malformation (arrow).26

Figure 2-11: Example of a PET image superimposed on an anatomical MRI data set for surgical guidance. Here, the surgeon wished to have the functional boundaries of the motor cortex delineated to help avoid it during the resection of a lesion.....28

Figure 2-12: Examples of physical and virtual tool coordinate spaces. A: A pointer has its tip as its coordinate space origin, which is physically attached to the tracker. B: Tracked ultrasound probe. The origin is based in the image, which can be treated mathematically as rigidly attached to the tracked transducer. C: Tracked intraoperative microscope. The origin is the focal point, which can also be regarded mathematically as being rigidly attached to the microscope lens.....32

Figure 2-13 Various fiducial marker strategies for IGNS. A: Bone and skin implanted markers. B: Bite-bar held fiducial marker array. C: Non-invasive re-locatable frame. D: Anatomical or skin bonded landmarks.37

Figure 2-14: Head fixation devices used in IGNS. A: Mayfield clamp which is used mainly for craniotomies. B: C-Arm, used for bi-lateral implantations of depth electrodes.40

Figure 2-15: Effect of brain tissue distortion on IGNS accuracy: A: After craniotomy, the probe is placed on the cortical surface, assuming no distortion of the brain tissue, the position of the pointer is accurately represented on the pre-operative image data. B: Brain tissue distortion: Here the brain has sagged after the craniotomy. This time, when the probe is brought to the surface of the brain, its position is incorrectly reported as inside the cortex. This is because the actual brain tissue has moved with respect to the external landmarks used for registration42

Figure 2-16: Fused video/MRI image of the author. The cortex can be seen within the head, and a tracked pointer can be seen touching the surface of the head. Using the stereo display, the sensation of depth improves the realism of the image.....44

Figure 2-17: Two examples of "open" magnets designed for interventional MRI procedures. A: General Electric double doughnut design. B: Marconi static field flat magnet design.....45

Figure 2-18: Illustration of the basic principle of ultrasound imaging. The transducer acts as both a transmitter and receiver. An ultrasound pulse is emitted at time A. At time B, the pulse encounters an acoustic interface, where it undergoes partial reflection. At time C, the attenuated pulse encounters a second interface. In the meantime, the first reflected pulse is measured by the transducer. Finally at time D, the second reflected pulse reaches the transducer. The received signals and the speed of sound in the medium are used to calculate reflector depths to generate an image.53

Figure 2-19: Intensity vs. depth curves for common frequencies (a=3.5MHz, b=5.0MHz, c=7.5MHz) used in ultrasound imaging, for soft tissue.¹⁰⁴ The depth at which the intensity is reduced by 50% is indicated.54

Figure 2-20: Illustration of the relationship between pulse length and axial resolution. A: The gap between the interfaces is less than half the spatial pulse length. The return echoes from the two interfaces overlap and cannot be distinguished from one another. B: The distance between the two interfaces is enough to ensure that the two returning echoes do not overlap and can be distinguished from one another.....55

Figure 2-21: Illustration of how a delay generator can steer and focus a beam using the array of crystals found in a small face phased array transducer.56

Figure 2-22: Illustration of how intraoperative US may be integrated into a typical IGNS system. The US image may be regarded as a virtual pointer, where the central axis of the image may be regarded as the pointer's axis. 57

Figure 2-23: Examples of common data overlay techniques applicable to superimposing intraoperative US onto co-planar pre-operative MRI. A: Original MRI image. B: MRI with a US image displayed within a box. A 50-50 blend is applied to prevent the US from completely obscuring the underlying MR image. A separate color is also used to help the viewer to distinguish between US and MR features. C: MRI with opaque US image (OR function) superimposed on the MR. While the underlying MR image is obscured, the image is less cluttered. D: MR image with a yellow curve representing the outline of the ventricle obtained from the US.....60

Figure 3-1: IGNS system organization as used in the operating room. Two independent computers and tracking devices are used to preserve a "gold standard" system. Both systems share the tracked pointer and reference object, while only the US based system monitors the tracked US transducer. 63

Figure 3-2: Typical screenshot of US based IGNS system with key software components highlighted.....65

Figure 3-3: Software organization chart.....66

Figure 3-4: Example of image processor objects. The volume data instance object supplies the raw voxel data for the 3 multi-planar reformat (MPR) image processors. The image processors also employ the volume cursor coordinate value to determine where the 3 orthogonal planes to render lie in the volume. The results are passed down the pipeline to the image view objects for display on the screen. 68

Figure 3-5: 2D and 3D image views. These objects coordinate the display of the image data and the display and user interaction with all other objects that require a representation on the images. They also manage the UI required to allow the user to manipulate the image display parameters..... 70

Figure 3-6: Registration Tool Interface..... 74

Figure 3-7: Multi-segmented Hermite polynomial using the Katmull Rom constraint. The tangent direction at each knot is parallel to the direction of the line between the neighboring knots. 76

Figure 3-8: Example of a seeded fill to identify the area that corresponds to brain in the MRI image. The boundary is defined using a closed multi-segmented Hermite polynomial..... 77

Figure 3-9: Example of the ROI overlay tool. A: Oblique view of an enhanced MRI showing enhancement of a tumour. B: Same oblique MRI with a rectangular portion of the co-planar US overlaid in the region of the tumour. In use, the window is able to "move" over the underlying image..... 78

Figure 3-10: Different display techniques to visualize the displacement grid. A: A non-deformed mesh superimposed on an oblique image of a deformable brain phantom. B: Grid after deformation. The deformation represents how an intraoperative image would have to deform to match the pre-operative image. If the node points were pinned to the underlying pre-operative image and returned to a regular straight grid, the pre-operative image would be warped to conform to the intraoperative image in the process. C: Vector field showing the direction each node should take to correct the image. D: Magnitude

display. Semi transparent colour coded display to appreciate the distribution of the magnitude of the deformation throughout the image.....	81
Figure 3-11: Example of an oblique MRI of the deformable brain phantom after applying a deformation grid. The user may employ the ROI tool to evaluate the quality of the correction.....	82
Figure 3-12: Close-up image of the P7-4 ultrasound probe, attached to a Polaris tracker using the custom holder.....	82
Figure 3-13: Illustration of the ambiguity that can arise when attempting to image a small, thin target with a thick US slice (partial volume effect). A: Rotation ambiguity. B: Translation ambiguity. C: Z-bar fiducial marker calculates the position of the intersection of the marker and the center of the slice, reducing partial volume effect.	84
Figure 3-14: A: cross sectional illustration of the parallel Plexiglas plates and the guide hole pattern used to form a Z-bar fiducial marker. B: 3D volumetric reconstruction from CT of the calibration phantom showing the position of the 3 Z-bar markers. B: Cross section CT image of the phantom with the Z-bar markers intersecting the image highlighted in red.....	85
Figure 3-15: Example of an US image of the calibration phantom highlighting the poor signal from the center marker of the vertical Z-bar markers.	86
Figure 3-16:A: Cross sectional view of the phantom. The image shows intersection of the two horizontal Z-bar markers and the two slanted vertical bars with the image plane (highlighted in red). B: An oblique view in the plane of one of the Z-bars. The position of the Z vertices are calculated by extending least squares fits to the straight sections. C: 3D illustration of the phantom highlighting the Z-bar pattern and the relative positions of the registration divots.....	88
Figure 3-17: Schematic view of the single Z-bar calibration phantom.	90
Figure 3-18: A: US image of the Z-bar fiducial clearly showing the walls of the tubes. B: CT image of the phantom. The tubes were filled with contrast agent, and thus appear to be full.	92
Figure 3-19: Image of the deformable phantom held in the support collar in a water bath.....	93
Figure 3-20: Schematic of the construction of the simulated brain hemisphere. A: Red circles indicate points to drill into a 10cm thick slab of Plexiglas. The red line indicates a cut line. The circle on the right is a face view of a Plexiglas rod that was drilled and cut in half to form ventricle molds. B: Schematic view of the final mold.	94
Figure 3-21: Schematic of the support collar, screws and water bath container.	95
Figure 3-22: Volume rendered view of the segmented brain disk. The yellow sections are the hemispheres with the cortical surface, the red strips are the simulated blood vessels while the green sections are the ventricles.	96
Figure 3-23: Illustration of the placement of the thin threads in the geometric distortion phantom. This arrangement allowed for multiple profiles to be obtained at different locations in the image simultaneously.	97

Figure 3-24: Illustration of the slice thickness phantom and its basic principle. Because the target plane intersects the imaging plane with a 45° angle, the height equals its width	98
Figure 4-1: Images of a geometric distortion phantom taken at two MID settings. A: MID=5cm. B: MID=9cm.	102
Figure 4-2: Illustration of the procedure followed to resample and average profiles of the same point from several images. The average profile provided an improved Gaussian distribution.	103
Figure 4-3: Illustration of how geometric distortion is measured. Each row and column is used to calculate a linear best fit. The distance from each point and the line (Δ) quantify the distortion.	105
Figure 4-4: Ultrasound images of the slice thickness phantom taken at a maximum imaging depth of 5cm. A: Profile depth of 4.5cm. B: Profile depth of 1.5cm.....	105
Figure 4-5: Example of image smoothing to improve the reliability of the semi-automatic profile averaging technique. The negative spike may cause the profile trimming procedure to clip significant data. The profile of the smoothed image does not contain the spike. A similar result would have been accomplished by smoothing the profile itself.	106
Figure 4-6: US image of the slice thickness phantom demonstrating the locations of the profile samples for column 1, 2 and 3.	107
Figure 4-7: Axial resolution vs. depth measurements for US images acquired at maximum imaging depths 5, 6 and 7cm. The different lines correspond to different columns measured on the US image (see Figure 4-1).....	108
Figure 4-8: Lateral resolution vs. depth measurements for US images acquired at maximum imaging depths 5, 6 and 7cm. The different lines correspond to different columns measured on the US image (see Figure 4-1).....	109
Figure 4-9: Slice thickness measurements expressed as FWHM of profiles taken from images at US MID values of 5, 6 and 7cm. The different lines correspond to different columns measured on the US image (see Figure 4-6).....	112
Figure 4-10: Probability plot of the sampled values of the X-translations obtained by repeated calibration trials for MID-5cm. The straight line at 45° is consistent with a normal distribution.	115
Figure 4-11: US image of the phantom with the segments identified with the calibration tool. The profiles at the top of the image serve as a visual aid in correctly identifying the center of the segment B: Co-planar CT image with the same segments identified.....	118
Figure 5-1: Illustration of the deformation applied to the phantom. A: US image of the phantom taken through the imaging window prior to deformation. B: Illustration of the directions of movement of the support screws to apply the deformation. C: US image after deformation. Arrows indicate the general direction of compression, expansion or movement of the structures.	123
Figure 5-2: Co-planar MRI images of the non-deformed and deformed phantoms.....	124
Figure 5-3: Homologous structures identified in both the non-deformed (A) and deformed (B) MRI.....	124

Figure 5-4: A: Displacement node grid superimposed on the non-deformed MRI of the deformable phantom. Red crosses indicate nodes that are allowed to displace. B: Displacement grid after application of the initial displacement vectors obtained by identification of the simulated blood vessels, cortical landmarks and ventricles shown in Figure 5-3. 125

Figure 5-5: A: Vector grid obtained after allowing the initial grid of Figure 5-4A to propagate and relax to a steady state condition. The lines represent the direction of the grid node displacements and thus the measured deformation. B: Magnitude image of the displacement. 126

Figure 5-6: A MRI of the deformed phantom (as shown in Figure 5-2B). B: Warped image of the non-deformed MRI for comparison. The warped image contains more noise because it is a 1mm thick slice, while the MR image of the deformed phantom is 5mm thick to improve image quality. 127

Figure 5-7: MRI images of the phantom after registration and before deformation. The ROI tool (arrows) is used to superimpose the US image onto the co-planar MRI to visually assess the registration by observing the degree of shift between homologous structures. 129

Figure 5-8: Registration accuracy assessment. A: US image of phantom with point and line annotation delineated from both the US and MRI image. B: Co-planar MR image of the phantom with the same annotations superimposed. Note the outline of the US image area in red..... 129

Figure 5-9: Displacement magnitude image showing the registration error distribution over the image area. The red triangle shows the US image boundary, and thus the area of interest..... 130

Figure 5-10: Visual assessment of phantom shift. A: US image of the phantom after deformation. B: Co-planar MRI of the phantom. Examining A and B clearly demonstrates a difference between the two. C: The ROI tool used to superimpose the US image on the MRI allowing more detailed visualization and comparison of the deformation..... 131

Figure 5-11: Images of the phantom with point annotations (yellow) of homologous cortical and blood vessel points as well as spline curves (green) showing the ventricles outlines. A US image. B: co-planar MR image. 132

Figure 5-12: A: Deformation grid superimposed on the non-deformed MRI. Red nodes denote nodes within the boundary defining the phantom. B: Initial node displacements from applying deformation vectors calculated from homologous structures defined in Figure 5-11..... 133

Figure 5-13: A: Interpolated deformation vectors obtained by allowing the initial vectors shown in Figure 5-12B to propagate throughout the grid. B: Magnitude image of the displacements. 133

Figure 5-14: Warped MRI obtained by applying the displacement grid shown in Figure 5-13. Closeups of the ROI tool show good agreement between the US and warped MRI in the ventricles and vessels..... 134

Figure 5-15: Homologous points identified from the MR, US and warped (restored) MR images. Just as the US & MR coordinates yielded a vector which defined the deformation at that point, the US & restored MR point yield a measure of the quality of the restoration..... 135

Figure 6-1: Schematic diagram describing the relative positions of the IGNS systems and the operating room staff with respect to the sterile field (green area)..... 138

Figure 6-2: A: Intraoperative photograph of the IGNS pointer and head reference tracker. The head reference tracker is in a sterile bag while the probe was gas sterilized, and thus does not require the bag. B: Intraoperative photograph of the US transducer and tracker within the sterile bag. 141

Figure 6-3: A: Coplanar MR and ultrasound images of the IV ventricle. Point annotations help relate the agreement of the boundaries of the ventricle as seen in both images. B: The cerebellum was outlined on the MRI and overlaid on the ultrasound image demonstrating the occurrence of a tissue shift during or registration error the procedure (arrows). 143

Figure 6-4: Comparison between pre-operative and intraoperative images during a tumour resection. A: Gadolinium enhanced T1 weighted MRI reformatted to match the intraoperative US shown in B. 144

Figure 6-5: Full screen shot of the US based IGNS system. The upper left image shows a 3D surface rendered view of the brain with the probe position of anatomical context. The lower left is the same surface rendered brain and probe, with the addition of skull point samples to delineate the craniotomy and the US image shown in the orientation of its acquisition. The upper right images show the traditional transverse and coronal images, where the tumour can be clearly seen. The lower images show the intraoperative US image and co-planar oblique MRI. The tumour was clearly visible in the MR while it did not enhance well in the US. 146

Figure 6-6: A: Close- up of the oblique MRI shown in Figure 6-5. The tumour was delineated using the spline drawing tool. 147

Figure 6-7 A: Oblique MRI view whose orientation is set to match that of the intraoperative ultrasound image (B). The location of the crosshairs indicates the upper center of the ultrasound image, and not the location of the face of the ultrasound transducer. B: Intraoperative ultrasound image of a patient following the craniotomy. The lateral ventricles, falx and brain/dura interface are easily identifiable. 149

Figure 7-1: Cross section image of the hollow tube Z-bar fiducial marker. A: Filled with water for US imaging, with the tube walls generating contrast. B: Filled with Iothalamate meglumine to generate contrast in CT. 157

Figure 7-2: Suggested design enhancements for a calibration tool for more simple and efficient use in a clinical environment. The adjustable height aperture and flexible membrane allow US images to be made of the Z-bar at various heights without adding or removing US jelly. 158

Figure 7-3: Simple example of image processing to alter the MRI data to better resemble the US data for comparison. A: Oblique MRI (with no filtering) with co-planar US displayed in the ROI box. B: US image. C: Steer-able gradient filtered MRI with co-planar US shown in the ROI box. 164

List of Tables

Table 4-1: Summary of geometric distortion measurements for both rows and columns for all maximum imaging depths.	110
Table 4-2: Reproducibility of the x, y and z translation components of the US→Tracker calibration procedure for MID=5, 7 & 9cm. Mean is the mean value of the translation while the standard deviation is the standard deviation of the component for the 10 trials.	115
Table 4-3: Summary of the results of the IGNS system accuracy results.	119
Table 5-1: Summary of results of the non-deformed vs. deformed MR images of the phantom.	128
Table 5-2: Comparison of point displacements measured (in mm) between homologous US and MR images and US and corrected MR images. The US-MRI column provides a measure of the deformation, while the US-Corr data is a measure of the quality of the correction.	135
Table 7-1: Data collected from 4 operating room cases performed using the same data acquisition protocol.	166

Table of Contents

Abstract	i
Résumé	ii
Original Contribution	iii
Acknowledgements	v
List of Figures	vii
List of Tables	xiv
Table of Contents	xv
Chapter 1 Preface	1
1.1. <i>General Introduction</i>	<i>1</i>
1.2. <i>Thesis Organization</i>	<i>2</i>
1.3. <i>List of Publications</i>	<i>3</i>
1.3.1. Peer reviewed papers	<i>3</i>
1.3.2. Peer reviewed abstracts.....	<i>5</i>
1.3.3. Conference presentations and book chapters.....	<i>7</i>
1.3.4. Awards.....	<i>7</i>
Chapter 2 Evolution of Image Guided Surgery	8
2.1. <i>Introduction</i>	<i>8</i>
2.2. <i>Frame Based IGNS</i>	<i>9</i>
2.3. <i>Frameless Image Guided Neurosurgery (Frameless Stereotaxy)</i>	<i>13</i>
2.3.1. <i>Introduction</i>	<i>13</i>
2.3.2. <i>IGNS: Tracking Devices</i>	<i>15</i>
2.3.3. <i>IGNS Pre-operative Multimodality Image Based Guidance</i>	<i>22</i>
2.3.4. <i>Accuracy Considerations in IGNS</i>	<i>29</i>
2.3.5. <i>IGNS Intraoperative Imaging</i>	<i>41</i>
2.4. <i>Tissue Movement in Neurosurgery</i>	<i>47</i>
2.4.1. <i>Introduction</i>	<i>47</i>
2.4.2. <i>Measurement Methods</i>	<i>47</i>
2.4.3. <i>Pre-operative Image Restoration</i>	<i>49</i>
2.5. <i>Intraoperative Ultrasound in IGNS</i>	<i>51</i>
2.5.1. <i>Ultrasound Theory</i>	<i>51</i>
2.5.2. <i>Integration of Ultrasound in IGNS</i>	<i>56</i>
Chapter 3 Intraoperative Ultrasound IGNS System Description	61
3.1. <i>Introduction</i>	<i>61</i>
3.2. <i>Operating Room Hardware Setup</i>	<i>61</i>
3.2.1. <i>Introduction</i>	<i>61</i>
3.2.2. <i>Reference System</i>	<i>62</i>
3.2.3. <i>US based IGNS system</i>	<i>62</i>

3.3.	<i>IGNS Software Package</i>	64
3.3.1.	Introduction	64
3.3.2.	Image Data Module	66
3.3.3.	Image Processor Objects	67
3.3.4.	Image Display Objects.....	70
3.3.5.	Tools	71
3.4.	<i>Ultrasound Holder</i>	80
3.5.	<i>Ultrasound Phantoms</i>	82
3.5.1.	Calibration Phantoms	83
3.5.2.	Deformable Phantom	92
3.5.3.	Resolution and Distortion Phantom	96
3.5.4.	Slice Thickness Phantom.....	97
3.6.	<i>Discussion</i>	97
Chapter 4	System Characterization	100
4.1.	<i>Introduction</i>	100
4.2.	<i>Ultrasound/Frame Grabber System Characterization</i>	100
4.2.1.	Materials and Methods	100
4.2.2.	Results	107
4.3.	<i>Tracker Precision</i>	110
4.3.1.	Materials and Methods	110
4.3.2.	Results	111
4.4.	<i>US-Based IGNS Calibration</i>	111
4.4.1.	Introduction	111
4.4.2.	Materials and Methods	113
4.4.3.	Results	114
4.5.	<i>Overall System Accuracy</i>	116
4.5.1.	Introduction	116
4.5.2.	Materials and Methods	116
4.5.3.	Results	118
4.6.	<i>Summary</i>	119
Chapter 5	Deformation Detection and Correction	121
5.1.	<i>Introduction</i>	121
5.2.	<i>Non-deformed MRI vs. Deformed MRI</i>	122
5.2.1.	Set-up	122
5.2.2.	Correcting deformation.....	124
5.2.3.	Quantitative Assessment of Restoration Quality	126
5.3.	<i>Non-deformed MRI vs. Deformed US</i>	128
5.3.1.	Imaging and Registration	128
5.3.2.	Applying Deformation.....	130
5.3.3.	Deformation Correction	131
5.3.4.	Applying Displacement Grid to Non-deformed MRI	134
5.3.5.	Quantitative Analysis of Image Restoration.....	134
5.4.	<i>Discussion</i>	136
Chapter 6	Clinical Use	137
6.1.	<i>Introduction</i>	137
6.2.	<i>Materials and Methods</i>	138
6.2.1.	Operating Room Considerations.....	138
6.2.2.	Patient→Pre-operative Image Registration.....	139
6.2.3.	Sterilisation of IGNS Tools.....	140

6.3.	<i>Individual Case Reports</i>	141
6.3.1.	Syringobulbia and Syringomyelia	142
6.3.2.	Tumour Resection 1	142
6.3.3.	Tumour Resection 2	145
6.3.4.	Selective Amygdalo- Hippocampectomy	148
6.4.	<i>Discussion</i>	152
6.4.1.	Practical considerations	152
Chapter 7	Discussion and Conclusion	155
7.1.	<i>Introduction</i>	155
7.2.	<i>Special Tools and Phantoms</i>	156
7.2.1.	Calibration Tool (Phantom)	156
7.2.2.	Deformable Phantom	159
7.3.	<i>System Characterization</i>	160
7.4.	<i>Visualization and Measurement vs. Modeling and Predicting</i>	162
7.5.	<i>Deformation Detection</i>	162
7.5.1.	Suggested Future Work	163
7.5.2.	Research Utility-Deformation Measurement of Multiple Cases	164
7.6.	<i>Clinical Utility</i>	167
7.6.1.	Integrated US Guidance	167
7.6.2.	Deformation Visualization and Measurement	168
7.6.3.	Image Warping	168
7.7.	<i>Conclusion</i>	168
Glossary of terms	170
References	171

Chapter 1

Preface

1.1. General Introduction

Radiological images have been used as a diagnostic tool in medicine for decades. Soon after their introduction by Röntgen, physicians took advantage of this new form of information to better plan and carry out a wide variety of surgical procedures. Over the years, radiologists and neurosurgeons have developed techniques that allowed them to define coordinate spaces common to both the images and the patient's head. This was often facilitated by the use of a stereotactic frame, which allow one to precisely localize targets of interest on the image data, and then accurately reach them within the brain by attaching tools to the frame itself. This class of techniques became known as stereotaxy. Today, stereotaxy, also known as image guided neurosurgery (IGNS) has evolved into two subclasses, frame based and frameless. While the two subclasses have significant differences, they both rely on the identification of fiducial points within the images and patient to determine the mathematical relationship between the images and the head. They both share the assumption that the position of targets within the brain remains constant with respect to the fiducial reference points, that is, that the brain and coordinate system can be considered as a rigid body throughout the procedure. This unfortunately, does not hold true for many neurosurgical applications, particularly where large craniotomies are involved, and so failure of this assumption is a major source of accuracy error in IGNS. This thesis demonstrates the phenomenon of brain shift, and its impact on

the accuracy of IGNS. It also presents a novel addition of intraoperative ultrasound to frameless stereotaxy that allows one to visualize, quantify and correct for brain distortion during neurosurgery.

1.2. Thesis Organization

Chapter 2 follows the development of frame-based stereotaxy and, in more depth, frameless IGNS. This description includes the basic concepts and a description of sources of error, and how these impact on the utility of IGNS in the operating room environment. Emphasis is placed on the concept of brain tissue movement, and its contribution to accuracy errors in IGNS. Common configurations, including both pre-operative image-based IGNS, and more recent systems that include intraoperative information are discussed. Finally, an overview of various techniques for measuring brain deformation in IGNS is presented.

Chapter 3 provides a detailed description of the intraoperative ultrasound (US) based IGNS system developed as part of this work as well as the various phantoms constructed to calibrate and validate the system. It begins with a general description of the major components and continues with a detailed description of the IGNS software. The chapter closes with a description of each phantom built for this work, including general description and construction techniques.

Chapter 4 discusses the methods and results of several experiments performed to characterize and validate the IGNS system. It first presents experiments performed to characterize the individual components of the IGNS system, including the US/frame grabber images and the precision of the tracking device. The precision of the US/tracker calibration is evaluated next, and the chapter concludes with a description of the experiment to measure overall static system accuracy.

Chapter 5 outlines the work performed to evaluate the ability of the US based IGNS system to demonstrate and correct for tissue movement. It is done by using the deformable brain phantom in experiments to simulate brain deformation, and use the IGNS system to visualize, quantify and correct for the distortion. The accuracy in detecting and correcting for the simulated movement is evaluated and presented.

Chapter 6 discusses the results of the use of the US based IGNS system in the operating room for actual surgical cases. Four typical neurosurgical cases are described, each with an emphasis on where the system was useful.

Finally, chapter 7 summarizes the work, and puts it into perspective by discussing the limitations of the current system, and where future work would be fruitful in advancing the state of the art in this field.

1.3. List of Publications

1.3.1. Peer reviewed papers and conference proceedings

- R. M. Comeau, A Fenster, and T. M. Peters, "Intraoperative ultrasound for guidance and tissue shift correction in image-guided neurosurgery". *Medical Physics*, 27 (4), 787-800 (2000)
- R. M. Comeau, A.F. Sadikot, A Fenster, and T. M. Peters, "Intraoperative US in Interactive Image-guided Neurosurgery," *Radiographics* 17 (4), 1019-1027 (1998).
- R. M. Comeau, A. Fenster, A. Sadikot and T.M. Peters, "Combining Intraoperative Ultrasound and Preoperative MR Imaging for Improved Image Guidance in Neurosurgery ", *SPIE Proceedings, Image Processing* 3338(1):747-754.

- D. G. Gobbi, R. M. Comeau and T. M Peters, "Ultrasound Probe Tracking for Real-Time Ultrasound/MRI Overlay and Visualization of Brain Shift.", Medical Image Computing and Computer Assisted Intervention - MICCAI'99. Lecture Notes in Computer Science 920--927, 1999
- D.G. Gobbi, R.M. Comeau, B.K.H. Lee and T.M. Peters. "Correlation of Pre-Operative MRI and Intra-Operative 3D Ultrasound to Measure Brain Tissue Shift" SPIE Proceedings, Medical Imaging 2000, 12-17 February, San Diego, CA.
- A. C. Bastos, R. M. Comeau, F. Andermann, D. Melancon, F. Cendes, F. Dubeau, S. Lafontaine, D. Tampieri, and A. Olivier, "Diagnosis of Subtle Focal Dysplastic Lesions: Curvilinear Multiplanar Reformatting From 3D MRI" Annals of Neurology, 46(1):88-94, 1999
- T. M. Peters, R. Comeau, P. Munger, B. L. K. Davey, L. Pisani, A. Sadikot and A. Olivier, "Image-guided Neurosurgery at the Montreal Neurological Institute," Annual International Conference of the IEEE Engineering in Medicine and Biology Proceedings 2, 635-636 (1996).
- B. L. Davey, , R. M. Comeau , C. Gabe. , A. Olivier, and T. M. Peters , "Interactive Stereoscopic Image-guided Neurosurgery", SPIE Proceedings, Image Display, 2164, 167-176, 1998 San Diego CA.
- A. Olivier, M. Alonso-Vanegas , R. Comeau and T. M. Peters, "Image-guided surgery of epilepsy" Neurosurgery Clinics of North America 7(2):229-43, 1996
- L. J. Pisani, R. Comeau, B. L. K. Davey and T. M. Peters. "Incorporation of stereoscopic video into an image-guided neurosurgery environment," Proceedings of 17th International Conference of the Engineering in Medicine and Biology, 365-6 (1995).

- T. Paus, R. Jech, C. J. Thompson, R. Comeau, T. Peters, and A. C. Evans, "Transcranial Magnetic Stimulation during Positron Emission Tomography: A New Method for Studying Connectivity of the Human Cerebral Cortex", *Journal of Neuroscience*, 17(9): 3178-3184, 1997
- T. Paus, R. Jech, C. J. Thompson, R. Comeau, T. Peters, and A. C. Evans, "Dose-Dependent Reduction of Cerebral Blood Flow During Rapid-Rate Transcranial Magnetic Stimulation of the Human Sensorimotor Cortex", *Journal of Neurophysiology*, 79(2): 1102-1107, 1998
- R. G. Bittar , A. Olivier, A. F. Sadikot , F. Andermann , R. M. Comeau . M. Cyr , T. M. Peters and D. C. Reutens , "Localization of somatosensory function by using positron emission tomography scanning: a comparison with intraoperative cortical", *Journal of Neurosurgery*, 90(3): 478-83, 1999
- T. Peters, B. Davey, P. Munger, R. Comeau, A. Evans and A. Olivier, "Three-Dimensional Multimodal Image-Guidance for Neurosurgery". *IEEE transactions on Medical Imaging*, 15(2): 121-128, 1996

1.3.2. Peer reviewed abstracts

- R. M. Comeau and T. M. Peters, "Intra-Operative Ultrasound Imaging in Interactive Image Guided Neurosurgery". *Radiological Society of North America, Chicago, December 1996: InfoRad exhibit and platform presentation*
- R. M. Comeau, A Sadikot, A Olivier, M. A. Audette, A Fenster and T. M. Peters, "Combining Intraoperative Ultrasound and Preoperative 3D MRI for Interactive Image Guided Neurosurgery" *Radiological Society of North America, Chicago, December 1997: InfoRad exhibit*

- R. M. Comeau, A. Fenster and T. M. Peters, "Detecting Brain Tissue Deformation Using Intra-Operative Ultrasound Imaging In Interactive Image Guided Neurosurgery", 43rd Annual Scientific Meeting of the Canadian Organization of Physicists in Medicine, Charlottetown PEI, 1997: Platform presentation
- R. M. Comeau, A. Fenster, A. Sadikot and T. M. Peters, "Detecting And Correcting Brain Tissue Deformation Using Intra-Operative Ultrasound Imaging In Interactive Image Guided Neurosurgery", 44th Annual Scientific Meeting of the Canadian Organization of Physicists in Medicine, London On, 1998: Poster presentation
- A. C. Bastos, R. M. Comeau, D. Melancon, D. Tampieri, F. Dubeau, T. Peters and F. Andermann, "Image analysis of gyral architecture in cortical dysgenesis by using curvilinear reformatting of 3D MRI," presented at the Annual Meeting of the American Epilepsy Society, Boston, Massachusetts,
- R. M. Comeau, A. Fenster, A. Sadikot and T. M. Peters, "Combining Intraoperative Ultrasound and Preoperative MR Imaging for Improved Image Guidance in Neurosurgery ", Presented at Human Brain Mapping annual meeting, Montreal QC, 1998: Poster presentation
- R. M. Comeau, T. M. Peters and T. Paus, "Optically Based Frameless Stereotaxy for Image Guided Transcranial Magnetic Stimulation (TMS)". Presented at Human Brain Mapping annual meeting, Düsseldorf, 1999: Poster presentation
- A.F. Sadikot, D. Reutens, R.M. Comeau, E. Meyer, T.M. Peters, A. Olivier, "Image-guided Interactive Neurosurgery for Correlation of PET-MRI and Intraoperative Cortical Stimulation", Poster Presentation, American Association of Neurological Surgeons, Minneapolis, MN, 1996
- M. A. Alonso-Vanegas, R.M. Comeau, B.L.K. Davey, M. Preul, E. Brust-Mascher, T.M. Peters and A. Olivier, "Guided Neurosurgery Using The Isg Viewing Wand In

Epilepsy Surgery: Review of 60 Cases”, Poster Presentation, American Association of Neurological Surgeons, Minneapolis, MN, 1996

- A.F. Sadikot, B.L.K. Davey, R.M. Comeau, M. Panisset, G. Bertrand, and T.M. Peters, “Frame-based Interactive Image Guidance for Functional Neurosurgery”, Platform Presentation, Congress of Neurological Surgeons, 1996
- A.F. Sadikot, B.L.K. Davey, R.M. Comeau, G. Bertrand, T.M. Peters, “Validation of an Interactive Image Guidance System for Functional Neurosurgery” Poster Presentation, American Association of Neurological Surgeons, Minneapolis, MN, 1996

1.3.3. Conference presentations and book chapters

- A. Olivier, M. Cyr, R. Comeau, T. Peters, W. Boling, D. Klein and D. Reutens, “Image Guided Surgery of Epilepsy and Intrinsic Brain Tumours”. Book Chapter in Advanced Neurosurgical Navigation, E. Alexander III and R. J. Maciunas Editors. Thieme Medical Publishers, Inc. New York, NY. 39:469-482
- Montreal Neurological Institute “Fellows Day”, 1998
- Montreal Neurological Institute Graduate Student Association “Research Day”, 1999

1.3.4. Awards

- RSNA 1996: InfoRad Certificate of Merit
- MNI Fellows Day, 1998: Killam award

Chapter 2

Evolution of Image Guided Surgery

2.1. Introduction

In November 1895, Dr. Wilhelm Conrad Röntgen discovered, while working with cathode ray instruments, that an unknown radiation emanating from a Hittorf valve could penetrate solid objects, and had the same effect as light on a film plate. Since the particles or rays that created these images were unknown, he referred to them as X-rays. Soon after, the first radiographic image of his wife's hand was obtained, and the usefulness of radiographs, or X-ray images, in diagnosing various ailments became apparent. Prior to Röntgen's discovery, surgeons relied on exploratory surgery (and occasionally autopsy results) to diagnose many neurological conditions. The advent of Radiology ushered in a new era where the surgeons could use images of the patient to help diagnose an ailment, and plan out a surgical procedure beforehand. This technique became known as image guided surgery, or more specifically for the brain, image guided neurosurgery (IGNS).

In many neurological conditions, X-ray images allowed the surgeon to gain some understanding of the individual patient's anatomy before actually opening the skull. Surgeons used this new insight to develop procedures that were less invasive, while maintaining or improving their efficacy. In these early days, image quality was poor by current standards, and the surgeon had to mentally correlate the images with the patient in

surgery. Still, this innovative trend in surgical technique encouraged further innovations in image acquisition to improve image quality, and led to the development of tools that enabled surgeons to truly relate the image to the real anatomy. This field became known as stereotaxy, from stere, meaning solid body and taxis, meaning arrangement. More recently, it has become referred to as frame based IGNS.

2.2. Frame Based IGNS

In 1918, Aubrey Mussen built a stereotactic frame designed for human use.¹ However it was not until 30 years later (after his death) that this device was discovered. In addition, in 1947, a group led by Frederic Gibbs adapted a frame developed in 1906 by British physicians Robert Henry Clarke and Victor Horsley (for use in animals) to study human epileptics². At the same time, Spiegel and Wycis further developed the technique of stereotaxy, which established a three-dimensional Cartesian coordinate system to facilitate the navigation of the human brain. These coordinates were defined with respect to both the brain and the radiographic images that were acquired while the patient was equipped with a reference (or stereotactic) frame attached to the head.

Figure 2-1 illustrates the concept of stereotaxy. As with most stereotactic frames, the Olivier-Bertrand-Tipal³ (OBT) frame, enables one to attach fiducial markers tailored for a particular imaging modality. After images are acquired and transferred to a computer workstation, the fiducial markers are identified and a modality-specific method of calculation to determine transformation from frame-coordinate space to the image-coordinate space is performed.

When two dimensional projection images, such as angiograms, are acquired, fiducial markers in the form of 2mm ball bearings embedded in parallel plates are placed on the frame (Figure 2-1b). The plates and frame are constructed such that the position of

the fiducials are known in the frame coordinate system. When the images are acquired and input into a computer, the fiducials are identified on the image and combined with their known locations in the frame coordinate system, yielding a series of homologous point pairs. These point pairs are used to calculate the homologous transformation matrix (HTM) that describes the projection from the three-dimensional frame coordinate system to the two-dimensional image coordinate system. This transformation maps targets defined in the frame coordinate system to the image.

In the early 1970s three dimensional tomographic imaging was introduced with the development of computed tomography (CT), and more recently, with magnetic

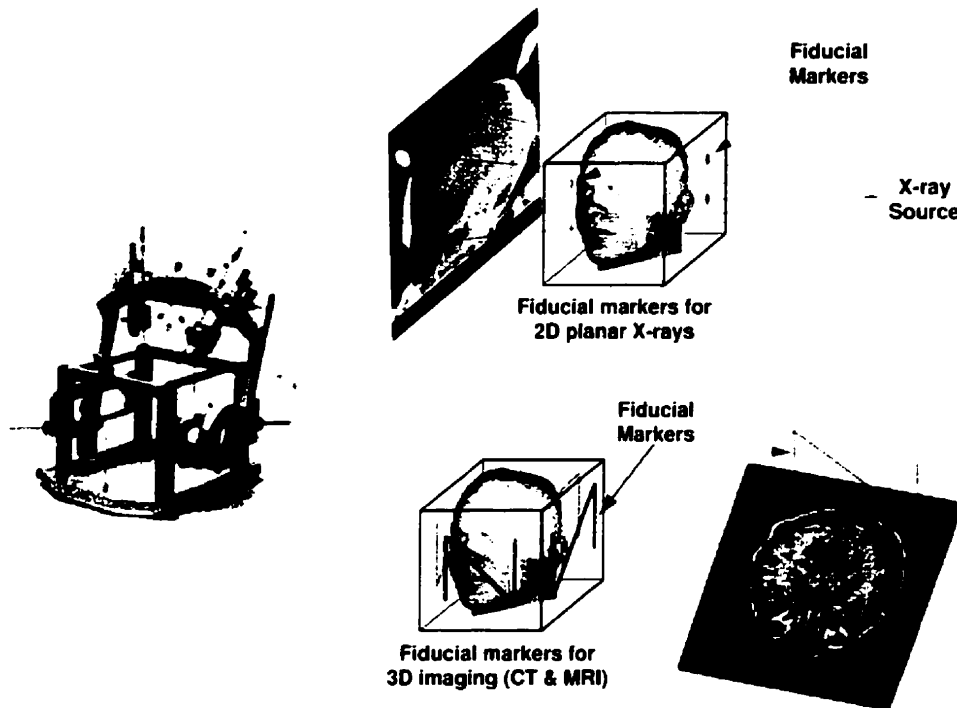


Figure 2-1: Illustration of the concept of the stereotactic frame. A: A typical stereotactic frame: The Olivier-Bertrand-Tipal (OBT) frame, with imaging plates and tools attached. B: Illustration of the position of the ball-bearing fiducial marker configuration for 2D X-ray images. C: N-bar fiducial configuration for computed tomography or magnetic resonance imaging.

resonance imaging (MRI). Along with these systems, new fiducial marker systems were developed to calculate the position and orientation of the images in stereotactic space. In the case of the OBT frame and many other frame standards,⁴⁻⁷ the fiducials used are Z-bars (Figure 2-1c). When a tomographic image of a Z-bar (also known as N-bar) is acquired, three points, the images of the cross section of each segment crossing the image plane, are acquired. Each segment forms a side of a right triangle. From Figure 2-2 and using simple geometry:

$$\frac{a}{l} = \frac{A}{L} \quad (2.1)$$

Thus, the position P_c of the center marker can be calculated by

$$p_c = p_1 + \frac{a}{l}(p_2 - p_1) \quad (2.2)$$

Each tomographic image is acquired with a minimum of three N-bars. Once the centre marker of N-bar has been localized in frame and image coordinates, the rigid body

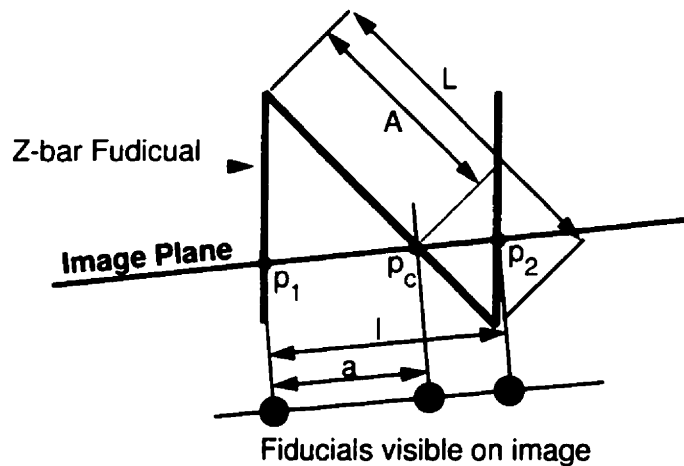


Figure 2-2: Design of the N-bar fiducial marker.

transform from image to frame coordinates (and vice versa) may be calculated.

The main advantage of the stereotactic frame is its accuracy. It has been shown that when image distortion is eliminated, the accuracy of correlating a point in image space to its homologous point frame space is on the order of 1mm in each direction.⁸ This makes stereotactic frames most useful in procedures requiring high accuracy. One such procedure is the treatment of movement disorders. Figure 2-3 shows an example of a stereotactic planning workstation in use at our institution. Ventriculograms, x-ray images of the skull with a contrast agent injected into the ventricles, are acquired in the operating room and are digitally scanned into the planning workstation. Pre-operative MRI data are transferred to the system via a network. After identifying their respective fiducial markers and calculating the frame-to-image registration, any coordinate and trajectory can be entered in frame space, and displayed on the images.

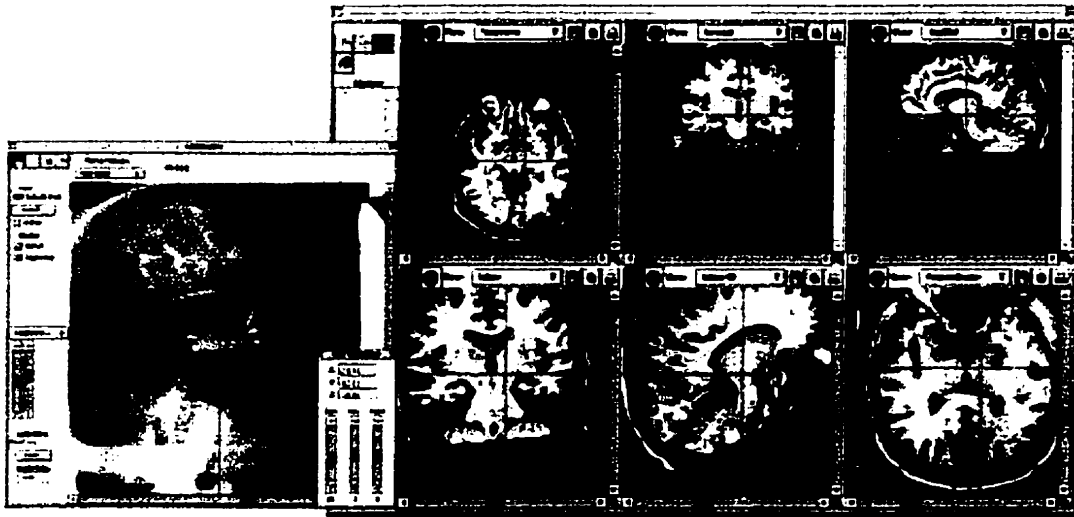


Figure 2-3: Display of a computerized planning system used in the planning of the implantation of a deep brain stimulator into the globus pallidus for the treatment of Parkinson's disease. Both Ventriculography and volumetric MRI are employed to calculate the position of the stimulator prior to implantation.

Neurosurgeons and investigators have continued to adapt the stereotactic frame for a variety of procedures, including atlas based guidance for the treatment of movement disorders,⁹⁻¹² biopsy sampling,^{13,14} electrode implantation for the investigation of epilepsy^{3,15} and cyst aspirations.¹⁶

An additional benefit of the frame is to provide a structure to hold tools for procedures such as biopsies, electrode implantations or small lesion generation. This structure is cumbersome however, and limits unrestricted access to large areas of the head, such as during craniotomies. In these cases, it would be desirable to maintain the ability to correlate the position and orientation of tools with the image data, but also to work without the restrictions of the frame. To accomplish this, the field of “frameless stereotaxy”, or as is more commonly known, interactive image guided neurosurgery (IGNS) was born.

2.3. Frameless Image Guided Neurosurgery (Frameless Stereotaxy)

2.3.1. Introduction

In frame based stereotaxy, correlation of the real world and the image world is accomplished by establishing a common reference space based on the frame. In frameless stereotaxy, the frame is typically replaced by a tracking device, which monitors the position and orientation of a hand held tracked tool holder, to which tools are attached. Figure 2-4 illustrates a typical frameless IGNS system. As in conventional neurosurgery, the patient’s head is rigidly fixed to the operating table, usually employing a clamping system in which compressed pins fix directly through the scalp into the skull. Either the tracking system, or a tracked reference object is rigidly fixed to the head restraint, which serves as the “world”, or patient reference frame. The tracking system is connected to a

computer graphics workstation, where images acquired pre-operatively are stored. After a calibration procedure (described below), which determines the rigid body transformation from the world reference frame to the image reference frame, the computer displays the position and orientation of the tool on the image data.

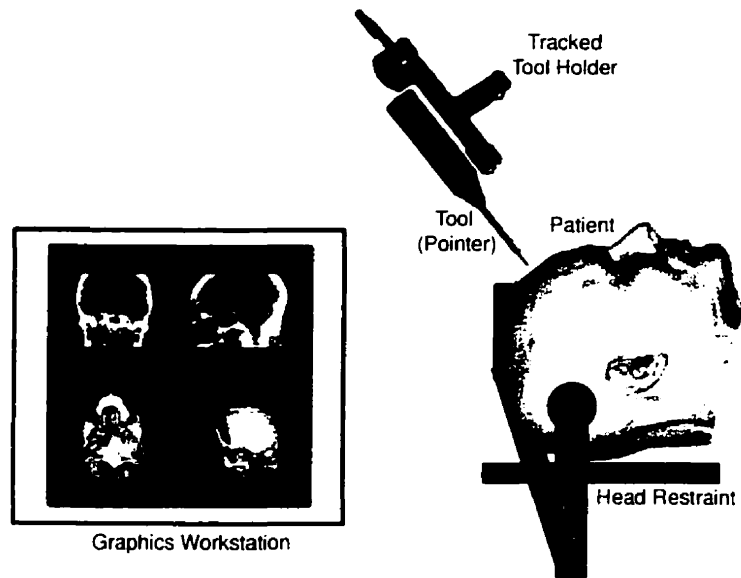


Figure 2-4: Typical IGNS setup: A pointer is attached to a tracked tool holder; in this example, an LED array, whose position and orientation is monitored by a tracking device. The tracker frame-of-reference is assumed to be rigidly fixed to the head. A computer monitors the tracker and displays a representation of the tool within the image data.

In the following discussion, we refer to various “spaces” as illustrated by Figure 2-5. Each defines a Cartesian coordinate system attached to a system component, such as the tracked probe, the probe holder, the patient or the patient’s images. These coordinate systems may be related to one another by arbitrary rigid body or affine transformations, including rotations, translations and scaling. A rigid body transformation may be represented as a 4x4 matrix:

$${}^h_jT = \begin{bmatrix} \cos\alpha \cos\beta & \cos\alpha \sin\beta - \sin\alpha \cos\gamma & \cos\alpha \sin\beta \cos\gamma + \sin\alpha \sin\gamma & t_x \\ \sin\alpha \cos\beta & \sin\alpha \sin\beta \sin\gamma + \cos\alpha \cos\gamma & \sin\alpha \sin\beta \cos\gamma - \cos\alpha \sin\gamma & t_y \\ -\sin\beta & \cos\beta \sin\gamma & \cos\beta \cos\gamma & t_z \\ 0 & 0 & 0 & 1 \end{bmatrix} \quad (2.3)$$

where t_x , t_y and t_z are the translation from space a to b , and α , β and γ are the fixed angle rotations¹⁷ from in the x , y and z directions respectively.

Referring to the figure, the position of the tip of a pointer may be represented in the pre-operative image space by:

$$p_i = {}^i_rT \bullet {}^i_hT \bullet {}^h_pT \bullet p_p \quad (2.4)$$

where p_p is the point of interest in tool space (usually the tip, or origin, of a pointer), h_pT is the transformation from tool to tool holder space, i_hT is the transformation from tool holder to the tracking system origin, and i_rT is the transformation from tracking system to pre-operative image space. i_rT is obtained from the tracking device, i_hT is derived using one of the patient-image registration procedures described below, and h_pT is calculated via a tool-specific calibration procedure, either empirically, or using a method described below.

2.3.2. IGNS: Tracking Devices

A tracking device calculates and reports the position and orientation of an object in three dimensional space. In the context of IGNS, a means of determining the position and orientation of the tool with respect to the patient is required to allow the surgeon to visualize tools used during surgery on the image data. Many investigators have reported various approaches to this task. Most of these involve attaching a tool (usually a pointer)

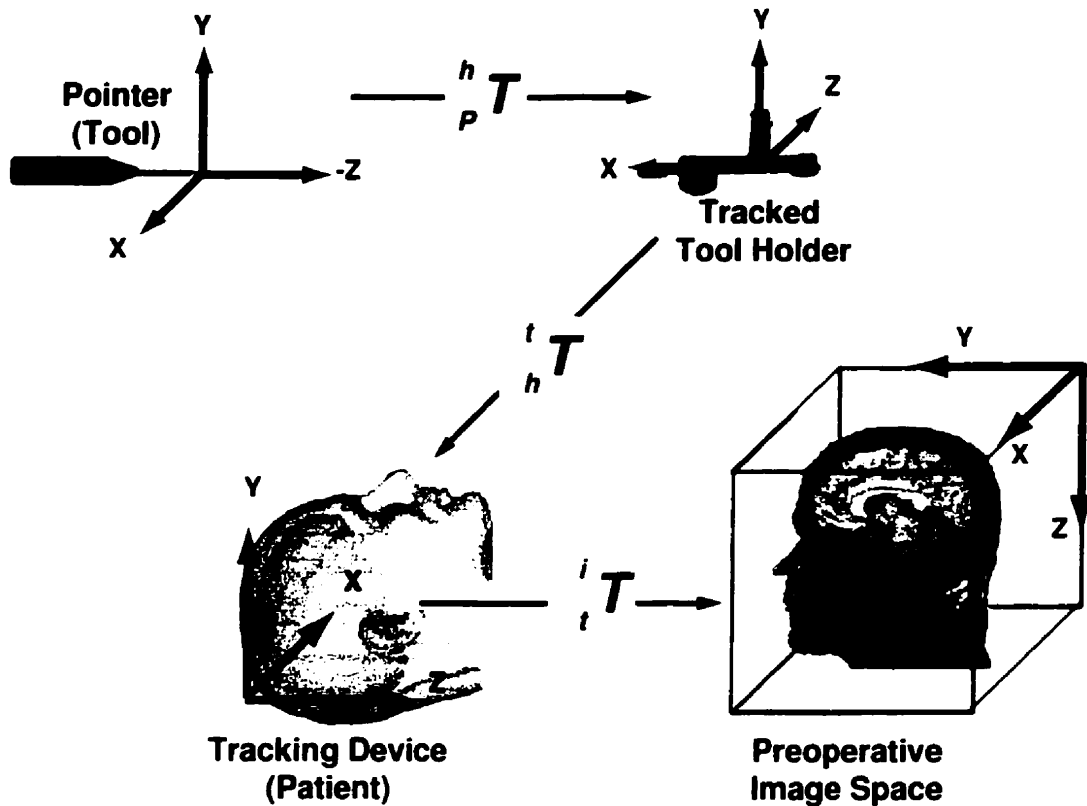


Figure 2-5: Illustration of the coordinate systems and the transformations relating them to each other. Tools are attached to a tool holder, while the holder's position and orientation are monitored by the tracking device and returned to a computer. The transformation from the tracking device to the image frame-of-reference is obtained by identifying homologous points on the patient with the pointer, and on the images with the computer mouse.

to a device to monitor and report its position to the display computer, while others have used "virtual" pointers, such as the focal point of a microscope. This section reviews the current state of the art in tracking devices and their strengths and weaknesses in interactive IGNS.

Some tracking devices may be a single unit, that is, they may consist of a single object that acts as the tool holder and the frame of reference (e.g. articulated arm) while others consist of one or more tracked objects whose position and orientation are calculated in a common frame of reference. For clarity, a tracked object is referred to

simply as a tracker, while the tracking device as a whole (and the common frame of reference it represents) is referred to as the tracking device or system.

2.3.2.1. Articulated arms

One of the first tracking devices to gain acceptance in the operating room was the articulated arm,¹⁸⁻²³ which offers high accuracy and reliability.²⁴ Figure 2-6 shows a common six-degree of freedom articulated arm, the Surgicom (Faro Medical Technologies, Lake Mary, FL). The arm is attached directly to the head fixation clamp, forming a rigid system with the head holder and the skull itself. Sterilization is achieved by draping it in a sterile bag. The end of the arm includes a receptacle to which tools may be attached.

The arm itself is multi-segmented, with high-resolution encoders at the joints. These encoders report the angle of each joint to a computer, which uses these, along with the known dimensions of the arm segments, to calculate the position and orientation of the final segment (the tool holder, or the wrist). Tools are attached to the wrist, and the surgeon may move the tool about while the tracker's computer monitors the extension of the arm and calculates the position of the wrist, which is reported to the IGNS computer. When a tool is attached to the arm, its calibration transformation, h_pT (which is determined *a priori*) must be entered into the IGNS software so it can relate the tool reference frame to the arm's tool holder reference frame.

The main disadvantage of the articulated arm is its bulk and intrusiveness in the operative field. Despite the six degrees of freedom, it can be difficult to orient the tool to the desired location and orientation, particularly if care is not taken in initial positioning of the arm during set-up. In addition, the articulated arm is only capable of tracking one tool at a time. If tracking of more than one tool is required, the tools must be exchanged,

which lengthens the procedure and is difficult to achieve while maintaining the sterility of the tools.

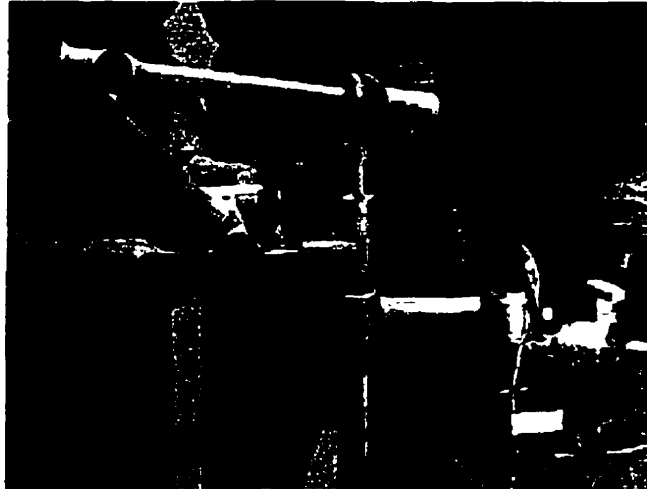


*Figure 2-6: Typical six degree of freedom articulated arm
(Faro Technologies, Lake Mary, FL).*

2.3.2.2. Magnetic trackers

Another early tracking system to be used in IGNS was the magnetic tracker.^{25,26} Magnetic based trackers use a transmitter, positioned near the operative site, to emit a gradient magnetic field. Small receivers, consisting of orthogonal coils, measure the field and allow a connected computer and associated electronics to calculate the receiver's position and orientation within the field. The receivers can be attached to a pointer and other surgical tools, allowing the tools to be tracked in the field.

Magnetic trackers offer advantages over mechanical articulated arms, including a much less intrusive presence in the operative field, increased freedom of movement and the possibility of tracking multiple tools simultaneously. Their disadvantage is in their accuracy and reliability. The basic principle of magnetic field based trackers is that the transmitter creates a known field gradient in its vicinity. The measured field at the

receiver allows its position within that field to be calculated. If a conductive or ferromagnetic object in or near the field distorts the field, the calculated position of the receiver will be in error. Efforts have been made to minimize or at least characterize this susceptibility, and thus increase the reliability²⁷ of magnetic trackers.

Because such interference is difficult to detect, and the errors introduced due to the interference may be subtle, these systems are not “fail safe”, i.e. when it fails, the tracking device returns erroneous results rather than an error message. Because of the importance of the information provided by the tracker (e.g. the position of a tool within a patient’s brain), many of the investigators that have reported on magnetic field tracker based IGNS systems in the past have since adopted other tracking technologies, whenever possible.

2.3.2.3. Optical trackers

Optically based tracking systems use cameras to view light sources attached to a rigid body (or tracker). These sources are either infrared emitters (I-reds) linked to a control unit via a wire, or spherical reflectors which reflect infrared light emitted by the tracking device itself. Multiple cameras (typically two or three) are employed to visualize the emitters, and calculate their location in space by triangulation. Like the magnetic based tracking devices, multiple optical trackers may be used simultaneously.

Optically based tracking systems offer many of the advantages of the magnetic-field based trackers, with the addition of higher reliability. The advantages of optically based tracking systems include: Low intrusiveness in the operative field, excellent mobility of the tools being tracked, the ability to track several tools simultaneously, and immunity to subtle errors related to the exterior environment. Their advantages have led to their widespread adoption by both research investigators,²⁸⁻³⁰ and the mainstream

commercial market.^{31,32} Figure 2-7 illustrates a typical setup for a tracking device, the Polaris optically based tracking system (Northern Digital, Markham ON), used in many IGNS platforms. The camera array is positioned approximately 1.5 m away from the operative field, typically on a stand that allows it to view the operative field from over the surgeon's head. Usually a tracked object, or reference tracker, is attached onto the head fixation device. This allows the IGNS computer to calculate the position and orientation of other tracked tools with respect to the reference tracker, which is rigidly fixed via the Mayfield clamp to the patient's head. This allows the camera to be moved without loss of registration.

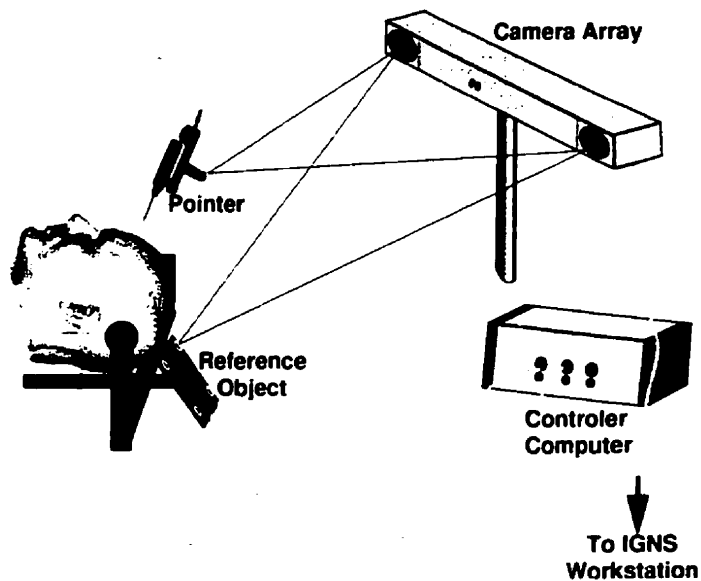


Figure 2-7: Schematic illustration of the Polaris optical tracking system in use at our institution. A reference tracker is rigidly connected to the head fixation device to provide a rigid-body connection between the tracker and the patient's skull. Using both the fixed reference tracker, and the tracked tool, one can calculate the position and orientation of the tool with respect to the reference tracker and thus the patient.

Until recently, optically based systems functioned in an active tracker configuration. That is, the tracked object consisted of an array of infra-red emitters (I-reds) that were activated in a sequence under the control of a computer. Using the array

of I-red positions and the known positions of the I-reds on the tracker. the position and orientation of the tracker was calculated. More recently, passive tracking systems have been introduced. These operate in a manner similar to the active systems, with two exceptions. First, instead of being fitted with emitters, they are fitted with spherical or circular reflectors. The camera array also contains an infrared emitter, which floods the field of view with infrared light. The cameras obtain images of the reflectors, and thus can calculate their position and orientation. Secondly, because the images are of the reflection created by the infrared flash from the camera on the reflectors, the image obtained is of all the reflectors simultaneously. The advantages of the passive systems are twofold. First, there no longer needs to be a wire between the control unit and the trackers, allowing even greater freedom of movement in the operating room. Second, the passive trackers offer a better field of visibility than the I-reds, simplifying the geometry of the tracker, and thus the tracker's construction. The main disadvantage of the passive spheres is that they are costly (\$15-50USD) and delicate, in that they can only tolerate being sterilized once, and thus must be replaced after each case.

The disadvantage of optically based tracking systems (both active and passive), is that they require sight lines between the trackers and the camera. This can be largely overcome by careful planning of the camera position, and by the using a dedicated tracker as a reference object attached to the head fixation clamp. As described earlier, this allows the camera to be moved without losing the ability to calculate the position and orientation of a tracked tool with respect to the head reference tracker.

2.3.2.4. Video Based Trackers

Holton-Trianter et. al.³³ have reported on a novel free-hand tracking device with functionality similar to that of the passive optical tracking system described above. Their system, the VISLAN IGNS apparatus, employs stereo video cameras to acquire images of

tools, which have unique patterns on them (Figure 2-8). Machine vision techniques are used to extract the pattern from the images and calculate its location in 3D space. The authors report that the position of the tool can be localized with an error of less than 0.5mm.

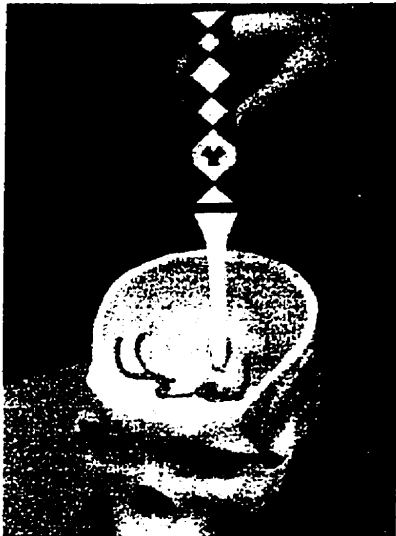


Figure 2-8: Image of the VISLAN pointer. The tool includes a pattern object which can localized automatically using machine vision techniques.

2.3.3. IGNS Pre-operative Multimodality Image Based Guidance

Since the development of radiographic imaging in the early 1900s, investigators have sought to improve and extend its capabilities of providing information regarding the internal structures of the human body. In addition to simple radiography, other volumetric modalities exploiting contrast-generating properties have been developed. Before most surgical cases, surgeons consult a variety of diagnostic image information sources to extract the useful information each has to offer. Some IGNS systems enable the surgeon to integrate these modalities, allowing them to combine their strengths and obtain a better overall picture of the area of interest. An in-depth investigation of each imaging technique exceeds the scope of this thesis, but a brief presentation of the more common modalities relevant to IGNS is in order. In the context of IGNS, imaging types may be

conveniently grouped into pre-operative and intraoperative imaging. Pre-operative based imaging will be presented first, while intraoperative imaging modalities are presented later in this chapter.

Imaging modalities may also be sub-grouped into anatomical and functional areas. Anatomical images demonstrate information about the actual structural relationships within the volume of interest, while functional images, as their name implies, are meant to reveal insight into the operational aspects of the target area. The following section discusses anatomical imaging methods used in IGNS, in chronological order of their development.

2.3.3.1. Anatomical Imaging for IGNS

Computed Tomography (CT)

Computed tomography was the first volumetric imaging modality, and certainly one of the first to be utilized in frameless IGNS. It provides excellent images of the skull, and reasonable images of many anatomical and pathological structures within the brain (e.g. hemispheres, ventricles, tumours). Its ubiquitous availability has made it a common modality for the diagnosis of many neurological disorders. Figure 2-9 shows a screen shot of an IGNS system in use during a resection of a spinal tumour. The CT images (and 3D reconstruction) provide good visualization of the skull base and upper C-spine segments as well and the chord dura and the tumour itself.

While CT images are widely used for many neurosurgical procedures, the visualization of individual brain structures is difficult due to limited soft tissue contrast.. X-ray based imaging generates contrast between structures based on their differential electron density. Many of the structures within the brain have similar density values, and thus do not generate high contrast in the images. Another limitation of CT is that it

exposes the patient to ionizing radiation. The need for high-resolution images typically used in IGNS (e.g. 1x1x1.5mm voxels) results in higher patient exposure to ionizing radiation.

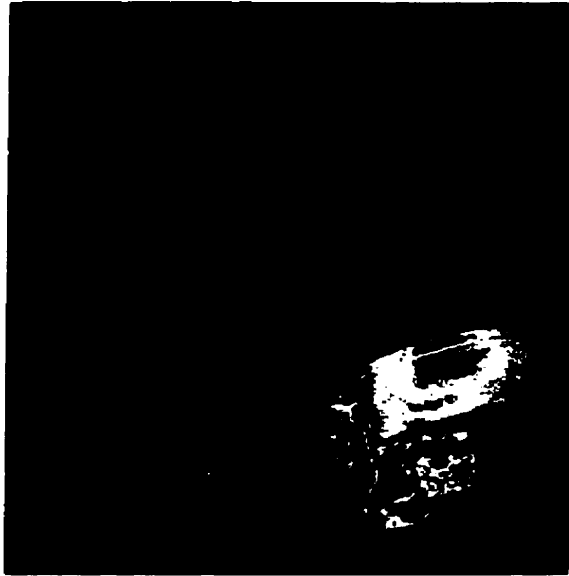


Figure 2-9: Example of an IGNS system (Viewing Wand, ISG Technologies, Mississauga, ON) using volumetric CT data for the resection of a tumour in the spinal canal. Bottom right window shows a 3D reconstruction of the skull, spinal segments, spinal chord dura and tumour. Probe is shown touching the skull base.

Digital Subtraction Angiography (DSA)

Subtraction angiography is a radiological technique where two images, one of the anatomy, and the second one of the same anatomy with a contrast agent present in the blood vessels, are acquired. After acquisition, they are subtracted from one another, forming a third image where common structures are subtracted out to enhance the vasculature. This technique was first performed using film based images, but more recently, the images have begun to be acquired and processed digitally using an image intensifier, thus the procedure is now called digital subtraction angiography. DSA is a diagnostic modality commonly used in the investigation of blood flow abnormalities such as strokes, arterial venous malformations (AVM) and hemorrhages. It is also used for

pre-operative planning when performing biopsies or implanting electrodes into the deep structures of the brain.³⁴ Its historical use in frame based stereotaxy has led to its use in frameless IGNS procedures, where the tracking device has replaced the frame. Today, DSA is being employed less frequently as the less invasive and cheaper magnetic resonance angiography (MRA) and infused CT (CTA) become more popular.

Magnetic Resonance Imaging

MRI is widely accepted as the most significant development in neuro-imaging since the discovery of X-rays, and has quickly become the imaging modality of choice for diagnosing and guiding the treatment of many neurological conditions. It provides high resolution (typically isotropic 1mm voxels), high contrast images of the brain's anatomy. The basic principle of MR imaging relies on the response of atomic nuclei to stimulation from external magnetic fields. The subject is placed in a strong uniform (or gradient) magnetic field (typically 1.5Tesla) causing the naturally random directions of the spin of the nuclei to line up with the field. These nuclei are then subjected to other varying magnetic fields (excitation sequence which is dependant on the imaging protocol) to cause the direction of the spins of the nuclei to loose their alignment and presses away from the direction of the main field. This is analogous to tapping on a spinning top causing it to presses about the original spin axis. After the stimulation, the spin precession decays as the spin realigns itself with the main field. This realignment process, or spin decay, is dependent on the strength of the external magnetic field and the magnetic moment of the nuclei themselves. This decay is measured with receiver coils and can be processed to generate images.

Excitation sequences may be varied to exploit different contrast mechanisms in the target volume. MRI generally refers to images obtained using sequences that optimize anatomical structural contrast. Images of the brain's vasculature may be obtained using

other excitation sequences or by using a contrast agent (Gd-DTPA), and are referred to as (MRA).

The high contrast available in MR images allows the segmentation, labeling and display of selected structures derived from the image. Data are often displayed as colour coded surface rendered images. Figure 2-10a shows a screen shot of an IGNS system (Viewing Wand) displaying perpendicular cuts (MPR) into the MRI volume as well as a 3D surface rendered view of the segmented brain. Figure 2-10b shows a 3D volume rendered (maximum intensity projection, or MIP) view of a MRA image data set, demonstrating an arterial-venous malformation.

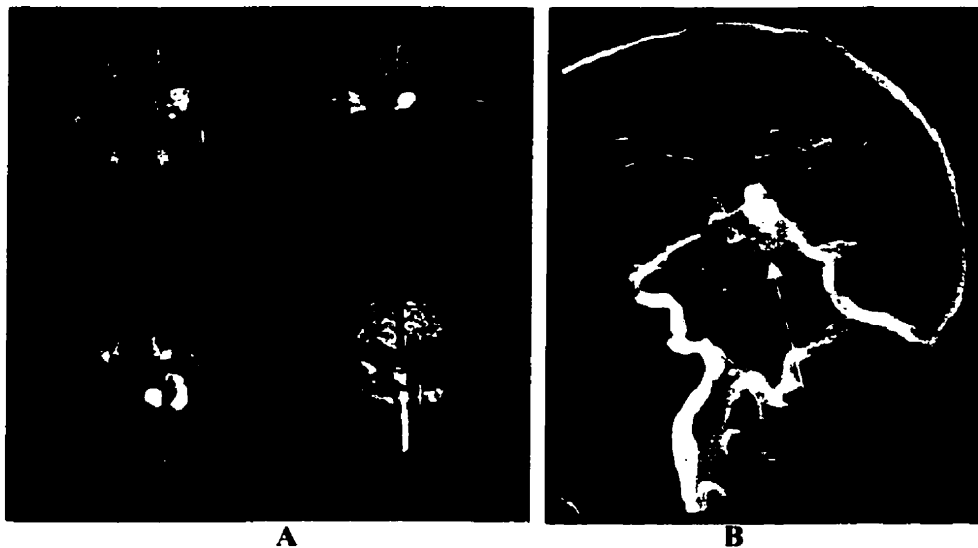


Figure 2-10: A: Typical IGNS (ISG Viewing Wand) screen using Gadolinium enhanced MRI to highlight tumour nodules. Brain surface and tumour nodules were segmented and are displayed as colour coded surfaces in the bottom right view. B: Maximum intensity projection image of a magnetic resonance angiogram of a patient with an arterial venous malformation (arrow).

Although MRI provides excellent images of the brain, unlike CT, they are prone to geometrical distortion. These distortions are often caused by imperfections in the

magnet, which in turn causes the magnetic field to be inhomogeneous. Such distortions have been extensively studied in the context of frame based stereotaxy,³⁵⁻³⁷ where additional sources of distortion may come from the magnetic susceptibility of the stereotactic frame itself. MRI distortion has also been studied in the context of multimodality image registration³⁸ and IGNS.^{39,40} Again, static field inhomogeneity was found to be a significant contributor. MRI distortion can be minimized or corrected by modifying the acquisition technique or by performing a non-linear registration with homologous CT images, which contain less soft tissue contrast, but also have little or no distortion.

2.3.3.2. Functional Imaging in IGNS

In addition to anatomical images, neurosurgeons also rely on image information that relays brain function, rather than structure. This type of information can be invaluable in many situations, for example in guiding the resection of a tumour that lies close to a critical region of the brain, such as the speech area. Among the various pre-operative functional imaging modalities, positron emission tomography (PET) and more recently, functional magnetic resonance imaging (fMRI), are most common.

Positron Emission Tomography (PET)

Positron emission tomography was introduced in the mid-1970's.⁴¹ Images are obtained by detecting co-incident photon (511 keV) emissions that are characteristic of a positron-electron annihilation event. Positrons are introduced into the brain using pharmaceuticals tagged with a positron-emitting isotope (e.g. 2-fluoro-2-deoxy-D-glucose (FDG)). These pharmaceuticals are designed to compete with naturally occurring chemicals that are present in the brain. In the case of FDG, it partially replaces glucose consumed by the brain during normal synaptic function. Typically a baseline scan is obtained with the subject at rest. A second scan is obtained with the subject performing a

specific task (e.g. finger tapping to perform a motor task). Subtracting the two images produces statistical difference image, which represents how the function of the brain changed during that task. In IGNS, these tasks are designed to delineate the functional borders of structures significant for a specific surgical procedure.

The advantage of PET is that it is possible to obtain images of high functional specificity, for example, images representing motor or sensory function. In addition to task related functional images, other pharmaceuticals that target metabolic function of specific pathologies (e.g. tumours) may be used to enhance their imaging.

In order to provide anatomical context to the functional images, the PET data are usually segmented using a statistically derived threshold to display significant activation peaks, which are superimposed on an anatomical data set (typically MRI) of the patient. Figure 2-11 is an example of a functional PET scan superimposed on anatomical MRI for surgical guidance during a tumour resection. The surgeon can use the functional data to highlight eloquent areas that should be avoided during the resection.

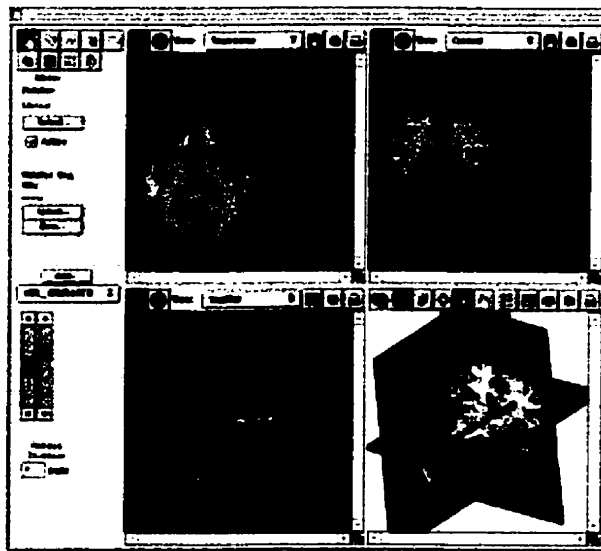


Figure 2-11: Example of a PET image superimposed on an anatomical MRI data set for surgical guidance. Here, the surgeon wished to have the functional boundaries of the motor cortex delineated to help avoid it during the resection of a lesion.

The disadvantages of PET are its relatively low resolution (typically 5mm³ voxels), exposure of the subject to radiation, limiting the amount of data that can be acquired, and the requirement of a significant investment in equipment (e.g. a cyclotron to produce radio-pharmaceuticals) and expertise.

Functional Magnetic Resonance Imaging (fMRI)

Functional magnetic resonance imaging is a relatively new imaging modality that promises to greatly increase the neurosurgeon's access to patient specific, high resolution, volumetric, functional information. As with anatomical MRI, fMRI uses selective excitation of nuclei within the brain to generate contrast. Its basic principle lies in excitation sequences that attempt to measure blood oxygenation levels within the capillaries of the brain, which are thought to correlate with local brain activity in the vicinity of those capillaries. As with PET, images of the patient at rest are obtained, followed by images of the patient performing a specific task. Analysis of the two data sets results in a statistical map representing the relative change in blood oxygenation level which is correlated with the input stimulus and represents the brain's functional change elicited by the task.

The recent proliferation of MRI scanners in the medical community provides an opportunity to make fMRI more accessible than PET as a tool for surgical guidance. It also offers higher temporal resolution than PET, and does not expose the patient to radiation. This enables one to perform multiple studies on single subjects (or patients) without concern for radiation safety limits.

2.3.4. Accuracy Considerations in IGNS

There are several sources of error associated with IGNS systems, all of which lead to the position of the tracked probe being incorrectly reported in relation to the images

used for guidance. These errors can be conceptually linked to the failure of two basic assumptions:

1) **Accuracy:** That the equipment, registration and images are perfectly accurate, that is, that the pointer tracking device is free of positioning error, the registration between the patient and image spaces is error free, and that the images are free from spatial distortion.

2) **Rigidity:** That the equipment and volume of interest form a completely rigid system, that is the structures of interest within the brain remain in the same position with respect to the external fiducial points used for patient-image registration and the tracking device throughout the procedure.

Recalling Equation 2-4, individual errors associated with IGNS can be associated with errors in determining each of the transformation matrices, namely h_pT , the transformation from tool-to-tool holder space, t_hT , the transformation from tool holder-to-tracker space provided by the tracker, and i_tT is the tracker-to-image space transformation, determined by the patient-image registration. Their relative contributions to the overall error can be determined by measuring the consistency, or precision, of the measurement of each transformation. In addition to the precision of each transformation, the overall system accuracy can be determined.

2.3.4.1. Accuracy Errors – Errors in h_pT

The transform h_pT represents the transformation from a particular tool's frame of reference (or space) to the tracked tool holder space. The value of h_pT cannot be measured directly as the origin and orientation of the tracked tool holder is usually not physically identified on the holder itself. Special calibration procedures must be performed so that the position and orientation of the tool and tracked tool holder are known simultaneously

in the tracking device space. The precision of pT can be estimated by performing the measurements required to evaluate pT multiple times, and calculating the standard deviation of the measurements.

The method employed in determining pT is dependent on the tool being calibrated, thus each tool and method will have their own sources of error. In every method, the tracking device is required to obtain the measurements to calculate pT , so the error in pT will include the error of the tracking device itself. In the context of this thesis, two tools of interest are considered: a simple pointer and a US image from a tracked transducer.

As with the tracked tool holder, the origin of many tools cannot be physically localized in the tracking device space. The US image origin is one such example. While there is no physical origin to localize, there is a rigid body connection between the US image and the tool holder that can be expressed mathematically. We refer to this as a virtual probe. Another example of a virtual probe used in IGNS is the focal point of an operating microscope while tracked by an IGNS system. Figure 2-12 illustrates the relationship of the tool's origin and the tracker tool holder for a pointer, a tracked US transducer and the focal point of a tracked microscope.

Pointer Calibration

Hartov et. al.⁴² describe a typical method, supplied by a magnetic field tracking device manufacturer (Ascension Technology, Milton VT), for determining the translation vector from a tool holder to a stylus tip. The calibration procedure involves placing the probe tip into a known (or at least constant) location (e.g. a divot point) and obtaining multiple (n) samples at different tool holder orientations. Each sample provides the orientation and position of the tool holder, and is represented as a 3x3 rotation matrix

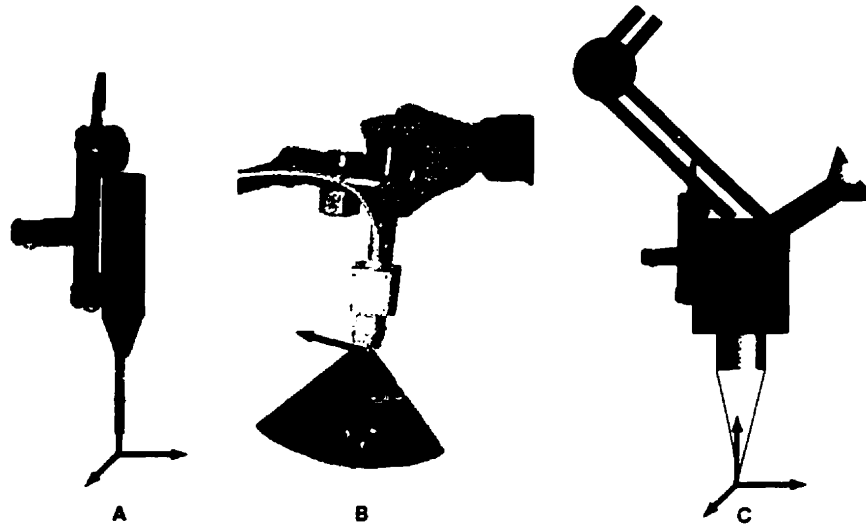


Figure 2-12: Examples of physical and virtual tool coordinate spaces. A: A pointer has its tip as its coordinate space origin, which is physically attached to the tracker. B: Tracked ultrasound probe. The origin is based in the image, which can be treated mathematically as rigidly attached to the tracked transducer. C: Tracked intraoperative microscope. The origin is the focal point, which can also be regarded mathematically as being rigidly attached to the microscope lens.

(M_{3c3}) , denoting the rotation of the tool holder in the tracker space, and a vector in tracker space (p_r) representing the position of the tool holder. Using this notation, the position of the pointer tip (V_i) for any sample i can be expressed as

$$V_i = M_i \times V_s + Pr_i \quad (2.5)$$

By subtracting $(n-1)$ equations from the first, and summing them, it can be shown that:

$$\left(\sum_{i=2}^n Pr_i - (n-1) \bullet Pr_1 \right) = \left((n-1) \bullet M_1 - \sum_{i=2}^n M_i \right) \times V_s \quad (2.6)$$

or,

$$P = M \times V_s \quad (2.7)$$

Finally, we can solve for V_s , yielding

$$V_s = (M_l \times M_t)^{-1} \times (M^T \times P) \quad (2.8)$$

Although this method yields the pointer tip offset vector from the tool holder, it assumes identical orientation between the pointer axis and the tool holder. This assumption is acceptable if we are only interested in the position of the pointer tip in tracker space, but if the relative orientation is desired (e.g. to reference the orientation as well as position of the pointer shaft), another method is required.

US Transducer Calibration

Several methods have been reported for determining ${}^h_p T$ for a tracked US transducer. While each method differs slightly in implementation, they all involve acquiring images of a calibration phantom while the US transducer is attached to the tracked tool holder⁴³⁻⁴⁷. Trobaugh et. al.⁴⁵ were among the first to report such a technique, which involved acquiring multiple images of a wire cross phantom, transforming these images to a common probe reference frame, and using these points in a least squares (Gram-Schmidt orthogonalization) technique to solve for the calibration matrix.

2.3.4.2. Accuracy Error—Registration Error (${}^i T$)

The lower invasiveness and intrusiveness of frameless IGNS has many advantages over frame-based stereotaxy, however it has been largely at the expense of accuracy, specifically with respect to the mapping the patient space to the image space. In frame based stereotaxy, registration is performed by identifying fiducial markers that are designed to be easily visualized when imaged, are at precisely known locations in the frame coordinate space, and are rigidly fixed to the patient's skull. In IGNS, other

strategies have been adopted to try to avoid the invasiveness associated with the frame, with some sacrifice of registration accuracy. These include the use of anatomical rather than implanted artificial landmarks as fiducials.

The accuracy of the patient-to-image registration can be assessed by performing the registration procedure, and evaluating the target registration error (TRE). This method assumes that the image is distortion free, or that the registration error incorporates the error introduced by image distortion. Fitzpatrick et al.⁴⁸ have derived expressions for TRE, and show that the TRE is directly related to the error in identifying fiducials on the patient, and on the relative placement of the fiducials themselves.

In practice, the TRE is evaluated in a visual manner. The surgeon places the pointer on anatomical landmarks on the patient and observes their corresponding point on the image data. This process is often repeated at several intervals throughout the procedure to ensure that the static registration has not been lost due to undetected movement of the head within the clamp. After the craniotomy, internal landmarks (e.g. blood vessels, skull base) are used because the external landmarks are often covered by the sterile drape. It is common practice for the surgeon to initially drill small divot holes into the skull surrounding the craniotomy area to provide accurate landmarks to consult during the procedure. When using brain based landmarks, any detected movement is a combination of registration error, possible skull slippage within the clamp, and non-rigid movement (if present) of the brain structures being localized within the skull.

All registration techniques first involve the identification and matching of features on the patient head. There are several registration techniques to consider, each with respective advantages and disadvantages. These strategies can be classified as point-based and surface-based methods, with the former being the most common. The most

accurate, and most invasive of these approaches involves the use of bone implanted fiducial markers. A less accurate, but less invasive technique is to use fiducials adhered to the scalp, while, the least invasive, and least accurate methods are those which use anatomical features as fiducials. The other class of methods, surface based methods, acquires surface information via a range sensor, video camera or by discrete sampling with the pointer of the skin surface. This surface description is matched with skin surface information extracted from the pre-operative image data to obtain a transformation that best maps the two surfaces to each other.⁴⁹

Point based methods

Point based methods involve the identification of discrete homologous points on both the patient and the images on the computer workstation. The homologous points are used to determine a rigid body transformation between the patient and image data, usually employing a least-squares fitting algorithm.⁵⁰ The different approaches in these methods are related to the targets chosen as fiducial markers, namely either bone implants, scalp markers or anatomical landmarks as illustrated in Figure 2-13. Various investigators have performed comparisons between these techniques in order to aid the surgeon in selecting the appropriate method for a particular accuracy requirement^{51,52}.

Bone based fiducial markers are screwed into the skull directly. They are designed to be visible in the acquired images, and have a well-defined physical mark that can be accurately reached with a pointer in the operating room. It has been demonstrated that an accuracy comparable to that of stereotactic frames⁵³⁻⁵⁷ (on the order of 1mm) can be achieved with this approach. It does however, lack many of the non-invasive advantages promised in IGNS. As in frame-based stereotaxy they require that a separate image data set be acquired after marker implantation, since the image data that were used

for diagnosis would not be acquired with the fiducials in place. This increases organizational complexity and the overall cost of the treatment.

Others have reported fiducial markers attached to rigid bodies that are fixed to the patient via a dental mold, which fits on the upper maxillary teeth⁵⁸⁻⁶⁰ (Figure 2-13b). These investigators have not reported TRE values, but have reported on application reproducibility, i.e. how well the fiducial device can be removed and reapplied in the same location with respect to the patient's head. Results show that reapplication precision was sub-millimeter, which would lead one to expect the accuracy of such device to be comparable to bone implanted fiducials. Recalling the work of Fitzpatrick et al.⁴⁸ and Peters et. al.⁶¹ however, generally, the TRE error increases with distance from the fiducials (e.g. in the region of the posterior fossa). Since the fiducials are predominantly in the front of the patient, the registration error is expected to increase towards the rear of the head.

Hirschberg reported on the use of the Laitinen re-applicable non-bone implanted stereo adapter (frame) that is placed on the patient for imaging, and replaced for the registration procedure during surgery⁶² (Figure 2-13). The frame is held in place using non-invasive ear bars and a rigid support that rests on the bridge of the nose. Their results of TRE accuracy however, range from 3-5mm, which is similar to those obtained using scalp fixed markers, or anatomical landmarks alone. In addition, despite the non-invasive procedure to apply the frame, personal experience has shown that the frame is somewhat uncomfortable or painful to wear, and is difficult for patients to tolerate.

Alp reported on the use of fiducials that are fixed to the scalp⁵². They typically consist of soft hollow torroids which contain imaging modality specific contrast agents, and which are fixed to the scalp with an adhesive. Overall system accuracy resulting from

their use in registration have been compiled for both MRI and CT. For CT, they have been shown to have an accuracy of $\approx 1.5\text{mm}$, and $\approx 2.5\text{mm}$ for MRI.

Finally, our experience at the Montreal Neurological Institute⁶³ has shown that anatomical landmarks can be successfully used as fiducial points for registration with a resulting TRE in the range of 2-4mm. Anatomical points such as the bridge of the nose and the external canti of the eyes are sufficiently close to either the skull or cartilage to be reasonably rigid. Other points, such as the inter-trageal notch superior to the tragus may be used, but are more difficult to identify without ambiguity. Care must be taken to ensure that the same anatomical point is identified on both the patient and the images. The main advantage of using anatomical landmarks is that it does not require that a dedicated set of images be acquired with fiducial markers. This simplifies surgery and imaging scheduling, and reduces the number of scans required to treat the patient, reducing costs.

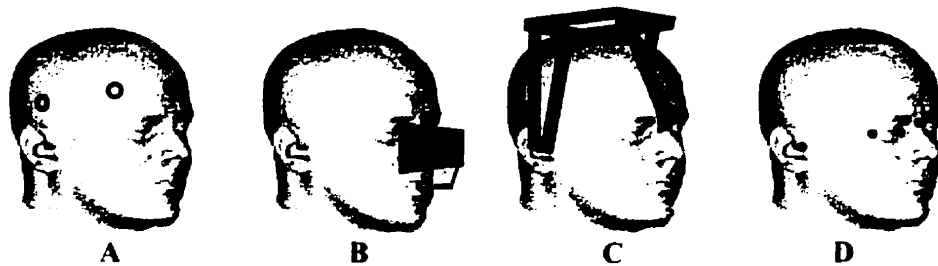


Figure 2-13 Various fiducial marker strategies for IGNS. A: Bone and skin implanted markers. B: Bite-bar held fiducial marker array. C: Non-invasive re-locatable frame. D: Anatomical or skin bonded landmarks.

Despite their lower accuracy compared to skull based fiducial markers, anatomical and scalp fixed landmarks are likely the most common technique used for patient image registration. They are the least invasive, and provide acceptable accuracy

for many procedures. Ultimately, the surgeon performs the judgement of desired accuracy vs. the invasiveness for a given case.

Surface Based Methods

Although point based methods require no special equipment, and are conceptually straightforward, they can be time consuming during the setup for surgery. Other methods have been described to simplify the registration procedure. Grimson et. al.⁶⁴ described a registration technique using a laser range-finder to identify the skin surface of the patient prior to the craniotomy, and matching the range-finder surface to the skin surface segmented from pre-operative MRI or CT. While this has the potential to simplify the registration process, it requires a laser range finder, increasing the overall cost of the IGNS system. Holton-Tainter et al. describe an IGNS system that employs stereo video as a means of detecting the patient's skin surface to obtain the range data required to calculate the patient-to-image registration^{33,65}. The same cameras used for registration are used to track the surgical pointer as described in section 2.3.2.4. Kall et. al.⁶⁶ report on a method whereby the skin surface is sampled by tracing it out with a tracked pointer.

In addition to using external features for registration, Nakajima et. al.⁶⁷ reported on the use of cortical surface blood vessels observed after the craniotomy as internal landmarks to refine an initial registration based on video imaging of the patient. Their technique elicits two concerns. First, the internal anatomical landmarks used to refine the original registration are not rigid. The non-linear movement of the cortical surface (and blood vessels) cannot accurately be described by a rigid or affine transformation. In addition, their registration was performed between a 2D video image and a 2D surface rendered image of the blood vessels derived from a pre-operative MRI data. Because the depth dimension is omitted, the non-linear movement of the cortical surface (and blood vessels) in the direction perpendicular to the image plane is not measured. Thus, the

“correction” to the registration may in fact degrade the registration without being detectable.

2.3.4.3. Rigidity Errors: Image Distortion

In simple terms, when we examine an image, we often make visual interpretations of the locations of certain structures with respect to other structures. In the case of localizing a tumour for example, one would look at the surrounding structures (e.g. falx, ventricles) to get a sense of its location. In IGNS, the locations of structures of interest within the patient’s skull are identified within the tracking device’s frame of reference (space) and subsequently mapped to the image space using the patient-to-image registration transformation(T). Recall that T is calculated by identifying homologous features in both the patient and images. The calculation of T assumes that the relationship between the patient and images can be described as a rigid body transformation. Image distortion can introduce errors in the determination T , and thus in its ability to map patient coordinates to image coordinates. This problem also affects inter-image registration accuracy used in multimodality IGNS⁶⁸.

In practical terms, image distortion is found most often in DSA and MRI, each for different reasons. In DSA, image distortion is introduced predominantly in the image intensifier by the effect of external magnetic fields (e.g. earth’s field, electric cables) on the electron beam, and from the spherical shape of the face of the image intensifier. The former manifests itself as a linear shift while the latter as a “pin cushion” effect.

In MRI, image distortions are often the result of inhomogeneity of the static magnetic field, or of the gradient field, or from magnetic field susceptibility distortions, and can be as high as 2-5mm.³⁹ Many investigators have examined these, and have proposed solutions. Some involve performing non-linear warping of the MRI by

correlating it to CT data.³⁵ Others have proposed modified excitation protocols to minimize the distortion in the MR images during acquisition.^{36,38,69}

2.3.4.4. Rigidity Errors: Head Fixation

During IGNS procedures, the patient's head is rigidly fixed to the operating room table. Figure 2-14 shows two head fixation devices for IGNS. The first is a "Mayfield" clamp commonly used for craniotomies. The second is a "C-arm" clamp that allows access to both sides of the head.⁷⁰, and is used for bilateral depth electrode implantation. Both devices employ compressed pins to fix the clamp directly through the scalp into the skull, and are sufficiently robust to ensure that negligible flexing occurs under the typical loads encountered in the OR.



Figure 2-14: Head fixation devices used in IGNS. A: Mayfield clamp which is used mainly for craniotomies. B: C-Arm, used for bi-lateral implantations of depth electrodes.

Although rare, a movement of the clamp with respect to the tracker, or of the skull with respect to the clamp may occur after registration. This can be corrected by drilling small reference points on the skull and localizing them with the IGNS pointer before the initial craniotomy. These points can be verified during the procedure to ensure that there

has been no rigid body movement. If movement has been detected, these points can be used to determine a rigid body transformation to correct the registration. Because these points can be precisely identified, a rigid body “correction transformation” can be added to the original registration without adding significantly to the original registration error.

2.3.4.5. Rigidity Errors: Brain Rigidity

During open craniotomies, the release of intra-cranial pressure, the effect of gravity and drugs, and the resection of tissue, causes the brain to distort with respect to the skull, and more importantly, the external registration points. This movement is common, and has been measured by various investigators to be up to 15mm,^{71,72} and sometimes as high as 20mm. Brain shift represents the single largest source of error in IGNS. Figure 2-15 illustrates the effect of brain distortion on IGNS accuracy.

In addition to brain shift after craniotomy, the actual manipulation and/or removal of brain tissue causes the geometrical relationships of the brain in the real world to diverge from the image of the brain obtained pre-operatively.

2.3.5. IGNS Intraoperative Imaging

Despite the wealth of information offered to surgeons by pre-operative based imaging, more relevant and up-to-date intraoperative information is required to overcome the effect brain movement has on the accuracy of the pre-operative image information. Intraoperative imaging has been used for years to guide tools and monitor the progress of many surgical procedures. Mapping the pre-operative images to the intraoperative images allows the surgeon to better appreciate the degree of tissue shift, and also maintains the relevance of the pre-operative image features by allowing them to be superimposed on the intraoperative images and vice versa. This section will briefly describe the more common intraoperative imaging techniques, particularly those relevant to modern IGNS.

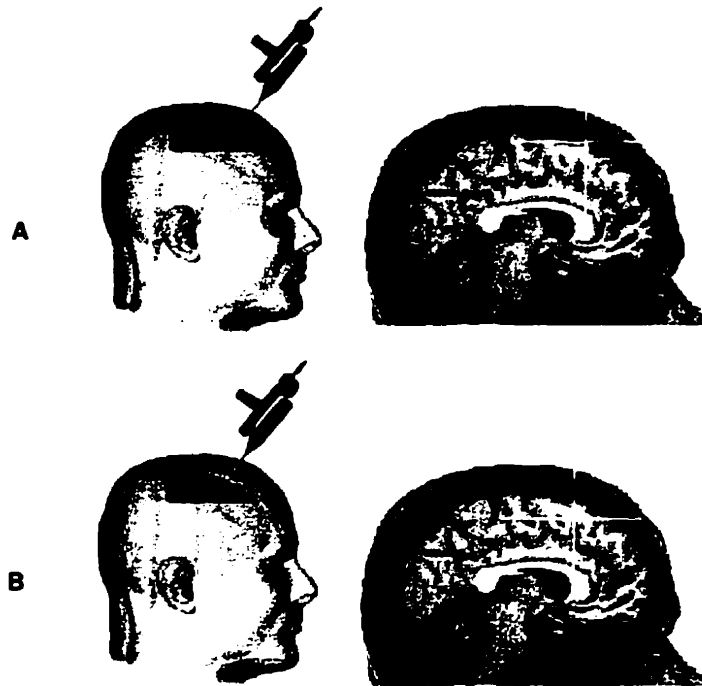


Figure 2-15: Effect of brain tissue distortion on IGNS accuracy: A: After craniotomy, the probe is placed on the cortical surface, assuming no distortion of the brain tissue, the position of the pointer is accurately represented on the pre-operative image data. B: Brain tissue distortion: Here the brain has sagged after the craniotomy. This time, when the probe is brought to the surface of the brain, its position is incorrectly reported as inside the cortex. This is because the actual brain tissue has moved with respect to the external landmarks used for registration

2.3.5.1. Intraoperative X-ray and Fluoroscopy

Intraoperative X-ray imaging is used for a variety of procedures, including confirmation of tool placement in stereotaxy. Fluoroscopy is commonly used as an intraoperative guide for many orthopedic and spine procedures. Recently, Hamadeh reported on techniques to correlate, or register, intraoperative fluoroscopy with pre-operative CT images.⁷³ In addition, Guezic⁷⁴ reported on a similar technique to correlate CT and intraoperative fluoroscopy to improve the guidance of a surgical robot.

Among others, Sofamor Danek has introduced an extension to their pre-operative based IGNS system, the Stealth Station (Medtronic Sofamor Danek, Memphis TN), that incorporates intraoperative fluoroscopy into their IGNS environment (Fluoronav™). It allows the surgeon to acquire fluoroscopic images, and map the position and orientation of surgical tools (that are being tracked by the IGNS system) to the fluoroscopic images.

2.3.5.2. Intraoperative Microscopy/Video

The intraoperative microscope has been a common tool for neurosurgery for many years.⁷⁵ Recently, they have been incorporated into the IGNS environment, enabling the surgeon to use the focal point as a virtual probe,⁷⁶ and to allow for pre-operative information (e.g. tumour segmented from pre-operative MRI data) to be superimposed into the microscope view.^{77,78}

One advantage of using the microscope central axis and focal point as a virtual probe is that the surgeon can use the microscope to follow a predetermined trajectory that was defined on the pre-operative image data. Superposition of pre-operative structures onto the microscope view also allows the surgeon to monitor the degree of brain shift by observing discrepancies between the pre-operative and intraoperative images.

Grimson demonstrated a novel system that superimposes 3D rendered images derived from pre-operative MRI onto intraoperative video.⁶⁴ This enables the surgeon to use the fused view to see a representation of target structures inside the head before the craniotomy, essentially providing them with a display commonly referred to as augmented reality. Pizani et al.⁷⁹ presented a similar system, which employed two video cameras to acquire stereoscopic video images, and a stereoscopic monitor to display the fused video/3D rendered image.



Figure 2-16: Fused video/MRI image of the author. The cortex can be seen within the head, and a tracked pointer can be seen touching the surface of the head. Using the stereo display, the sensation of depth improves the realism of the image.

2.3.5.3. Intraoperative CT

Pre-operative CT images are commonly used for surgical guidance. Butler et al.⁸⁰ have demonstrated a mobile CT system and radio-lucent head holder that can be moved into the operating room to acquire images during the procedure.

2.3.5.4. Intraoperative MRI

Intraoperative MRI offers the panacea of intraoperative imaging. It is probable that every neurosurgeon would find the ability to obtain high quality MR images at any point during a procedure useful. To that end, intense efforts have been made by many of the major scanner manufacturers to develop such systems, and many radiology and neurosurgery investigators have reported their experiences with such devices.⁸¹⁻⁸³ However, there are several obstacles to be overcome to allow a typical craniotomy based procedure to be performed under MRI guidance including:

- Allowing the surgical staff access to the craniotomy while the patient inside the magnet.

- Developing surgical and anesthesia tools that can function within the high magnetic field environment.
- Making the cost of a surgically dedicated MRI scanner and associated tools affordable.

These efforts have led to several approaches. General Electric has introduced a redesigned super-conducting magnet scanner that contains gaps in the center of the magnet to allow access to the patient (Figure 2-17a). This approach is often referred to a “double doughnut” design. Among other manufacturers, Marconi (formerly known as Picker) has demonstrated a design using a vertical magnet (Figure 2-17b), allowing access on one side. One of the original design goals of this latter example was to provide a less confined environment for the patient during diagnostic studies to prevent claustrophobia, but this design also allows for intraoperative use.

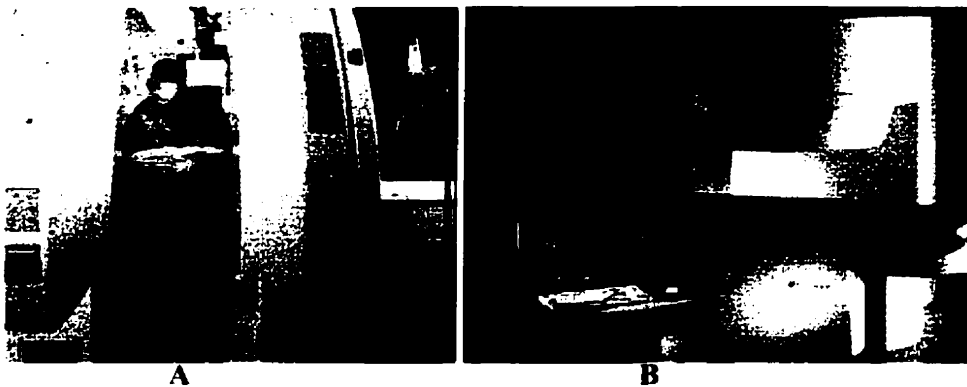


Figure 2-17: Two examples of “open” magnets designed for interventional MRI procedures. A: General Electric double doughnut design. B: Marconi static field flat magnet design.

Using a method analogous to that of Butler, Sutherland et. al.⁸⁴ reported on a MRI scanner attached to a ceiling mounted gantry which allows it to be brought into the operative field for image acquisition, and subsequently removed to allow the procedure to continue. This partially addresses the issue of accessibility to the operative field in that

the surgeon need not stand inside the scanner while operating, but requires that the surgical staff suspend the procedure while the scanner is moved into place, images are acquired and the scanner is removed again.

2.3.5.5. Intraoperative US

Long before the advent of frameless IGNS, intraoperative ultrasound was used routinely for procedures including gynecology and obstetrics and abdominal surgery. In addition, its use in neurosurgery is well established.⁸⁵⁻⁹² A detailed overview of US including relevant theory and a review of the literature relevant to its use in neurosurgery is presented in section 2.5.

The advantages of using ultrasound in the operating room are its universal availability in neurosurgical hospitals, its mobility, as well as its low space requirement. It provides images of reasonable quality and typically costs 5-10% of an intraoperative MRI system. Many US scanner manufacturers have recently developed US probes optimized for neurosurgical use. Such systems have relatively small scan heads (under 1cm²) and because the transducer can be placed over the volume of interest, provide impressive images of the brain

2.3.5.6. Intraoperative Endoscopy

Endoscopy is another intraoperative imaging modality to have recently entered the neurosurgical arena^{87,93-95}. Using light guides and miniature video cameras, it provides surgeons with a live visual image of the operative site while minimizing the size of the craniotomy. Endoscopes have been combined with stereotaxy by attaching them to stereotactic frames⁹⁶ or by tracking them as another tool, allowing their position and orientation to be visualized on pre-operative CT or MRI.

Recently, several investigators have reported incorporating endoscopes into the IGNS environment by connecting them to a tracking device^{28,44,97} and using “virtual reality” displays such as a head mounted display⁹⁸. These can aid the neurosurgeon in identifying the anatomy within the endoscopic view by displaying the endoscope’s position within the MRI or CT volume. The surgeon must be aware however, that if the brain tissue has moved during the procedure, the position of the endoscope as displayed on the pre-operative data may be incorrect.

2.4. Tissue Movement in Neurosurgery

2.4.1. Introduction

As explained in section 2.3.4.5, brain tissue movement is a significant source of error in IGNS. Many investigators are developing various approaches to measure and characterize the problem. If the movement can be characterized by a few simple parameters (e.g. CSF pressure, patient orientation), these parameters can be employed to predict the shift in cases where direct measurement may not be possible.

2.4.2. Measurement Methods

There are two basic approaches to measuring brain shift. First, one of several methods (described below) can be employed to measure the position of the cortical surface. Secondly, a tomographic imaging technique. MRI, CT or Ultrasound can be used to obtain images of the structures that lie below the surface. In either case, the intraoperative measurements can be compared to pre-operative image data to measure the deformation.

2.4.2.1. Surface Based Methods

One of the first indications of brain shift is the visible movement of the cortical surface after performing a craniotomy. The most obvious way to quantify such brain shift is by measuring the position of the cortical surface, and comparing this to the surface derived from the pre-operative data. The problem of measuring the surface of the cortex is similar to that of measuring the skin surface for patient-to-image registration. This similarity permits the same tools used for the registration problem to be used in the surface measurement problem.

Discrete Point Sampling

The simplest approach is to use the IGNS probe to obtain discrete samples of the surface, and to map these to homologous points on the pre-operative data.^{71,99} Other investigators have approached this task with a tracked operating microscope.⁷²

Laser Range Sensor

In addition to the above methods, another surface-based approach is to obtain cortical surface range images using a laser range sensor. Such a device, whose position is known in the tracker frame of reference, can be used to obtain profiles of the cortical surface. These profiles, combined with a finite-element model approach to characterizing tissue movement, can be employed to estimate the movement of structures below the surface itself.¹⁰⁰

2.4.2.2. Tomographic Methods

The other approach to measuring the movement of brain structures during surgery is to acquire intraoperative images of the structures themselves, and compare them to their position obtained from pre-operative data. Many intraoperative imaging techniques

described earlier can be employed for this task. Two that have been reported to date use intraoperative MRI and ultrasound.

Intraoperative MRI

Although intraoperative MRI is relatively new to the IGNS field, Maurer et al. have already reported on its use to measure brain shift.⁸³ They have obtained 3D volume data sets of the complete brain during surgery. The accuracy of measurement may be limited however, by the potential distortion of the MR images acquired.

Intraoperative US

For many institutions, the availability of ultrasound has made it a useful tool to capture tissue movement. One of the first groups to incorporate intraoperative US into IGNS was Bucholz et al. who reported its use for correcting tissue deformation in neurosurgery.¹⁰¹

2.4.3. Pre-operative Image Restoration

Using measurements of tissue movement obtained from one of the above methods, the movement information can be used to estimate and characterize the deformation. This representation can be applied to the pre-operative image data to realign, or warp it to better represent the actual state of the tissue. The technique used to warp the data is dependent on the nature of the information available. If information regarding the movement of the cortical surface is available, a method of predicting or modeling the movement of the internal structures given this surface information is required. If tomographic information is available, a method of matching homologous features between the pre- and intraoperative information may be used to measure the

deformation, and a simple interpolation scheme may be used to characterize the movement, and subsequently warp the pre-operative data.

Modeling

Once the necessary parameters have been measured, a model is employed to predict the deformation. The complexity of the model is dependent on the information available. In cases where dense deformation information is available (e.g. intraoperative MR or US), a simple linear interpolation model may be sufficient. In cases where the deformation information is sparse (e.g. surface measurements), more elaborate models are required.

Edwards et. al.¹⁰² recently reported on a three component finite element model to predict deep structure movement. The components consist of rigid structures (e.g. bone), soft tissue and fluid cavities (e.g. ventricle). An energy function consisting of opposing forces of sample and model energy is constructed and applied to a series of grid nodes superimposed on the pre-operative image. Sample energy is derived from the sampled deformation information and increases with discrepancy from the model and the sample data. The model energy is derived from assigned mechanical properties of the three components segmented from the pre-operative image. Model energy starts at zero, and increases with increased deformation. A third term to prevent folding, or the overlapping of grid nodes is also applied. A conjugate gradient descent algorithm is used to minimize the energy function. The resulting deformation grid is applied to the pre-operative image.

Miga et. al.¹⁰³ reported on another model to predict the movement of internal structures based on gravity induced effects as well as measurements from cortical surface and/or intraoperative US information. It incorporates a more sophisticated mechanical model of the brain and differentiates between many anatomical structures.

The mechanical model employs consolidation theory and essentially treats the different brain structures as a solid matrix saturated with fluid. Thus, the model can account for mechanical changes due to changes in cerebrospinal fluid (CSF) volume, as well as the effects due to gravity and other mechanical loads which may cause CSF flow and pressure changes. In its current implementation, the mechanical properties of grey and white matter are modeled to provide a more accurate estimation of movement.

2D Warping

When deformation information is available beneath as well as on the surface of the brain, the models discussed above may be employed to estimate the deformation throughout the image volume. An alternative is to employ an interpolation scheme to estimate the deformation throughout the image. In many situations, a simple form of linear interpolation or a thin plate spline interpolant¹⁰⁴ may be used to represent the deformation over the image.

2.5. Intraoperative Ultrasound in IGNS

This section begins with a review of basic ultrasound theory, and proceeds with a discussion of its utility in the operating room. Finally, a detailed review of the literature is presented.

2.5.1. Ultrasound Theory

2.5.1.1. Introduction

Ultrasound imaging devices function by combining the known speed of sound in a medium, and the fact that when sound waves encounter an acoustic interface, they undergo partial reflectance. Knowledge of the propagation speed and the time interval

from emission to reception enables the distance from the transmitter and the interface to be calculated.

Figure 2-18 illustrates the basic operation of an ultrasound imaging system. Discrete ultrasonic pulses, typically a few cycles in length, are emitted by a piezoelectric crystal within the transducer. The sound pulses travel in the medium (tissue) until they encounter an acoustic interface, where the impedance coefficients between adjacent tissue types differ. For normal incidence, the reflection coefficient at an acoustic interface is:

$$IRC = \frac{I_r}{I_i} = \left[\frac{z_2 - z_1}{z_2 + z_1} \right]^2 \quad (2.9)$$

where I_r is the reflected intensity, I_i is the incident intensity, and Z_1 and Z_2 are the acoustic impedances of tissues 1 and 2 respectively. The reflected pulse travels back towards the transducer, where its signal is measured. The distance d from the source to the reflector can be calculated by:

$$d = \frac{tc}{2} \quad (2.10)$$

where t is the time from pulse emission to the time the reflection is received and c is the speed of sound in that medium.

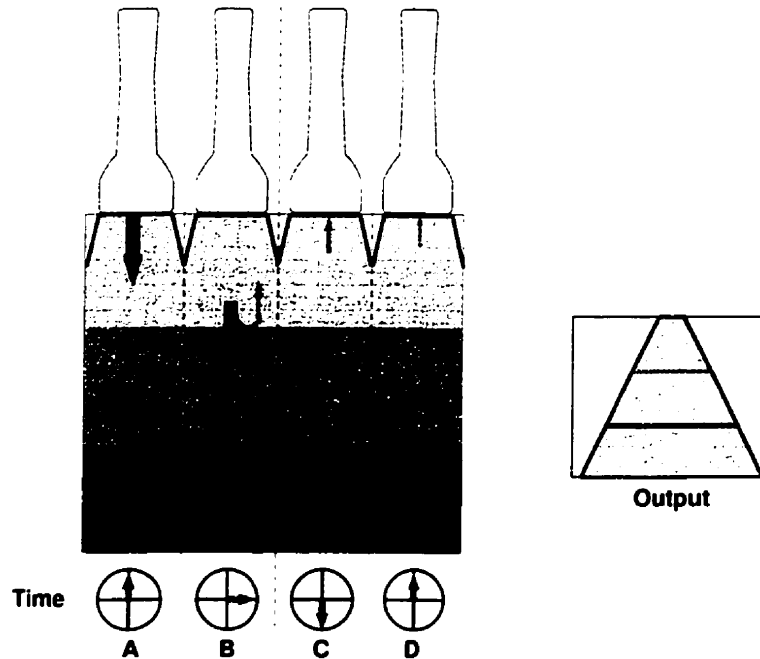


Figure 2-18: Illustration of the basic principle of ultrasound imaging. The transducer acts as both a transmitter and receiver. An ultrasound pulse is emitted at time A. At time B, the pulse encounters an acoustic interface, where it undergoes partial reflection. At time C, the attenuated pulse encounters a second interface. In the meantime, the first reflected pulse is measured by the transducer. Finally at time D, the second reflected pulse reaches the transducer. The received signals and the speed of sound in the medium are used to calculate reflector depths to generate an image.

As the sound pulse travels through the medium, its intensity decreases. This attenuation is primarily due to absorption of the sound waves in the medium (which is converted into heat), scatter and reflection; it is dependent on both the medium and on the ultrasound frequency, and thus is one of the factors governing the frequencies used for imaging. Figure 2-19 shows typical attenuation curves for ultrasound imaging frequencies in soft tissue. It can be seen that penetration is inversely related to frequency. In general, the attenuation coefficient of sound in soft tissue (expressed in dB/cm) can be approximated by:

$$0.5 * f \frac{\text{dB}}{\text{cm}} \quad (2.11)$$

where f is the frequency of the ultrasound pulse in MHz. The total attenuation (in dB) of sound of frequency f traveling a path of length L can thus be approximated by:

$$0.5 * fL \quad (2.12)$$

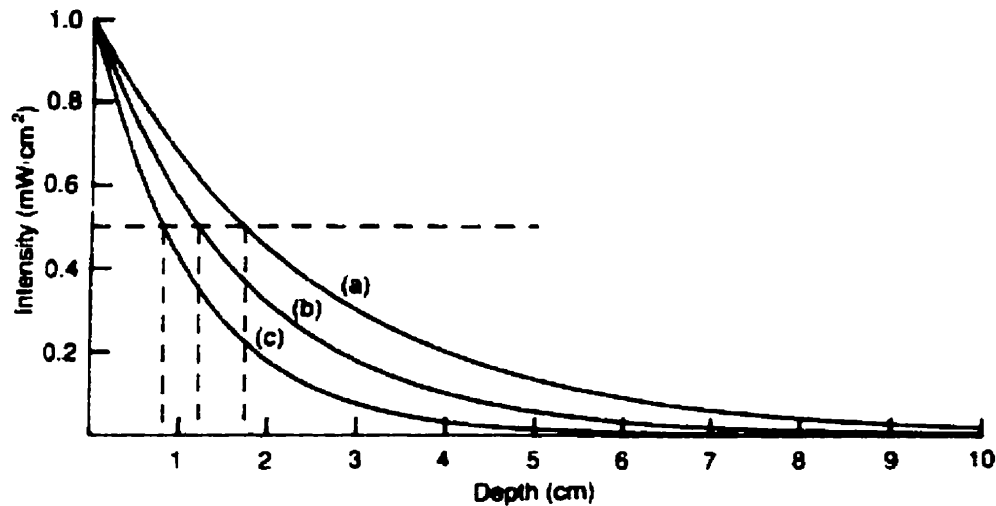


Figure 2-19: Intensity vs. depth curves for common frequencies ($a=3.5\text{MHz}$, $b=5.0\text{MHz}$, $c=7.5\text{MHz}$) used in ultrasound imaging, for soft tissue.¹⁰⁵ The depth at which the intensity is reduced by 50% is indicated.

Another important parameter that is dependant on ultrasound frequency is axial (or detail) resolution. Axial resolution represents the smallest gap between 2 objects along the direction of the pulse that can be resolved, as illustrated in Figure 2-20. The spatial pulse length and the electronics detecting the return signal limit axial resolution. The spatial pulse length is in turn limited by the sound frequency. Thus axial resolution improves as the frequency increases.

The two fundamental needs for ultrasound imaging compete with each other. That is, one must trade between the desire to image deeply located tissue (which favors low frequency waves) and axial resolution (which favors high frequency waves). To

accommodate these limitations, ultrasound probes designed to function in multiple operating frequencies are often employed.

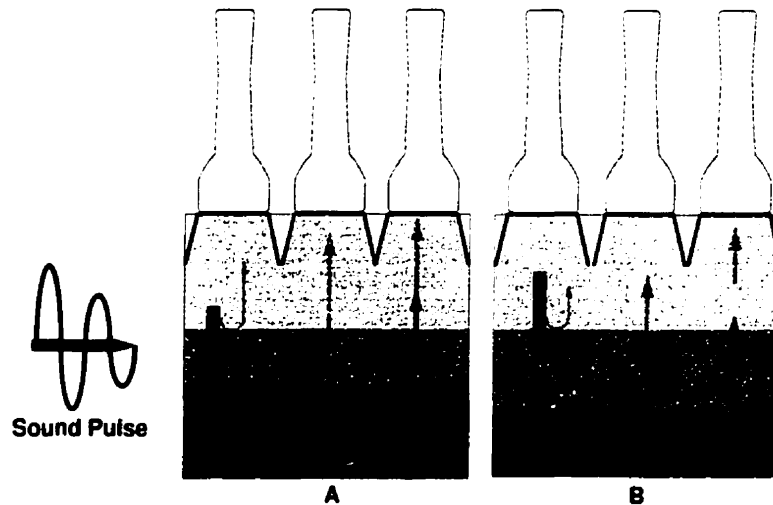


Figure 2-20: Illustration of the relationship between pulse length and axial resolution. A: The gap between the interfaces is less than half the spatial pulse length. The return echoes from the two interfaces overlap and cannot be distinguished from one another. B: The distance between the two interfaces is enough to ensure that the two returning echoes do not overlap and can be distinguished from one another.

2.5.1.2. Transducers

Much of the development work towards improving ultrasound imaging has been focused on the ultrasound transducer. Transducers must be designed to have the desired frequency and bandwidth for a given resolution while meeting the penetration requirement. A complete review of this field exceeds the scope of this thesis, so only the relevant points are given here.

Most modern ultrasound transducers consist of multiple crystals positioned in an array. Among the varieties of transducer, the phased array is best suited for neurosurgical use. Phased array transducers typically have small scanheads, and use delay generators to control the crystal firing to both steer and focus the beam (Figure 2-21).

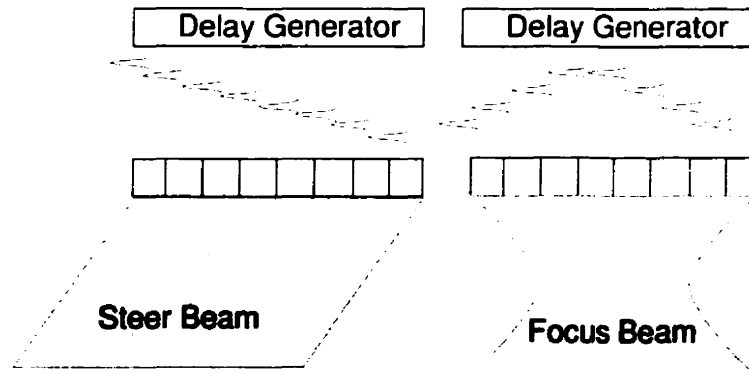


Figure 2-21: Illustration of how a delay generator can steer and focus a beam using the array of crystals found in a small mall face phased array transducer.

2.5.2. Integration of Ultrasound in IGNS

2.5.2.1. General Setup

When the surgeon or radiologist employs the US transducer to image the patient, its position and orientation determines the tissue volume imaged. The image itself can then be thought of as being rigidly fixed with respect to the transducer, and thus treated as a virtual tool (see Figure 2-12). Figure 2-22 shows how an US system can be incorporated into an IGNS system. The transducer is rigidly fixed to a tracked tool holder while the output of the US scanner is fed into the IGNS system, usually via a video frame grabber. When an US image is acquired by the workstation, the tracking device is interrogated, and the position and orientation of the tracked tool holder is obtained and tagged to the image. If the patient has been registered to a pre-operative data set as described earlier, then Equation 2-4 can be used to map the US pixels to the pre-operative image data.

Each time an US image is acquired, the homologous co-planar pre-operative image plane can be extracted from the pre-operative image data and displayed along with

the US. Trobaugh et al.⁴⁵ introduced the idea of correlating intraoperative US with pre-operative CT or MRI. Their first report described a technique to display US and co-planar MRI images during neurosurgical procedures. They also showed an example where the structures from the intraoperative US and pre-operative MRI did not line up. They presented several possible explanations, including the possibility of brain tissue shift during the procedure. Trobaugh and Bucholtz later presented an updated version of the system which employed image fusion to improve the intraoperative display¹⁰⁶ as well as techniques to realign the pre-operative image data.¹⁰¹

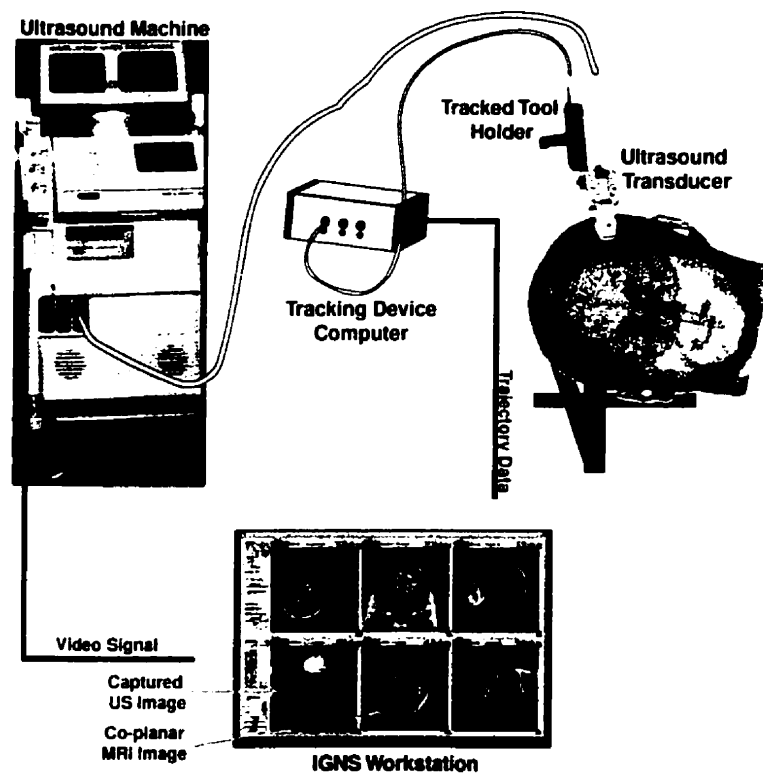


Figure 2-22: Illustration of how intraoperative US may be integrated into a typical IGNS system. The US image may be regarded as a virtual pointer, where the central axis of the image may be regarded as the pointer's axis.

Galloway et al. presented an IGNS system at the same time that included intraoperative information such as live video and intraoperative US.⁹⁷ Other investigators have either presented similar systems,⁴⁴ or described how intraoperative US was incorporated into a frame based stereotaxy environment.⁴⁶ In all of these, it was ultimately possible to map the US pixel to homologous pre-operative image pixels.

2.5.2.2. Calibration Techniques

Recalling equation 2-3, any coordinate in probe (or more generally, tool) space can be mapped to the pre-operative space as long as the transformation from tool to tool holder space, h_pT , is known. Several investigators have presented methods of determining h_pT .

Trobaugh described a technique of determining this calibration,⁴⁵ which requires that the transducer be tracked while acquiring several images of a single point, in this case a wire cross in a water phantom. The point is identified in each image, and transformed into a common space. This enables one to treat the points as if they were all part of a single composite image. With these points, a Gram-Schmidt orthogonalization is performed to find the least-squares solution, yielding h_pT .

A similar technique was reported by Detmer¹⁰⁷ and more recently by Hartov,⁴² with only slightly different mathematical techniques employed to solve the system of equations. Georgi recently reported a similar approach, where a brass bead was used instead of a wire cross.⁴⁶

A different calibration phantom was described by Prager et. al,¹⁰⁸ which employs a single brass bar target and special transducer holder. The special holder rigidly fixes the

transducer to a brass bar target and constrains the movement of the transducer with respect to the brass bar to orientations that maintain the position of the brass bar to the center of the US slice. The use of such a line target allows for reliable automatic identification of the bar in the US image. The authors report that the entire calibration procedure can be performed in a few minutes.

2.5.2.3. Display Techniques

Once US images are acquired in such a way that their position and orientation in pre-operative image space is known, various visualization techniques to compare pre- and intraoperative images may be employed. In most of the reports of intraoperative US integration into IGNS, little or no information is provided about the display techniques of presenting the data to a surgeon. Many groups simply present intraoperative US images paired with co-planar pre-operative images.¹⁰¹ The assumption is that made that these images are displayed simultaneously on the IGNS workstation. While this is already a significant achievement, simple yet useful tools can also be employed to improve the operator's (surgeon) ability to compare the pre- and intraoperative information. These tools include image blend overlays and feature extraction overlays.

The blending method involves selecting all or part of the two images and applying a blending function to obtain a composite image. The blending function can be a simple mask (OR blend) or a more complex blend. Figure 2-23 shows two simple blending examples applied to co-planar US and MRI images. First, a 50-50 blend is applied to obtain a composite image (Figure 2-23 B) where features from both images are shown. Despite the use of a different colour in the US image, it is difficult to distinguish the features between the US and MRI. In Figure 2-23 C, a simple OR function is applied. Despite the fact that the US image completely obscures the underlying MR image, the resulting composite image is less cluttered and thus easier to interpret.

An alternative to blending is to extract salient features from one image and display representations of these on the other. A simple example is to extract an edge of a ventricle from a US image and displaying that edge as a solid line on the co-planar MRI (Figure 2-23 D). This helps to provide a concise display of the relevant information obtained from the intraoperative US while maintaining a good view of the MR image.

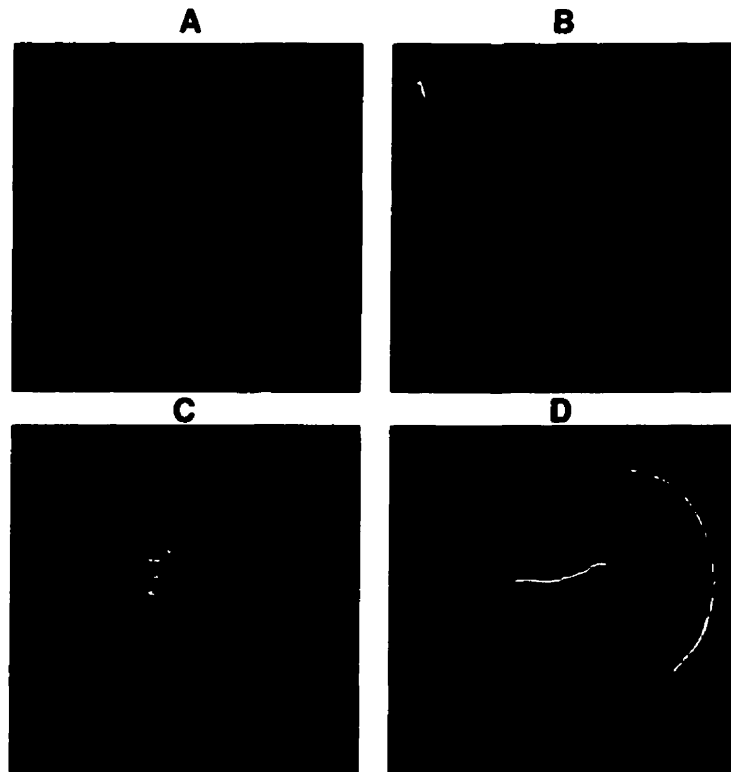


Figure 2-23: Examples of common data overlay techniques applicable to superimposing intraoperative US onto co-planar pre-operative MRI. A: Original MRI image. B: MRI with a US image displayed within a box. A 50-50 blend is applied to prevent the US from completely obscuring the underlying MR image. A separate color is also used to help the viewer to distinguish between US and MR features. C: MRI with opaque US image (OR function) superimposed on the MR. While the underlying MR image is obscured, the image is less cluttered. D: MR image with a yellow curve representing the outline of the ventricle obtained from the US.

Chapter 3

Intraoperative Ultrasound IGNS System Description

3.1. Introduction

This chapter describes all the hardware and software tools that were developed as part of this project. It begins with a description of the IGNS hardware setup as it is used in the operating room. A detailed description of the software follows, and finally, the design and construction of the phantoms used for calibration and validation are presented.

3.2. Operating Room Hardware Setup

3.2.1. Introduction

Although a complete and functional IGNS system was developed as part of this work, it is typically used in tandem with a second system in the operating room. The second system is a commercially available product (SNN Scout, SNS Inc, Mississauga ON) routinely used in our hospital. This maintains a “gold standard”, or reference system, that is independent of the research system. This ensures that the surgeons always have a consistent and reliable guidance system regardless of our research activities. Although the reference system does not require the presence of the US based IGNS equipment, the logistics of the setup (described below) require that the patient head tracker and the pointer be shared between the two systems.

Figure 3-1 illustrates the interconnections of the equipment in the operating room. Computer system A represents the reference system, while computer B represents our US based IGNS system. Both systems are connected to independent tracking devices (Polaris Tracker, Northern Digital, Waterloo ON). The Polaris consists of a position sensor camera, a tool interface unit (TIU), and one or more tracked rigid bodies, referred to as trackers. Both systems share 2 trackers. One is rigidly fixed to the head holder (thus the skull) while the other is attached to a pointer. Each tracker may only be connected to a single TIU at a time, however, they can be switched from one TIU to the other (dashed lines in Figure 3-1).

3.2.2. Reference System

The reference system is the commercially available SNN Scout, comprising a computer workstation (Dell Computer Inc. Round Rock, TX), a Polaris tracking system including a patient reference tracker, referred to as a dynamic patient tracker (DPT), and a tracked pointer.

The Scout software includes all the required functions to transfer DICOM compliant image data from most imaging devices, register these images with the patient, and provide image based navigation during surgery.

3.2.3. US based IGNS system

The major components of the US based IGNS system are a computer workstation and frame grabber (Power Macintosh G3/AV, Apple Computer, Cupertino CA), a Polaris tracking system, and an ultrasound machine (Ultramark 9, Advanced Technologies Laboratories Inc., Bothwell, WA). As our tracking device can monitor the position and

orientation of three trackers simultaneously, our setup assigns the three trackers to be the patient head holder, pointer, and the US transducer.

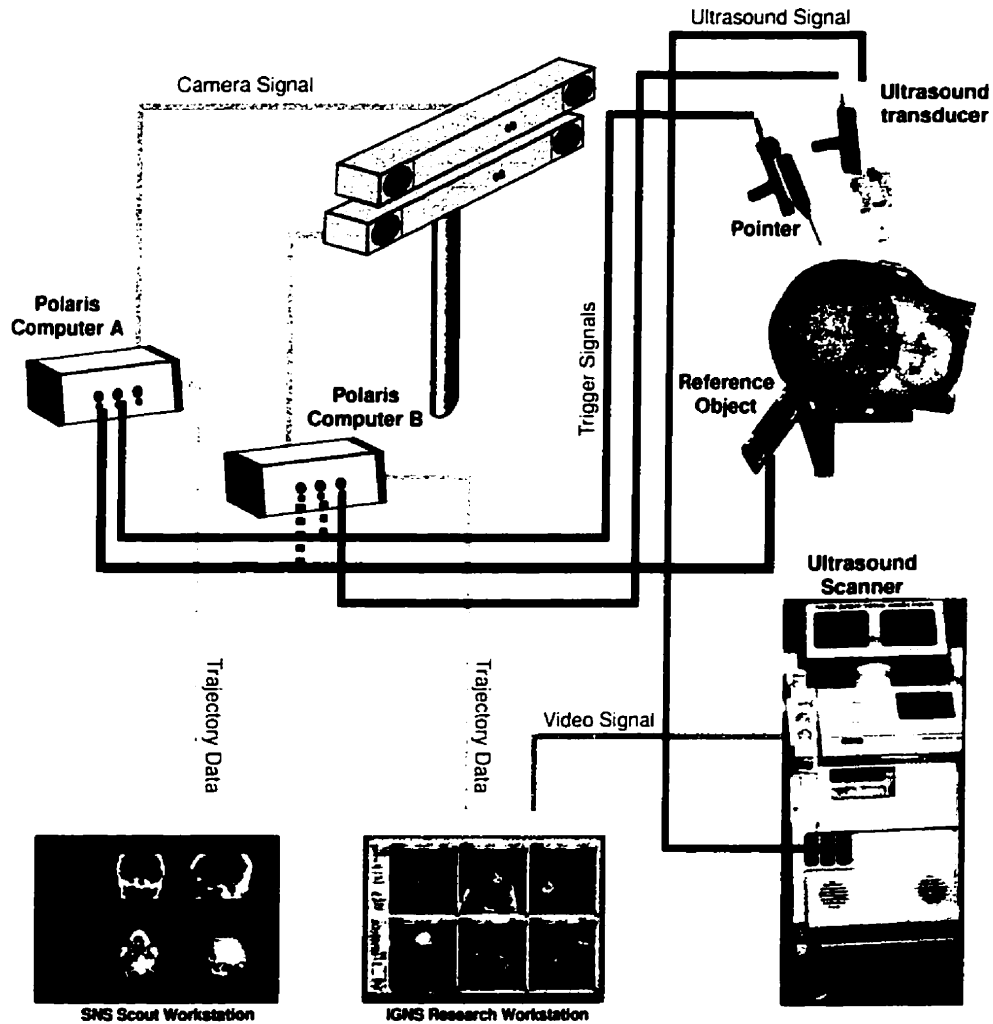


Figure 3-1: IGNS system organization as used in the operating room. Two independent computers and tracking devices are used to preserve a "gold standard" system. Both systems share the tracked pointer and reference object, while only the US based system monitors the tracked US transducer.

The US transducer is an ATL P7-4 multi-frequency probe. It is rigidly attached to a tracker via a custom tool holder (Figure 3-12). The NTSC video output of the US system is connected to the workstation frame grabber, while the output of the tracker

computer is connected to the workstation via an RS232 serial port. This allows the workstation to acquire US images while monitoring the position and orientation of the tracker rigidly attached to the US transducer. Using the patient→image registration (T) and an US→tracker calibration explained below, equation 2-4 can be used map the intraoperative US image to the pre-operative MRI images for comparison.

3.3. IGNS Software Package

3.3.1. Introduction

The overall goal of the IGNS application is to enable the surgeon to use the US images in as useful a manner as possible, while minimizing the extra time required to setup and operate the system during surgery. The software to accomplish this goal was developed in a modular form, and is roughly categorized into components to manipulate data, user interface (UI) components to enable the user to control the data processing functionality, and visualization components to display the images. Because the efficiency of use of the software impacts on its suitability in the operating room, UI designs which promote time-efficient use are also discussed here. Figure 3-2 shows a typical screen shot of the US based IGNS software. The highlighted areas are referred to in the following discussion.

All software was written in the object oriented development language C++ (Metrowerks, San Antonio TX). This enables one to design and implement functionality as a class hierarchy. That is, a series of objects that perform similar functions can be grouped in such away that common functionality is defined once in a parent class, while unique functionality may be implemented where required in subclasses, which inherit the common functionality of their parent class. This technique, called abstraction, allows for different classes to refer to one another through reference to their parent classes. Thus,

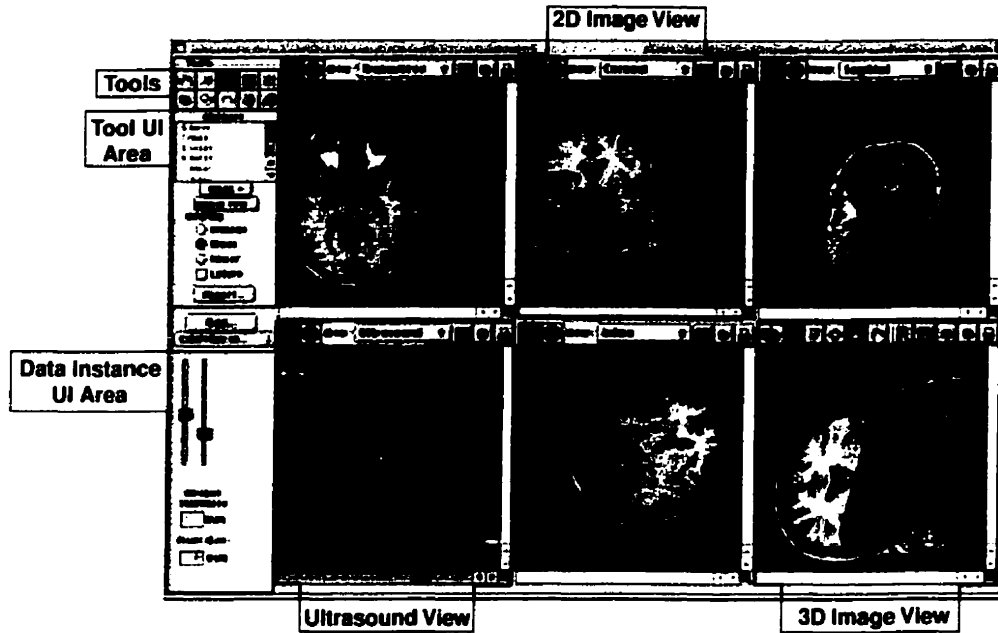


Figure 3-2: Typical screenshot of US based IGNS system with key software components highlighted.

one software module can refer to a variety of different objects that are inherited from a common abstract class. For example, a class of objects called *shape* may be defined. Subclasses called *square* and *circle* may be defined using *shape* as the parent class. The parent class may define a function called *draw*, but each subclass, *square* and *circle*, will implement *draw* in a different way. Another part of the software which manages all the objects to be drawn only needs to refer to the *shape* class, as all it may need to do is to call the *shape*→*draw* function. The appropriate implementation for the *square* and *circle*'s *draw* function will be invoked as they override the parent's *draw* function. Such abstraction simplifies the design and development process, and is used extensively here.

The software organization can be broken down into 4 sections (Figure 3-3). The image data section deals with image file I/O and image data management, such as managing voxel look up table (LUT) controls and video data stream control. The image process section deals with 2D and 3D rendering of the image data, including generating tri-planar and oblique multi-planar reformatting (MPR) images and converting the video

stream into an oblique image plane. The tools provide much of the user interaction facilities including the manual pointer, annotation, segmentation and deformation grid creation/control functions. Finally, the image display section interfaces with the image process and tool modules to provide the actual 2D and 3D display of the images and tool representations, as well as the user interface functions to manipulate them.

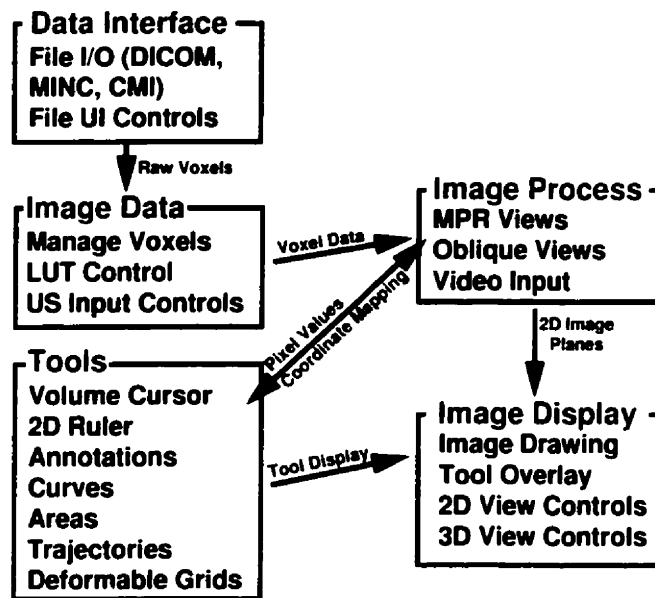


Figure 3-3: Software organization chart.

3.3.2. Image Data Module

The image data module consists of a series of objects that interact to load, store and manipulate the image information as a whole. They provide the functionality for the user to input images from a variety of data formats including file based CT or MRI, and video based US. It enables one to manipulate the presentation of the data through colour lookup table (LUT) controls, and provides a level of abstraction for other software modules by defining a common internal representation of the data, regardless of whether its source is a file or a video stream.

3.3.2.1. Data Interface Object Class

The data interface object defines the way that data-instance objects (i.e. those that ultimately manage the images once loaded) obtain image information from several image file formats. Objects inheriting from data interface objects present the user with a format specific user interface to allow for image selection. Certain file formats store volumetric data in the form of a sequence of individual slice files while others as a single file. Each data interface subclass implements format specific file handling functions to load the images and obtain information regarding the image dimensions and orientation, allowing it to be stored in a common orientation.

3.3.2.2. Data Instance Objects

The data instance object holds and manages the image information after it is read by the data interface object. It provides a means for other objects to query the image's dimensions and to obtain a pointer to the raw voxels. Image process objects (described below) interact with data instance objects to render visible representations for analysis or display. Data instance objects manage the UI required to allow the user to manipulate the LUT (window width/level) used to view the images (see Figure 3-2). In the case of video based ultrasound data, the UI required to control the video stream and input calibration information is provided.

3.3.3. Image Processor Objects

Image processors are the class of objects that perform 2D rendering using a data instance object as its source. Image processor objects do not manage any UI objects directly, but rather are managed by the image view UI tools described below, and rely on an internal messaging system to be notified when events of interest occur that might require a re-rendering of the image. Image processor objects are given a reference to a

data instance object, and maintain a list of objects that are to be notified when a new rendering event has occurred.

Figure 3-4 shows an example of how an image processor object makes use of the raw pixel information from a data instance and the 3D cursor coordinates from the volume cursor tool to render the familiar axial, sagittal and coronal views. Image display objects and 3D texture mapped objects (managed by the 3D image view object) “subscribe” to the image processors to be notified when a new rendered image is available. The image is fed down the data pipeline for 2D image display, or to update a 3D texture map in a 3D view.

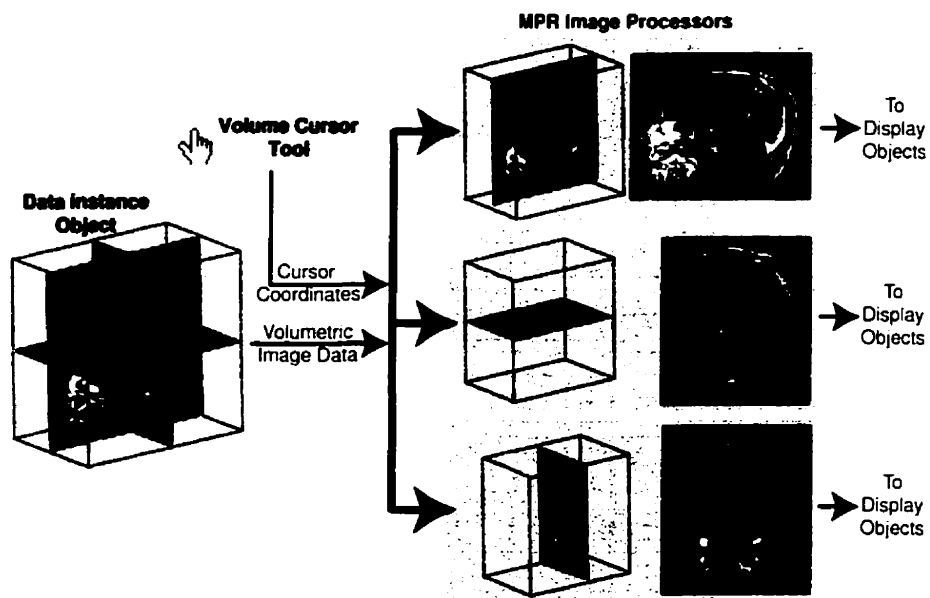


Figure 3-4: Example of image processor objects. The volume data instance object supplies the raw voxel data for the 3 multi-planar reformat (MPR) image processors. The image processors also employ the volume cursor coordinate value to determine where the 3 orthogonal planes to render lie in the volume. The results are passed down the pipeline to the image view objects for display on the screen.

Image processors also provide a means to transform coordinates from their 2D space to the 3D volume data space. This allows various tool objects (described below) to interact with the images produced from the image processors without requiring intimate knowledge of the individual image processors themselves. For example, if the user wished to click on a feature in the axial view to drop a 3D marker, the annotation tool would request the 3D coordinate from the abstract image processor by supplying the 2D image coordinate supplied by the mouse click. The exact nature of the image processor is irrelevant since all image objects share a common definition of the 2D→3D and 3D→2D coordinate transformation routine inherited from the base image processor class. This allows for rapid implementation of new tools, and for the introduction of new image processors without extensive changes to the other objects that may interact with them.

Several image processors have been implemented. These include standard tri-planar views, three orthogonal oblique views, live ultrasound and the deformed oblique view. The tri-planar views (axial, coronal and sagittal) are three orthogonal planes aligned with the planes of the voxel data, which represent the views the surgeon would most often see on traditional films. The oblique views are three orthogonal planes, two of which are parallel to the central axis of the tool (in-line & in-line 90), while the third is perpendicular to the tip of the tool. The central axis of a tool can be either the pointer shaft or the center line of a tracked US image. The live US image processor, as the name implies, simply contains the image obtained from the live US image acquired through the frame grabber. Finally, the deformed in-line view is similar to the in-line view, but can be deformed in the image plane by applying a piecewise linear deformation grid as explained below.

3.3.4. Image Display Objects

The image display objects are a collection of program modules that draw the image, coordinate the display of objects that have a representation on the screen, and manages the UI that permits the user to manipulate the display for a given task. Figure 3-5 shows the image display in the two basic modes of operation: 2D and 3D. In both modes, the UI displays the tools appropriate for that mode on a toolbar above the image.

3.3.4.1. 2D View Module

The 2D view module provides a window for bi-directional flow of information between the software and the user. The software communicates with the user by displaying one of the available images emanating from the image processors, along with

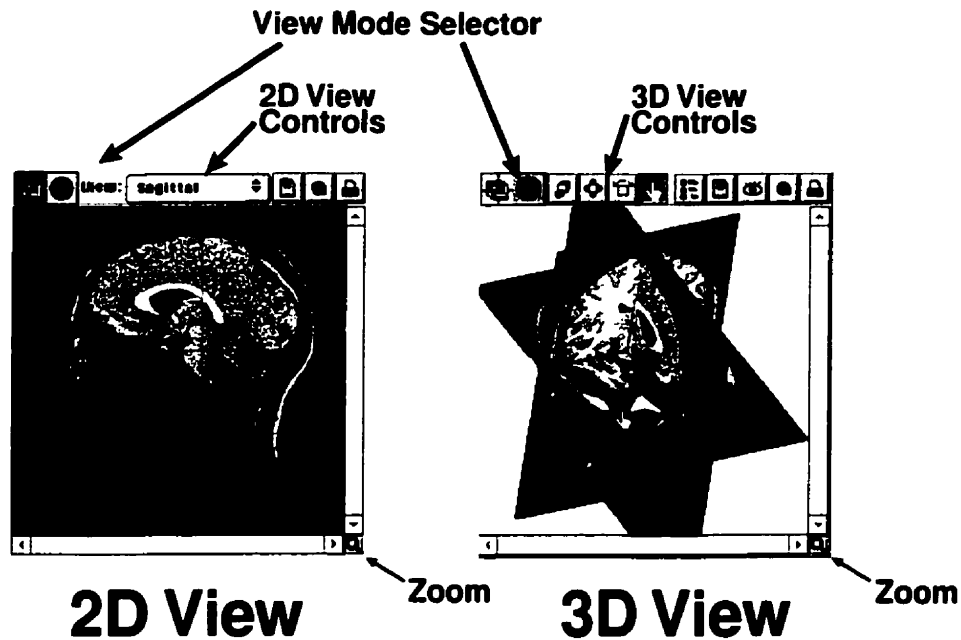


Figure 3-5: 2D and 3D image views. These objects coordinate the display of the image data and the display and user interaction with all other objects that require a representation on the images. They also manage the UI required to allow the user to manipulate the image display parameters.

representations of the tools, on the image. It also channels input from the user to the appropriate tool by monitoring mouse clicks within the display area and passing control to the tool to manage the interaction.

The user can manage the display by interacting with the 2D view controls. They allow one to select which image to display, control magnification, and direct its output to a printer, a file, or accumulate it as a frame in a QuickTime™ movie.

3.3.4.2. 3D View Module

This module allows the user to display 3D rendered versions of the image data, manipulate the image being viewed, and to a lesser degree than the 2D view, provides the bi-directional flow of information between the software and the user. Unlike the 2D view (with the exception of the cursor) the 3D view does not provide facilities to interact with tools.

The 3D view controls allow the user to select the objects to be displayed, to manipulate the 3D objects by allowing translation, scaling and rotation of the 3D view. The controls also permit the export of the 3D view into an external file, the printer or a QuickTime™ movie.

3.3.5. Tools

The tools are the primary interface between the user and the software. The user employs them to manipulate the cursor, annotate objects and analyze the intraoperative image data.

3.3.5.1. 3D Cursor Tool

The cursor tool provides the functionality to assign a point in 3D space to act as the location of a cursor. Input can come from the computer mouse by selecting a location on the screen, or from an external tracked tool, by pointing it to a structure on the patient. The latter function is used by the software in its IGNS mode. Before the system may be used in the tracked tool mode, a registration procedure must be performed to determine the transformation from patient to image space (${}^i T$ described in section 2.3.1). The volume cursor tool provides the functionality to perform such a registration.

Patient→Image Registration

The patient image registration tool provides the functionality and related user interface to enable the surgeon and operator to identify a series of homologous points on both the patient and image, and to calculate ${}^i T$, the rigid body transformation from the tracker space to the pre-operative image space.

The affine transformation is calculated using a Procrustes algorithm in common use in our laboratory¹¹⁶ and originally described by Sibson¹¹⁷. First, the centroid of each point set is calculated to determine the translation component of the transformation and to align the two point sets to a common origin. Second, if A and B are the two sets (with common origin), a rotation/reflection matrix Q can be obtained by solving

$$\min \| A - BQ \|^2, \quad (3-1)$$

which can be found through a singular value decomposition of $B^T A$.¹¹⁷ If

$$U^T (B^T A) V = \Sigma = \text{diag}(\sigma_1, \dots, \sigma_p), \quad (3-2)$$

where p is the number of dimensions, then the rotation matrix is given by

$$Q = UV^T \quad (3-3)$$

Finally, if required, a uniform scaling is calculated. These are combined to obtain the affine transformation, ${}^i T$.

The procedure requires that the operator and/or surgeon identify a series of homologous points, both on the patient with the IGNS pointer, and on the images on the workstation. It requires coordination between the surgeon and computer operator to ensure that first, the anatomical landmarks identified by the two of them are precisely the same, and second, that the landmarks are identified in the same order. The process of selecting points, evaluating the results and deciding how to improve the registration is iterative in nature, and requires some practice to achieve consistent results. It involves close communication between the surgeon and operator, and often requires that sampled points be discarded and re-sampled, either due to miscommunication, unintended movement of the IGNS pointer, or error in identifying landmarks. In a practical sense, the process is performed early in the surgical procedure, and often under some time pressure since many of the operating room staff must wait for this step to be performed before continuing to prepare the patient. For this reason, the user interface is optimized to minimize time spent.

Typical Usage Example

Referring to Figure 3-6, the registration process proceeds as follows: Pre-operatively, anatomical image points are selected on the image data using the annotation tool (described below). In the operating room, the operator selects each point on the list, and calls it out to the surgeon. The surgeon moves the tracked pointer to the appropriate

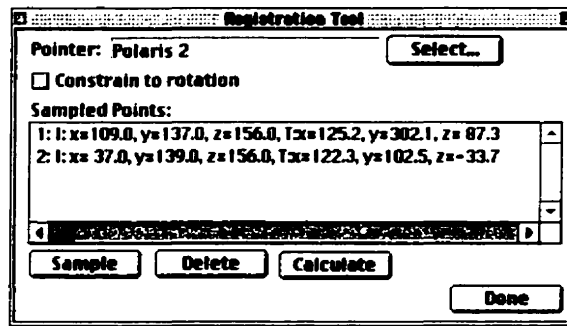


Figure 3-6: Registration Tool Interface.

anatomical location on the patient and notifies the operator, who at that time acquires a point pair by selecting the “Sample” button. The two sets of coordinates appear in the “Sampled Points” list confirming the acquisition. When all the points are selected, the transformation may be calculated and stored by selecting on the “Calculate” button. If the operator is unhappy with any acquired point, it may be discarded by selecting it on the list and clicking the “Delete” button.

After a transformation is saved, a visual check of the registration precision is performed. This step requires that the surgeon place the pointer tip on the skin surface at various locations around the head, while the operator evaluates the distance from the cursor location and the skin surface. If the registration is found to be acceptable, the procedure may continue. Otherwise, the surgeon or operator may decide to delete points, add new points, or repeat the entire registration.

3.3.5.2. Point Annotation Tool

The point annotation tool provides the functionality required by the user to “drop” markers at specified locations within the image volume. This can be achieved by first selecting a location with the cursor (either in mouse mode, or tracked tool mode),

switching to the annotation tool, and pressing the  button. The user is then prompted for a label for the annotation.

At certain times during the operative procedure, a series of points must be acquired as a group (e.g. skull or dura surface points to define the craniotomy). In order to minimize the time required to accomplish this, a “rapid fire” acquisition mode is employed. The operator is asked to provide a prefix string and starting index number. When the  on the window is pressed, an annotation is created at the current cursor location using the concatenation of the prefix and index number as the label. The index is automatically incremented in preparation for the next point. This allows the surgeon and operator to drop a series of points with predetermined labels in a short period of time.

Point annotations are displayed as **x** markers on the 2D screens with their labels drawn next to them. The user may alter the display rules for the 2D view to control the screen clutter. The labels may be toggled on and off, and the user may choose to display all points as they project onto the image plane, or restrict the display to points that lie within 2mm of the image plane. In the 3D view, they are displayed as small spheres, without labels. The annotation tool control maintains a visual list of all annotations. When the user selects one from the list, it is identified by colour changes in both the 2D and 3D screen.

3.3.5.3. Trajectory Annotation Tool

The trajectory tool functions in much the same way as the point annotation tool described above. The exception is that instead of storing a simple coordinate along with a label, a 4x4 matrix containing the location and orientation of the tracked tool is stored.

When selected in the list, both the location of the cursor and orientation of the oblique views are set to that of the trajectory.

In the 2D views, the trajectory is displayed in the same way as the point annotation, with an **x** and the label. In the 3D view, the origin is displayed with a sphere (in the same manner as an annotation) and in addition, an oblique line is used to display the orientation direction as well.

3.3.5.4. Spline Curve Annotation Tool



In certain circumstances the edge of a structures (e.g. ventricle) must be delineated. The spline curve tools allows the user to draw and edit smooth curves on the in-line and ultrasound (see Figure 3-2) views.

The curves consist of multi-segmented cubic splines¹⁰⁹ employing the Hermite polynomial blending functions, with the additional Katmull Rom constraint of having the tangent directions at each knot P_i parallel to the line connecting points P_{i-1} and P_{i+1} (Figure 3-7).

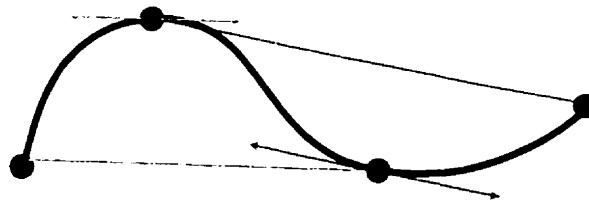


Figure 3-7: Multi-segmented Hermite polynomial using the Katmull Rom constraint. The tangent direction at each knot is parallel to the direction of the line between the neighboring knots.

3.3.5.5. Filled Region Tool



In addition to markers, trajectories and structural boundaries, areas, or regions must be identified or segmented in order to be able to classify them in the image correction procedure described below. The filled region tool (Figure 3-8) provides the functionality to achieve this. The tool employs closed versions of the Hermite polynomials described above to define a boundary, and a point annotation to define a seed to identify the interior of the region.

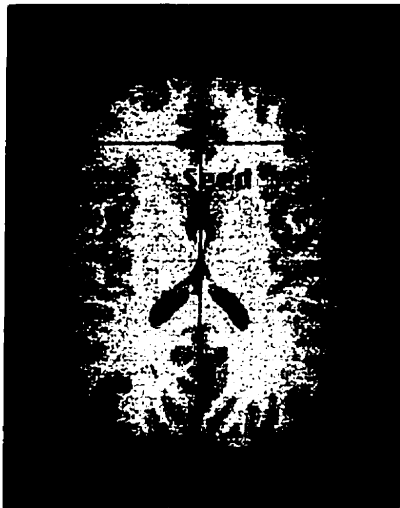


Figure 3-8: Example of a seeded fill to identify the area that corresponds to brain in the MRI image. The boundary is defined using a closed multi-segmented Hermite polynomial.

3.3.5.6. Ruler Tool



The ruler tool provides a means to measure straight-line distances. The user brings the mouse pointer to the start point and click-drag the mouse to the end point. The computer displays the line between the start and end points, while displaying the distance in mm in between them.

3.3.5.7. Region of Interest Overlay Tool



The region of interest tool is one of the most useful in the US based IGNS system. It enables the surgeon to define a rectangular region of interest (ROI) on either the in-line

view or the US view, and superimpose the homologous region from the other window. For example, an ROI can be defined on the oblique MRI view and that region from the US view can be superimposed over the co-planar MRI. Furthermore, the surgeon can interactively drag the ROI over the image with the mouse, effectively “revealing” intraoperative images over the pre-operative ones. This interactive motion enables the surgeon to obtain a concise qualitative appreciation of the differences between the intraoperative and pre-operative images.

Figure 3-9 gives an example of the ROI tool in use. The left image shows an oblique MRI whose orientation is identical to that of a live US image acquired with the IGNS system, while the right presents the same MRI with a rectangular ROI which contains the intraoperative US image. The ROI can be moved around over the image to provide the surgeon with an animated “before” and “after” deformation view.

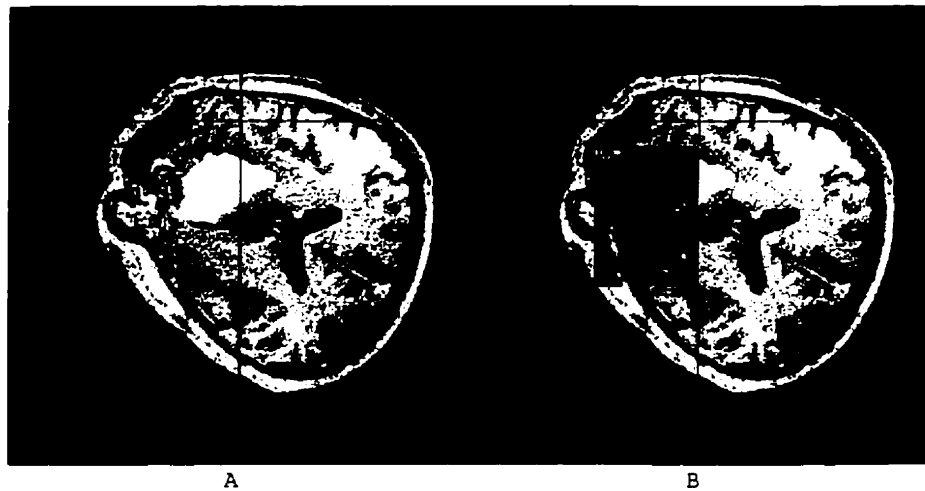


Figure 3-9: Example of the ROI overlay tool. A: Oblique view of an enhanced MRI showing enhancement of a tumour. B: Same oblique MRI with a rectangular portion of the co-planar US overlaid in the region of the tumour. In use, the window is able to “move” over the underlying image.

3.3.5.8. Deformation Grid Warping Tool



The deformation tool allows the previously identified annotations (point and splines) to be classified into a list of pre and post deformation homologous points. It also provides the functionality to define a grid of arbitrary size and to superimpose it on the oblique display. The grid tool uses the homologous points to calculate initial displacement vectors and propagates the displacement to all grid nodes using the following iterative technique.

Step 1: For each initial displacement vector, locate and apply the displacement to the nearest grid node.

Step 2: For each displaced node, notify neighboring nodes of the displacement.

Step 3: For each node notified of a neighbor's movement, calculate a new displacement vector by taking the average displacement of all its neighbors, and flag itself as displaced.

Step 4: If either the maximum displacement is above the minimum stop threshold, or the iteration count is below a preset maximum, repeat from step 2, otherwise, stop.

A similar result would be expected using a thin plate spline algorithm described above, however this technique is more easily extended to improve the interpolation scheme with the addition of model based information (e.g. Edwards¹⁰² and Roberts¹¹⁰). The tool provides all the functionality to create, and define the grid, and communicates with the warped oblique image processor to display the results.

Deformation Grid Display

Several options have been incorporated into the IGNS software to show the displacement grid. The first is a simple mesh that is connected to each grid node (Figure 3-10). As the grid is deformed, the mesh changes with it (Figure 3-10B), showing how the intraoperative image would have to be deformed to match the pre-operative image. The second technique displays a vector at each grid node, where the vector starts at the displaced node location, and points back to the original location. This represents the direction the pre-operative image would need to take to correct itself to the intraoperative image (Figure 3-10C). Finally, a colour-coded display is available to view the magnitudes of the displacement at each point (Figure 3-10D).

3.3.5.9. Warped Oblique Display

The ultimate goal of the IGNS software is to permit the correction of the pre-operative image based on the calculated deformation field. The deformation grid is applied to the oblique view using bi-linear interpolation, yielding a piecewise linearly warped image (Figure 3-11).

3.4. Ultrasound Holder

For the IGNS system to track a particular tool, it must be rigidly attached to a tracker. In the case of the US transducer and the Polaris tracker, a removable, rigid connector has been constructed (Figure 3-12) to allow attachment without altering the transducer itself. It is constructed of aluminum and epoxy putty. The epoxy putty was used to create a form allowing the holder to precisely conform to the shape of the transducer handle.

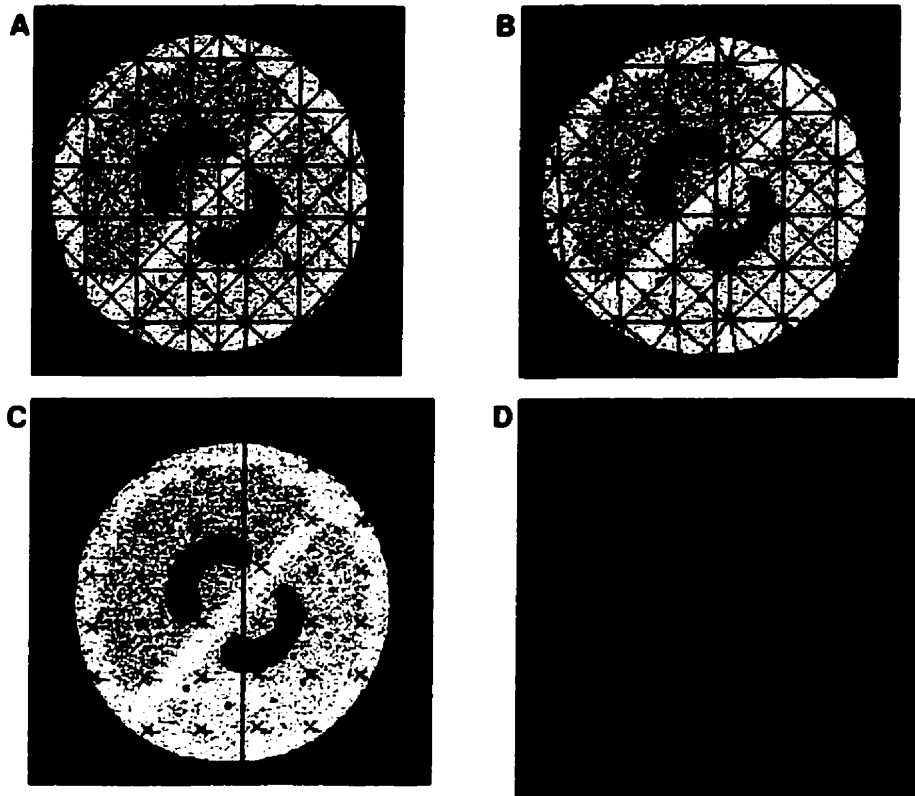


Figure 3-10: Different display techniques to visualize the displacement grid. A: A non-deformed mesh superimposed on an oblique image of a deformable brain phantom. B: Grid after deformation. The deformation represents how an intraoperative image would have to deform to match the pre-operative image. If the node points were pinned to the underlying pre-operative image and returned to a regular straight grid, the pre-operative image would be warped to conform to the intraoperative image in the process. C: Vector field showing the direction each node should take to correct the image. D: Magnitude display. Semi transparent colour coded display to appreciate the distribution of the magnitude of the deformation throughout the image.



Figure 3-11: Example of an oblique MRI of the deformable brain phantom after applying a deformation grid. The user may employ the ROI tool to evaluate the quality of the correction.

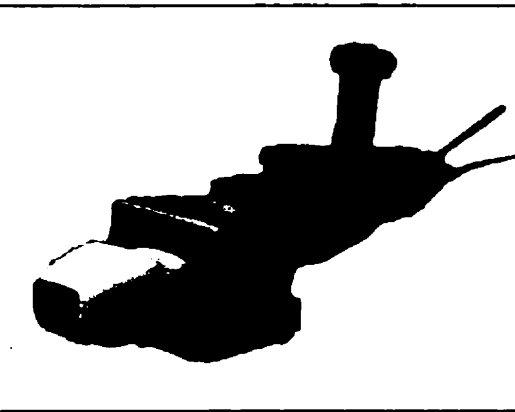


Figure 3-12: Close-up image of the P7-4 ultrasound probe, attached to a Polaris tracker using the custom holder.

3.5. Ultrasound Phantoms

Over the course of this work, several phantoms were required to characterize the US machine and frame grabber, calibrate the IGNS system, and to validate it. Many of these phantoms incorporated novel designs in order to overcome specific issues. This section describes the design and construction of the phantoms used in this project.

Brain simulating material: Poly(Vinyl Alcohol) Cryogel

For some of the work described here, we required a phantom that would simulate the imaging characteristics of brain tissue with US, MRI and CT, as well as exhibit

mechanical characteristics that were similar to that of the human brain. In addition, the material needed to be robust and stable over time. Poly(vinyl alcohol) cryogel (PVA-C) provides these qualities. This material is first prepared as a viscous fluid, which is then poured into a mold, and subjected to repeated freeze/thaw cycles. The mechanical properties of the PVA-C (along with the T1 and T2 MRI characteristics as well as the speed of sound)^[11] may be altered by varying the PVA-C/water concentration of the mixture, as well as changing the number of freeze-thaw cycles to which the mixture is subsequently exposed. Provided the material is stored in a humid environment, it appears to be stable over time (at least 4 years, in our experience).

3.5.1. Calibration Phantoms

3.5.1.1. Introduction

As with other investigators (see section 2.5.2.2) a calibration phantom (or tool) is required to determine u_pT , the transform from the US image space to the tool holder (tracker) space. In general, this tool defines a target or series of targets in a sound conductive medium that must be imaged by the US device. The targets used by others include wire crosses or suspended beads. In each case, an assumption is made that the image is acquired such that the target is in the centre of US image slice in the perpendicular (slice thickness) direction. Because the US image is thick (5-10mm), partial volume effects make it difficult for the operator to position the US transducer so that the target was at the centre of the image slice. In order to minimize partial volume effects, we have adapted the Z-bar (or N-bar) fiducial marker commonly used in frame based stereotaxy for use in our US calibration phantom.

Figure 3-13 illustrates how the partial volume effect can contribute to positioning ambiguity in the US calibration phantoms. Using the Z-bar we make no assumption that a

target is in the center of the image. Rather, the intersection of the center segment of the Z-bar and the center of the slice can be calculated from the image (Figure 3-13C).

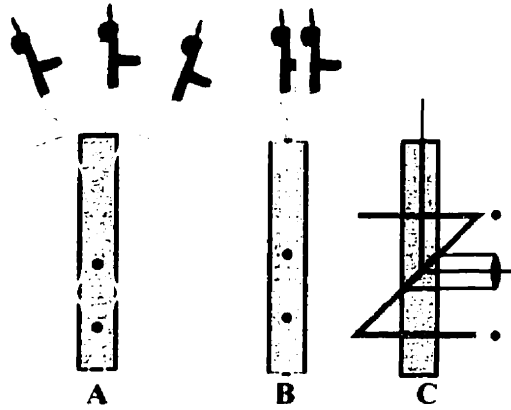


Figure 3-13: Illustration of the ambiguity that can arise when attempting to image a small, thin target with a thick US slice (partial volume effect). A: Rotation ambiguity. B: Translation ambiguity. C: Z-bar fiducial marker calculates the position of the intersection of the marker and the center of the slice, reducing partial volume effect.

The two design goals of the calibration phantom were to allow us to perform the calibration process in an accurate and reproducible manner, and to enable us to use it to measure the overall accuracy of the IGNS system. In order to achieve both goals, the phantom needed to be capable of being imaged by 2D US and 3D MRI or CT. Three such phantoms were designed, each building from the strengths and weaknesses of the previous one.

3.5.1.2. Calibration Phantom Version 1

General Description

The first phantom consisted of a series of hollow tubes protruding through two parallel Plexiglas plates. Holes drilled into the plates acted as guides for the hollow tubes. When in place, the tubes formed three Z-bar markers (Figure 3-14), each 5cm in length. The guide holes were made at known locations in the phantom frame of reference so that the locations of the Z-bar vertices could be calculated. The plates had four divot holes milled into them at known locations in phantom space, so that they could be identified with the IGNS pointer to determine the position of the phantom in tracker space.

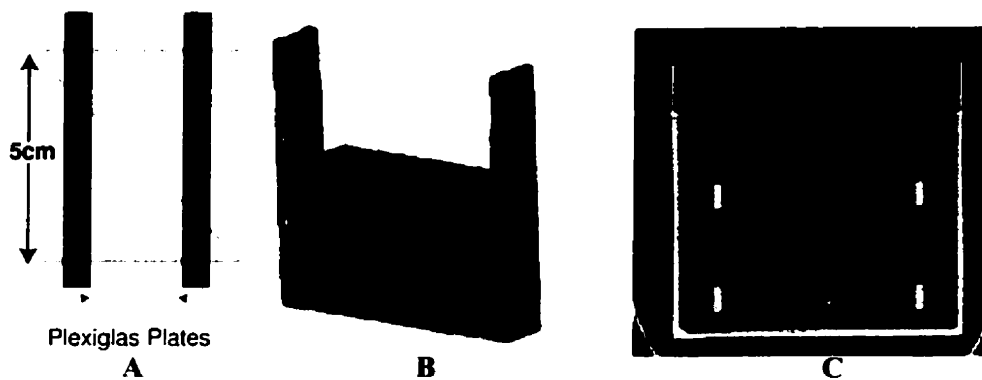


Figure 3-14: A: cross sectional illustration of the parallel Plexiglas plates and the guide hole pattern used to form a Z-bar fiducial marker. B: 3D volumetric reconstruction from CT of the calibration phantom showing the position of the 3 Z-bar markers. C: Cross section CT image of the phantom with the Z-bar markers intersecting the image highlighted in red.

The Z-bar tubes were filled with CT angiographic contrast agent (Iothalamate meglumine, U.S.P./ 60%) and the phantom placed in a water bath, where the speed of sound (1497m/sec) is similar to that of brain tissue (1510m/sec)¹¹². CT images were acquired with a Picker PQ6000 scanner to obtain a volumetric data set of the Z-bar markers, and the divot hole fiducials. For US imaging, the tubes were filled with the same water that is contained in the water bath. Care was taken to ensure that no air bubbles were left in the tubes.

Positive Results

In the early experiments, the phantom showed that the Z-bar fiducial marker was a good approach to minimize the influence of partial volume on calibration accuracy, and to simplify the overall imaging process. The ability to use the same phantom to measure the overall system performance was also found to be useful.

Negative Results

The phantom was weak in two areas. First, the US image quality, particularly in the diagonal segments of the vertically oriented Z-bars, was poor (Figure 3-15). It was often difficult to obtain a clear image of all the fiducial markers. The second limitation was in the size of the overall phantom. The spacing of the Z-bars prevented us from obtaining images of all the Z-bars at high image zooms. The lowest achievable maximum imaging depth (MID) was 10cm. The maximum imaging depth represents the distance from the transducer face to the most distal tissue displayed at the bottom of the screen. After some experience in the operating room, it became clear that calibrations at MID levels of less than 10cm were required.

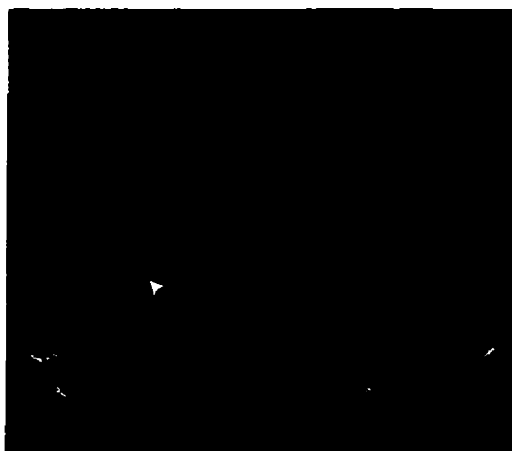


Figure 3-15: Example of an US image of the calibration phantom highlighting the poor signal from the center marker of the vertical Z-bar markers.

Center marker of vertical Z-Bar

3.5.1.3. Calibration Phantom Version 2

A second phantom was constructed to order to address the issues of the first calibration phantom. We hoped to enhance the first design to improve the US contrast of the fiducial markers, and to enable imaging using MID values more appropriate for intraoperative use.

The second phantom was constructed using Poly(vinyl alcohol) Cryogel (PVA-C)¹¹¹. This material was also used in the deformable phantom described below. It was hoped that this material would provide better US image contrast of the vertically oriented Z-bars and simplify handling since the phantom would consist of a relatively solid block of material and not require the water bath. The speed of sound in PVA-C (as used in the phantom) is 1530 m/sec, close enough to the average of that of soft tissue and of brain (1540 and 1510 m/sec respectively) for our needs.

Construction

The construction of the phantom was performed by the technical personnel at the Roberts Research Institute according to the author's specification. Cylindrical strands (2mm diameter) of PVA-C were formed in Plexiglas molds. They consist of 15% PVA-C by volume, and were subjected to 3 freeze/thaw cycles. The strands were held in position by 2 parallel plates similar to those used to hold the hollow tubes of the 1st phantom described above. The guide holes for the Z-bar strands were laid out according to Figure 3-16A. The vertical Z-bars were slanted inwards by 15° to taper them in towards the top to prevent the upper markers from being excluded from the US image. Once fixed in place, 10% PVA-C was poured to fill the space between the plates, and completely immerse the PVA-C strands. After allowing the liquid to stand to allow any air bubbles to rise to the surface, the assembly was subjected to a single freeze/thaw cycle. Once thawed, the support plates were removed, and the entire block was immersed in a final bath of 10% PVA-C within a Plexiglas container, which also had 8 divot holes milled into it for use during registration as described earlier. This volume was then subjected to a final freeze thaw cycle, and the resulting container and PVA-C within constituted the final phantom.



Figure 3-16:A: Cross sectional view of the phantom. The image shows intersection of the two horizontal Z-bar markers and the two slanted vertical bars with the image plane (highlighted in red). B: An oblique view in the plane of one of the Z-bars. The position of the Z vertices are calculated by extending least squares fits to the straight sections. C: 3D illustration of the phantom highlighting the Z-bar pattern and the relative positions of the registration divots.

The phantom was imaged using both the CT and MRI scanners. In the case of the CT, the slice thickness was 1.5mm, with an inter-slice spacing of 1mm. In the image plane, the pixel size was 0.39mm. For MRI, a T1-weighted gradient echo sequence, with TR=14ms, TE=6ms, Flip angle=23 degrees, Averages=5 was employed to obtain a 1mm³ voxel data set of the phantom.

Characterization

The nature of the phantom construction process, including movement of the strands while pouring PVA-C around them and the expansion of the material during the freeze process, prevented us from knowing in advance the exact locations of the Z-bars within the phantom with respect to the milled fiducials. Thus, it was necessary to use the volumetric CT data to characterize the coordinate space of the phantom. The image data were loaded into the IGNS system, and the annotation tool was used to manually drop a series of markers along each segment of the Z-bars. The coordinates for these points were used to determine a linear least squares fit for each segment. A bisection algorithm was subsequently used to determine the intersection (or closest point to it) of the segments

which were used as the Z-bar vertices. These vertices were used as the locations of the Z-bars in the phantom's frame of reference.

Impressions

While the smaller Z-bars provided the opportunity to perform calibrations with smaller MIDs as intended, and the solid PVA-C phantom was much easier to handle, the overall usefulness of the phantom was limited for the following reasons.

When imaging the phantom at different maximum imaging depth settings, it was necessary to alter the distance from the US transducer to the Z-bar fiducials. In order to achieve this, it was necessary to have a thin layer of water on the surface of the phantom to provide acoustic coupling without allowing the US transducer actually put weight on the PVA-C itself.

The lack of rigidity of the PVA-C strands made it difficult to keep them exactly in position during the construction process. This resulted in slightly imperfect Z-bars in that they contained geometric distortions (Figure 3-16B), limiting their accuracy.

Finally, the image quality of the diagonal segments of the vertical Z-bars were still sub-optimal. The smooth texture of the strands and the angular incidence between the diagonal of the Z-bar and the US beam caused a diminished return signal due to angular reflection.

3.5.1.4. Calibration Phantom Version 3

In the two previous approaches, the goal was to obtain a single image that would provide enough information to estimate h_pT , the transformation from US image space to the probe holder space. In order to improve the quality of the calibrations, the procedure

was altered to allow for multiple images and thus many more fiducial points to be acquired and used in the calibration. This removed the necessity to have multiple Z-bar markers within the phantom.

The final version of the calibration phantom was a simplified version of the previous two. The phantom differed from the previous ones in that it employed a single horizontal Z-bar fiducial marker. It was similar to the first phantom in that it returned to the use of hollow tubes immersed in a water bath to form the Z-bar instead of PVA-C. The thickness of the tube walls were decreased and the overall diameter was increased to improve image visibility in US.

3.5.1.5. Construction Description

Two support plates were milled from Plexiglas according to Figure 3-17 and fixed parallel to each other 3cm apart. Sections were cut from plastic drinking straws and their diameter measured with a caliper to ensure uniformity. The straw sections were inserted

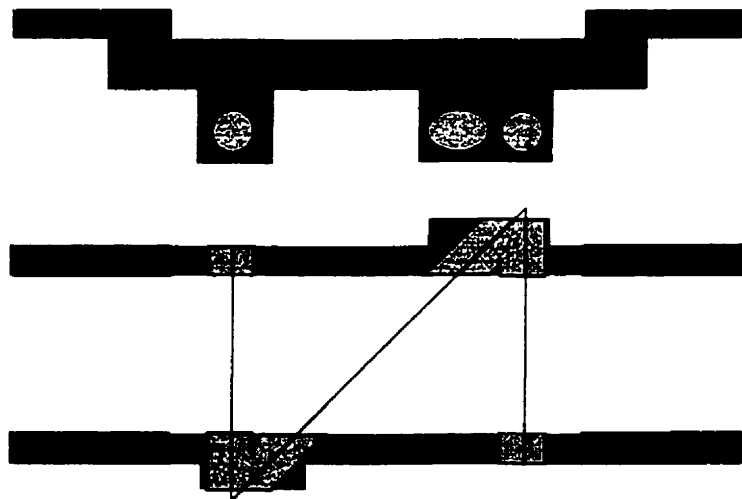


Figure 3-17: Schematic view of the single Z-bar calibration phantom.

into the guide holes, and sealed on the inside with silicone. The outside sections were left open for later filling with either water or imaging modality specific contrast agent. Electrical tape is used to seal the tubes when filled.

As with the first calibration phantom, the tubes were filled with Iothalamate melglumine, U.S.P./ 60% to provide contrast when imaged in CT. The divot holes were also filled with the contrast agent and covered with waterproof tape. The assembly was placed in a water bath for imaging. CT images of the phantom were acquired using the same slice thickness parameters as with the first phantom, namely a slice thickness of 1.5mm, and inter-slice spacing of 1mm, however the smaller size of this phantom allowed an in plane pixel size of 0.23mm. Unlike the previous phantoms, the CT data set was not required to characterize the phantom, but was needed as a simulated pre-operative data set to measure the IGNS system accuracy.

Figure 3-18A shows a typical US image of the phantom. The large diameter thin walled tubing allowed for a significantly improved visualization of the Z-bar. Figure 3-18 B shows one of the CT images, demonstrating good contrast of the Z-bar with respect to the surrounding water. The intensity contrast did cause some minor streaking artifact.

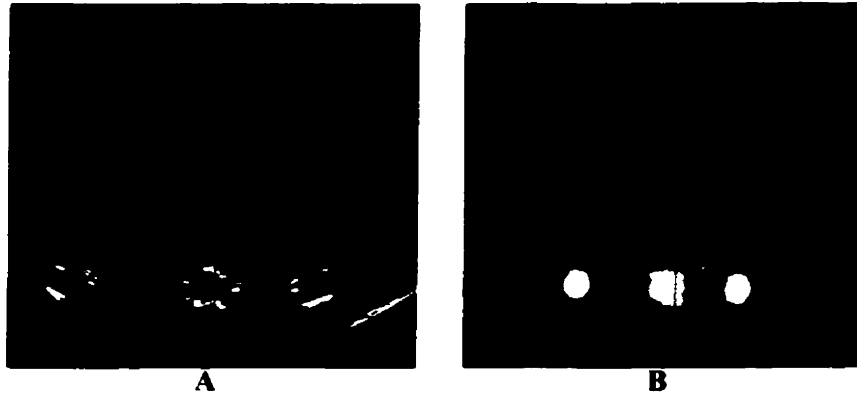


Figure 3-18: A: US image of the Z-bar fiducial clearly showing the walls of the tubes. B: CT image of the phantom. The tubes were filled with contrast agent, and thus appear to be full.

3.5.2. Deformable Phantom

Although many authors have reported on their experience with intraoperative US based IGNS, the literature presents little on the validation of such systems, particularly in their ability to detect tissue deformation. Some authors have presented static phantoms that consisted of an olive suspended in solution or a series of beads along a thread to characterize the static accuracy, or demonstrated their systems on canine brains. This section describes the construction of a novel deformable phantom capable of being imaged in US as well as MRI. It contains simulated hemispheres, ventricles and blood vessels. The design allows us to deform and image the phantom, enabling us to evaluate the ability of our IGNS system to detect and correct for this deformation. Figure 3-19 shows the deformable phantom in its water-bath container.

The phantom consists of three parts: the actual brain simulating PVA-C disk, a support collar and water bath. The disk sits in the support collar, which is in turn supported by screws protruding through the water bath container. The phantom may be

deformed by selectively tightening or loosening the support screws, which apply pressure on the collar and thus the brain disk.



Figure 3-19: Image of the deformable phantom held in the support collar in a water bath.

3.5.2.1. Construction Description

PVA-C Brain Disk

The disc consists of two PVA-C hemisphere sections surrounded by additional PVA-C to form the disc. The two hemisphere molds were constructed to have ridged outer edges to simulate cortical surfaces, and fluid compartments to simulate blood vessels and ventricles. Figure 3-20 illustrates the construction of the hemisphere molds. These molds were built by cutting out hemisphere-like shapes from 10cm thick blocks of Plexiglas. To make the fluid filled compartments, ventricle objects were constructed from Plexiglas cylinders and placed inside the molds. Simulated blood vessels were created by placing long narrow rods vertically inside the mold. The hemispheres were filled with

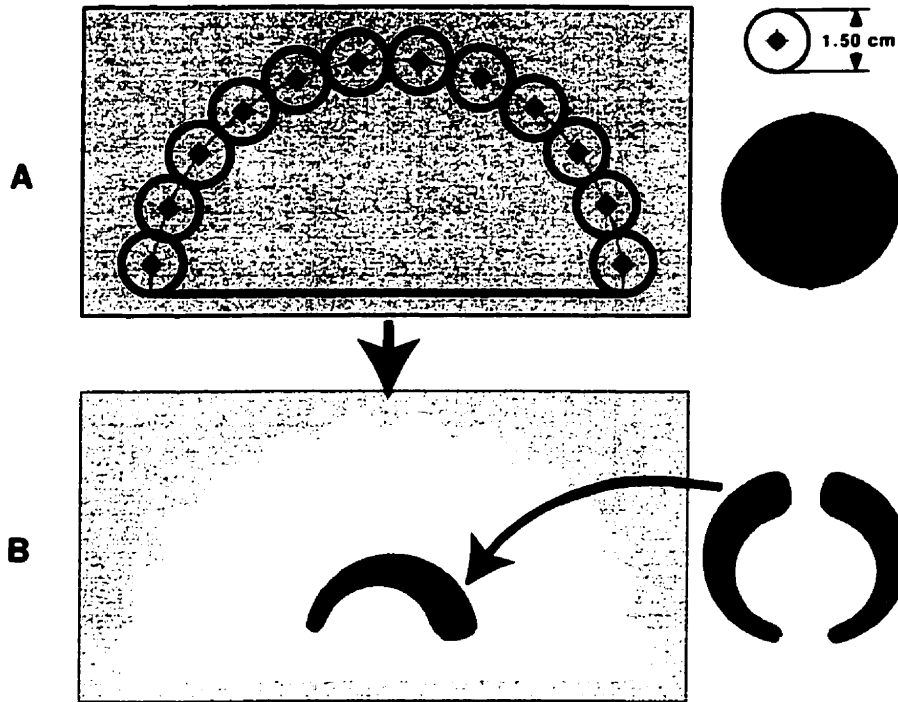


Figure 3-20: Schematic of the construction of the simulated brain hemisphere. A: Red circles indicate points to drill into a 10cm thick slab of Plexiglas. The red line indicates a cut line. The circle on the right is a face view of a Plexiglas rod that was drilled and cut in half to form ventricle molds. B: Schematic view of the final mold.

PVA-C (10%PVA-C/vol) and subjected to a single freeze/thaw cycle. They were removed from the mold and placed symmetrically in a larger cylindrical mold. The gaps between the hemispheres and the cylinder wall were filled with more PVA-C (15%/vol) and subjected to another freeze/thaw cycle. The simulated blood vessels and ventricles were left void of PVA-C so that they would fill with water when placed in the water bath. The final disk was removed from the mold and stored in a distilled water bath.

Support Collar and Water Bath

Figure 3-21 shows the design of the support collar and water bath. The support collar consists of a hollow section of Plexiglas tubing with an inner diameter and thickness of equal to that of the PVA-C disc. A 45° wedge was cut out of it to create a

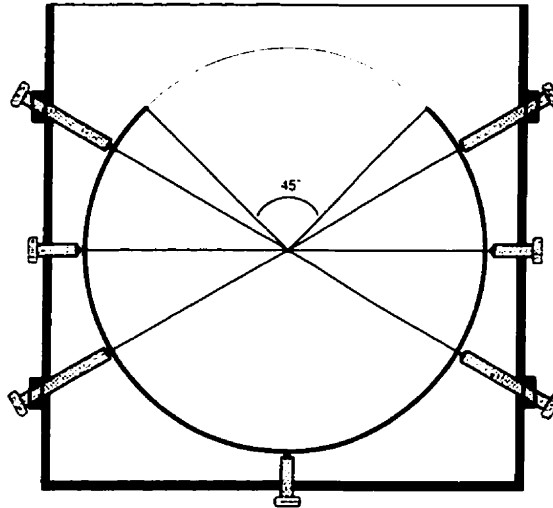


Figure 3-21: Schematic of the support collar, screws and water bath container.

window for US imaging and to allow room for the collar to contract when compressed. The water bath container comprises of a Plexiglas box with a removable lid, with reinforcements at the locations where the screws protrude into the box. The screws are made of nylon for MRI compatibility, and are covered in Teflon tape prior to use to ensure a water-tight seal.

Imaging

The phantom was placed inside the container which was then filled with distilled water. The phantom was placed in an MRI imaging scanner (Philips Gyroscan ACS II, Philips, Best, The Netherlands). As with the second version of the calibration phantom, the deformation phantom was imaged with T1-weighted gradient echo sequence, (TR=14ms, TE=6ms, Flip angle=23 degrees, Averages=5) which yielded a 1mm³ voxel volumetric data set. The images were transferred to an Allegro visualization workstation (ISG Technologies, Mississauga, ON) where threshold and manual segmentation tools were employed to obtain a volume rendered version of the phantom. Figure 3-22 shows the volume rendered image of the brain disk obtained from the Allegro workstation. The

hemispheres, as well as the fluid filled ventricles and blood vessels, can easily be identified.



Figure 3-22: Volume rendered view of the segmented brain disk. The yellow sections are the hemispheres with the cortical surface, the red strips are the simulated blood vessels while the green sections are the ventricles.

3.5.3. Resolution and Distortion Phantom

The phantom used for measuring resolution and geometric distortion consisted of thin threads in a pattern held between two parallel drilled Plexiglas plates acting as a template (Figure 3-23). The template defined 7 parallel rows and columns each 10.0mm apart. The upper rows contained fewer threads at the edges corresponding to the angular field-of-view of a typical US fan beam.

The two plates were sufficiently far apart to ensure that when imaged, the plates would not intersect the beam. The threads were thin enough ($\approx 100\mu\text{m}$) to ensure that they were smaller than the US pixel size. The plates were immersed in a 5% glycerin solution to provide low scatter, and to provide a medium where the speed of sound is close to that of brain (1510m/s).

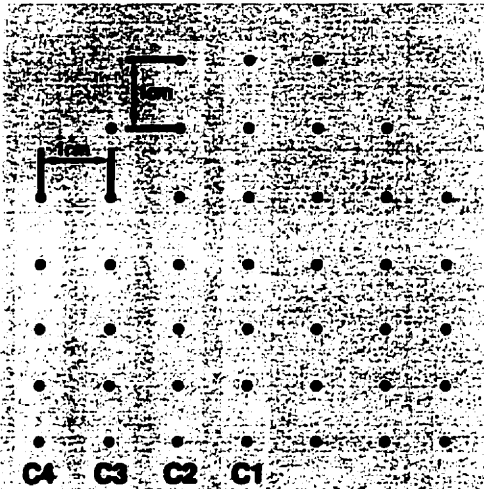


Figure 3-23: Illustration of the placement of the thin threads in the geometric distortion phantom. This arrangement allowed for multiple profiles to be obtained at different locations in the image simultaneously.

3.5.4. Slice Thickness Phantom

The slice thickness phantom consisted of a thin sheet of fine sandpaper bonded to a sheet of Plexiglas. The sheet was placed in a holder such that the plane of the sandpaper was at a 45° angle in the plane of the US beam (Figure 3-24). Thus, the height of any profile of the edge as seen in the US image yields the slice thickness at that point.

3.6. Discussion

This chapter described the tools developed as part of our intraoperative US based IGNS system, including relevant software as well as calibration tools and phantoms required to calibrate and validate the system.

The software provides the surgeon with simple yet informative tools to appreciate any movement of relevant brain tissue and pathology. First, live US images may be acquired and displayed in real time along with the co-planar pre-operative MR images. Interactive tools including the ROI overlay and the marker/line delineation tools allow

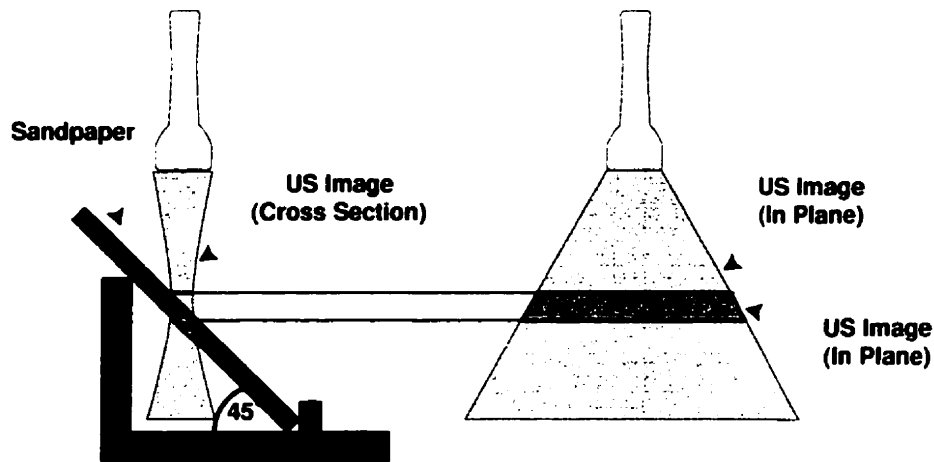


Figure 3-24: Illustration of the slice thickness phantom and its basic principle. Because the target plane intersects the imaging plane with a 45° angle, the height equals its width

the surgeon to compare and quantify the pre- and intraoperative images in more detail. The image warping tools provide the ability to estimate the deformation over the entire image and to correct the pre-operative images. Finally, the modular nature of the software will allow for improvements in the methodology to be easily added to the IGNS system.

Several designs for calibration tools were built and evaluated, all employing Z-bar fiducial markers. The final tool employing a single Z-bar simplified image acquisition while minimizing the contribution of image partial volume effects on calibration accuracy. The calibration tool had a second use as an accuracy verification tool. A volumetric CT scan of the tool simulating a pre-operative data set was obtained. Using the data set with the IGNS system can yield a series of co-planar US and CT images of the fiducial marker. The position of the fiducial marker in both images can be determined in the common tool frame of reference. The distance between the homologous points can be used as a measure of the system's accuracy.

The multi-modality deformation phantom consists of a PVA-C disk held in a water bath by a support collar and screws. The phantom includes simulated anatomical

structures such as lateral ventricles, blood vessels, mid-line and a cortical surface. The PVA-C allows us to obtain images in both US and MR, and to simulate tissue deformation by compressing using the support screws. This provides a tool to test the IGNS system's ability to display, measure and correct for tissue movement.

Chapter 4

System Characterization

4.1. Introduction

As described in the previous chapter, the intraoperative US based IGNS system consists of an ultrasound imaging device, a computer with a frame grabber, and a 3D tracking device. This chapter presents experiments performed and results obtained to characterize this system. First, the US imaging/computer frame-grabber system is characterized, including axial and lateral resolution, US image slice thickness and image spatial distortion. Second, the precision of the tracking device is examined, followed by an examination of the precision of the procedure employed to obtain h_pT , the calibration relating the US image to tracking device. Finally, the overall accuracy of the IGNS system is measured using the calibration phantom described in section 3.5.1.4.

4.2. Ultrasound/Frame Grabber System Characterization

4.2.1. Materials and Methods

Whenever possible, the procedures carried out for US system characterization followed the guidelines set out by the American Association of Physicists (AAPM) quality assurance protocols.¹¹³ The guidelines present two methods of measuring resolution: using a dedicated resolution phantom, or a thin wire target phantom. The resolution phantom presents a series of objects consisting of targets of various sizes, at

varying distances from one another. The investigator must select the smallest spacing that allows two adjacent targets to be resolved. The thin wire target phantom essentially provides an impulse function input into the imaging system. Measuring the profile of the response in the image yields a quantitative and less subjective measure of imaging resolution, and is employed here. The parameter used to describe the resolution is the full width at half maximum (FWHM) of the profile of the thin wire target.

All measurements were performed at several US MID values. As described in the previous chapter, the maximum imaging depth represents the distance from the transducer face to the most distal tissue displayed at the bottom of the screen, and is roughly analogous to the field of view of a CT or MR image. The US system scales the image to fill the screen based on the MID setting. Thus objects in images acquired with a lower MID will appear larger than in images acquired with a greater MID. Figure 4-1 shows two US images of the thin wire target phantom (described in section 3.5.3) taken at MID values of 5 and 9cm. Note the different scale bars on the right of each image.

4.2.1.1. Axial and Lateral Resolution Measurements

Image acquisition

The thin wire target phantom was filled with a 5% glycerin (by vol) to approximate the speed of sound in brain (1510m/sec). The NTSC video output of the US machine was connected to the frame grabber of the IGNS workstation. The US system was set to a 5cm MID. The US transducer was placed such that its face was submerged in the phantom bath to ensure good acoustic coupling and to allow as many of the wires as possible to be visible. The US brightness and contrast parameters were set such that all the wires were clearly resolvable. Once in position, ten images were acquired and stored. For each image, the transducer was moved slightly in the direction parallel to the wires to

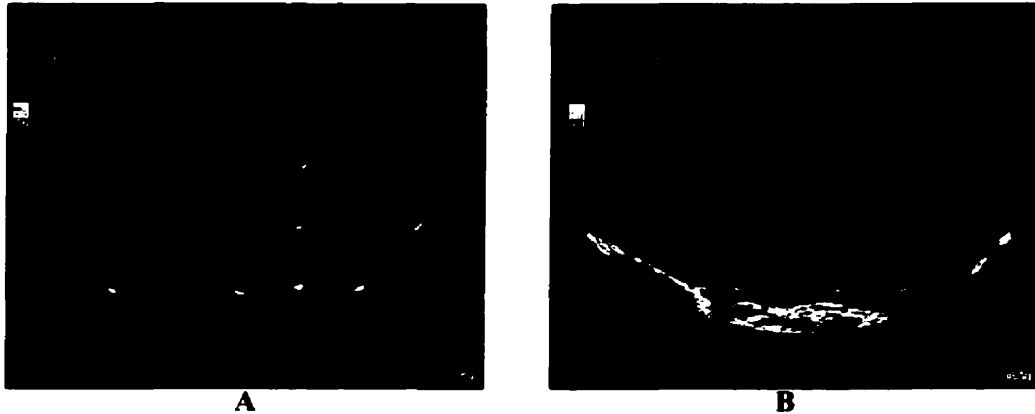


Figure 4-1: Images of a geometric distortion phantom taken at two MID settings. A: MID=5cm. B: MID=9cm.

ensure that if there were any undetected bubbles or imperfections in any of the wires, they would be present in only one or two images

This process was repeated with the MID set to 6 and 7cm respectively. In each case, between ten and twelve images were acquired in order to allow for rejection of images where excessive noise may have obscured one or more of the wires.

Image Analysis

The ten captured images at 5cm MID were loaded into the analysis module of the IGNS software. In each image, vertical and horizontal profiles were drawn through each dot (from a wire) and the pixel values corresponding to the profiles were extracted. To improve the signal to noise of the measurements, the individual profiles from each image corresponding to a particular target wire were averaged. The averaging was accomplished by aligning and re-sampling the profiles to a common grid, according to the following procedure.

- Find the peak of each profile

- Determine the left and right tails of each profile by finding the first pixels on either side of the peak that falls below 15% of the height of the peak
- Calculate the mean value, or centroid of the trimmed profile
- Linearly interpolate profile values at each common grid point to resample it to the uniform grid whose center is the centroid of the peak
- Average all re-sampled profiles corresponding to the same target wire
- Obtain FWHM by calculating σ ($FWHM=2.3\sigma$) for the average profile

Figure 4-2 illustrates the procedure of averaging the profiles to obtain a value of the FWHM. Each average profile consisted of 8 to 12 individual samples. The actual number used varied with the visibility of each individual sample. If an image artifact distorted an individual profile, the profile was discarded.

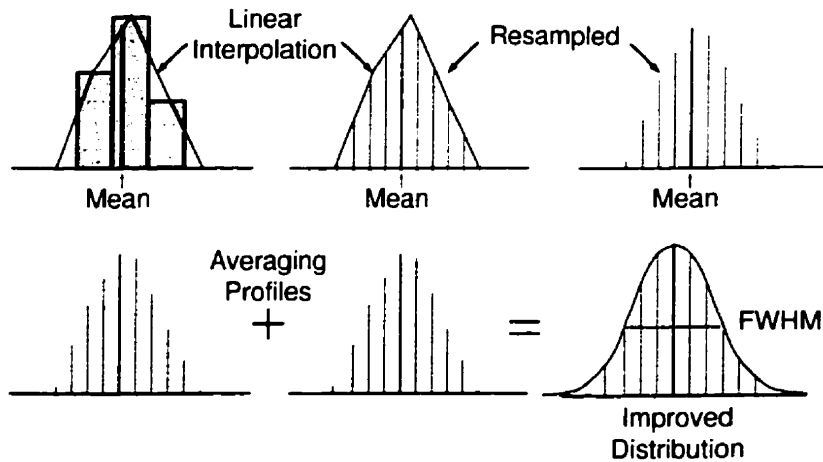


Figure 4-2: Illustration of the procedure followed to resample and average profiles of the same point from several images. The average profile provided an improved Gaussian distribution.

FWHM values were obtained for each point visualized on the image. The scale bar visible on each image was used to determine the conversion factor from pixels to mm. The US scanner assumes the speed of sound to be that of average tissue (1540 m/sec), however, because the phantom material (glycerol in solution) mimicked brain tissue (1510 m/sec), an additional correction of v/v_s , the ratio of the speed of sound for tissue and that of brain was applied. These FWHM values were sorted by column (horizontal distance from centerline) in the phantom and plotted as a function of depth. This procedure was repeated for the images obtained using MID values of 6 and 7cm.

4.2.1.2. Geometric Distortion Measurement

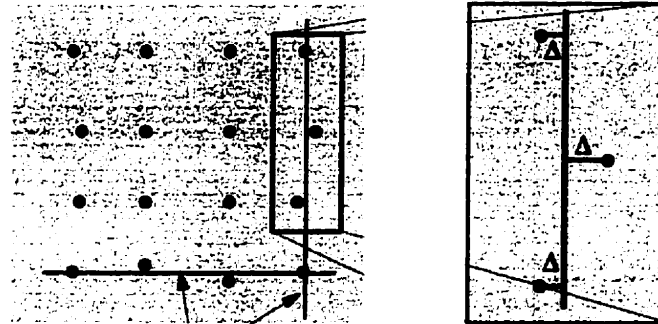
The images obtained to determine the system resolution were also employed to evaluate the system distortion. An image from the 5cm MID group for which all the dots were visible was selected. The center of each dot in the image was identified and its location, in image coordinates, tabulated. These points were sorted into individual rows and columns.

A least squares minimization method (LINEST function, Microsoft Excel) was used to obtain a linear best fit line through each row and column. For each line, the distance from the measured points and the fit line was obtained and tabulated. Figure 4-3 illustrates the method of measuring Δ , the distance from the actual wire image point, and the closest point on the best-fit line.

4.2.1.3. Slice Thickness Measurement

The slice thickness phantom was submerged in the 5% glycerin solution, and the US machine was set to a MID of 5cm. The transducer was positioned such that the imaging plane intersected the wedge at a 45° angle as illustrated in Figure 3-24. The vertical position of the US was set so that the target profile was visualized at a depth of

4.5cm, as measured using the depth scale on the image. This was the maximum depth where the entire profile was visible. Figure 4-4 shows two examples of US images of the phantom demonstrating the slice thickness profiles. Five images were acquired and stored by the IGNS system.



Linear best fit line Δ =distance from point to line

Figure 4-3: Illustration of how geometric distortion is measured. Each row and column is used to calculate a linear best fit. The distance from each point and the line (Δ) quantify the distortion.

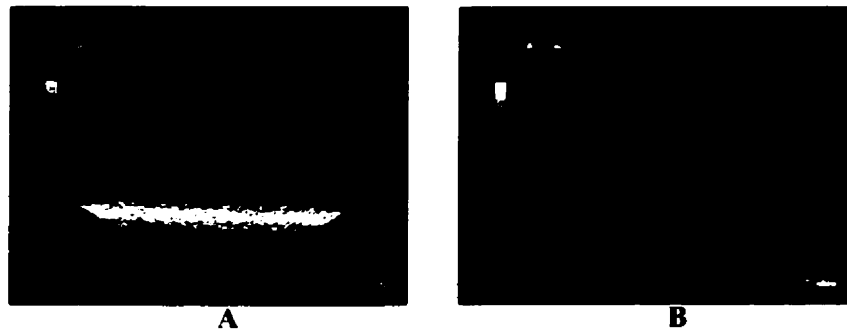


Figure 4-4: Ultrasound images of the slice thickness phantom taken at a maximum imaging depth of 5cm. A: Profile depth of 4.5cm. B: Profile depth of 1.5cm.

The transducer was moved vertically so that the target profile was at a depth of 3.5cm, and five more images were acquired. Similarly, five images were acquired at each of target profile depths of 2.5 and 1.5cm respectively. The US machine MID was set to 6cm, and another set of images was acquired in the same manner as before, except that

the target profile depths ranged from 5.5cm to 1.5cm at 1cm intervals. Finally, the MID was set to 7cm, and a set of profiles was acquired at depths ranging from 6 to 2cm, again at 1cm intervals.

A Gaussian blur of radius 1 pixel was applied to all the US images to reduce the noise of the images. This allowed the automatic profile averaging technique described in section 4.2.1.1 to function reliably, as it occasionally confused noise for a profile tail. Figure 4-5 shows how smoothing the image yielded smoothed profiles.

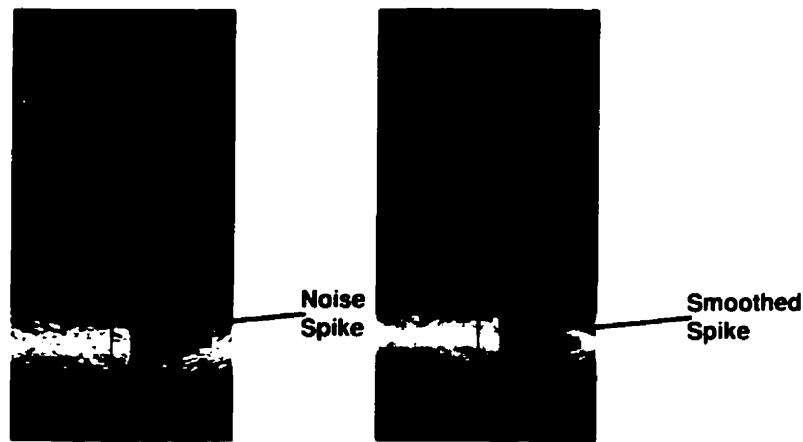


Figure 4-5: Example of image smoothing to improve the reliability of the semi-automatic profile averaging technique. The negative spike may cause the profile trimming procedure to clip significant data. The profile of the smoothed image does not contain the spike. A similar result would have been accomplished by smoothing the profile itself.

Three regions of interest (ROI) were identified in each image as illustrated in Figure 4-6. Two vertical profiles (taken a few pixels apart) of the target were extracted for each ROI location for each image. Since five images were acquired in each set, ten profiles per sample were ultimately obtained for each location. The automatic procedure described earlier was employed to align and average the ten profile groups to single profiles, and the FWHM of each averaged profile was measured and noted. Because the profiles were not observed to be consistently Gaussian, the FWHM was measured by

determining the location where the profile crossed the half maximum at the rise and fall of the curve. The FWHM values obtained were grouped by MID and plotted as a function of depth for each ROI location (C1, C2, C3) for each image.



Figure 4-6: US image of the slice thickness phantom demonstrating the locations of the profile samples for column 1, 2 and 3.

4.2.2. Results

4.2.2.1. Axial and Lateral Resolution

Figure 4-7 shows the axial resolution vs. depth for the measurements at three MIDs acquired. Each graph plots the FWHM for all columns visible in each image. Figure 4-8 shows the lateral resolution for the same MID images and for the same columns. As one would expect, the axial resolution is higher (lower FWHM) than the lateral. Also, the lateral resolution exhibits more of a dependence on depth than the axial resolution, which should be independent of depth.

4.2.2.2. Geometric Distortion Measurement

Table 4-1 summarizes the results of the geometric distortion tests. The distance from any point to the best-fit line for all tests never exceeded 1mm.

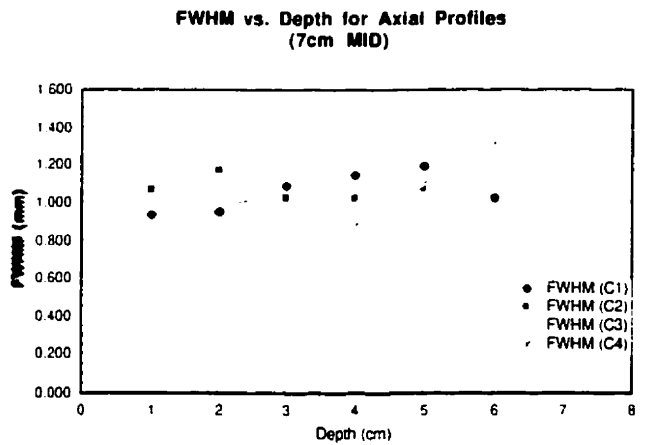
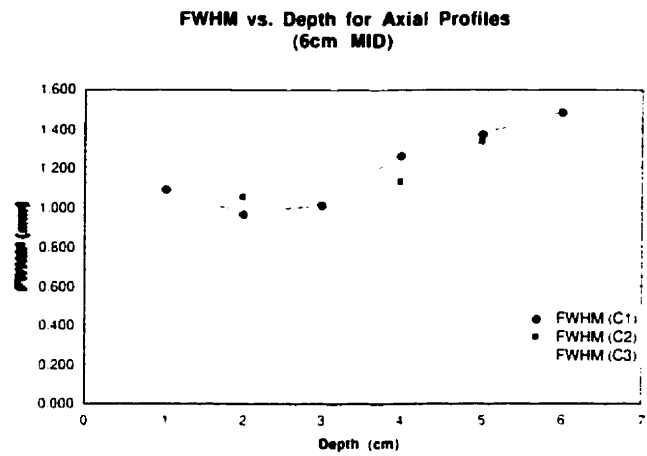
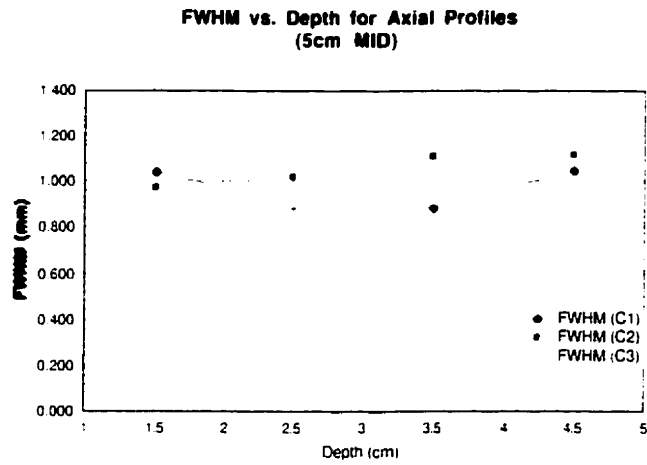
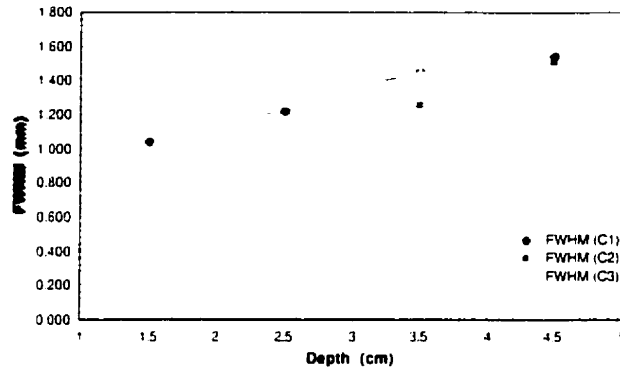
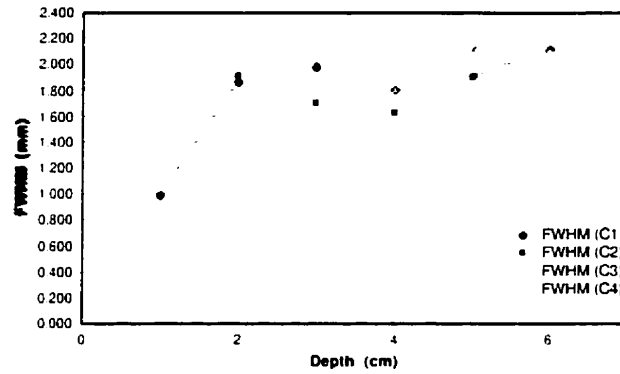


Figure 4-7: Axial resolution vs. depth measurements for US images acquired at maximum imaging depths 5, 6 and 7cm. The different lines correspond to different columns measured on the US image (see Figure 4-1).

**FWHM vs. Depth for Lateral Profiles
(5cm MID)**



**FWHM vs. Depth for Lateral Profiles
(6cm MID)**



**FWHM vs. Depth for Lateral Profiles
(7cm MID)**

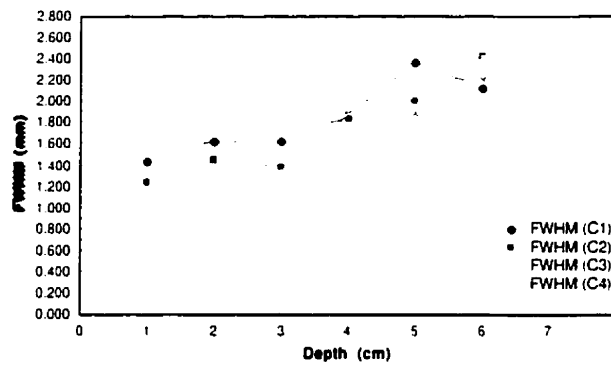


Figure 4-8: Lateral resolution vs. depth measurements for US images acquired at maximum imaging depths 5, 6 and 7cm. The different lines correspond to different columns measured on the US image (see Figure 4-1).

	Rows			Columns		
	Maximum Imaging Depth			Maximum Imaging Depth		
	5cm	6cm	7cm	5cm	6cm	7cm
Average (mm)	0.19	0.22	0.23	0.09	0.11	0.1
Max (mm)	0.42	0.57	0.64	0.23	0.37	0.32
Min (mm)	0	0.01	0.01	0.01	0	0

Table 4-1: Summary of geometric distortion measurements for both rows and columns for all maximum imaging depths.

4.2.2.3. Slice Thickness Measurements

Figure 4-9 presents the slice thickness as expressed by the FWHM for all measurements. As one would expect, the slice thickness (as measured by the FWHM) was considerably greater than either the lateral or axial resolution.

4.3. Tracker Precision

The tracking device plays a central role in every aspect of IGNS. It is used in every calibration step required by the IGNS system as well tracking the tools themselves. The accuracy of each step and of the overall system is thus limited by the accuracy of the tracker. Here we present an experiment performed to measure the precision of the tracking instrument.

4.3.1. Materials and Methods

A series of ten divot points 10mm apart were milled in a straight line into an aluminum bar. The holes were spaced 10 mm apart in a straight line. A pointer was attached to the tracker, and its calibration parameters (h_pT) loaded, enabling the location of the pointer's tip to be determined in tracker space. The pointer tip was placed in each divot, at which time the IGNS software was used to store the location of pointer tip in tracker space. The pointer was moved from one divot to the next in a back and forth

manner to acquire a continuous set of points such that the distance between any successive points would be 10mm. A total of 37 points were acquired, allowing 36 relative distance measures to be obtained. The distances between each point pair were calculated and tabulated.

4.3.2. Results

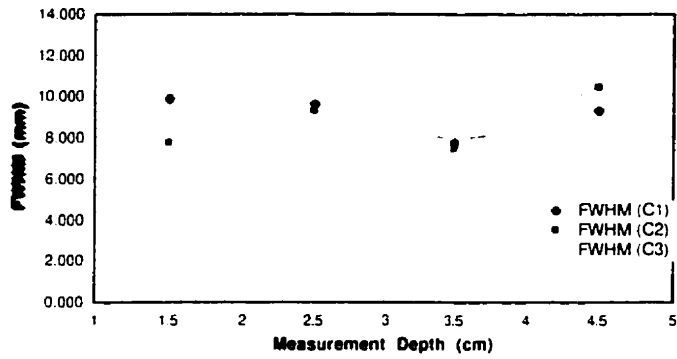
The mean value measured for the distance between each pair of points was found to be 10.0mm, with a standard deviation of 0.29mm. This is consistent with results reported previously in our laboratory.¹¹⁴ Using the 95% confidence level (1.96 standard deviations), we can say that the tracking device has an overall precision of ± 0.57 mm.

4.4. US-Based IGNS Calibration

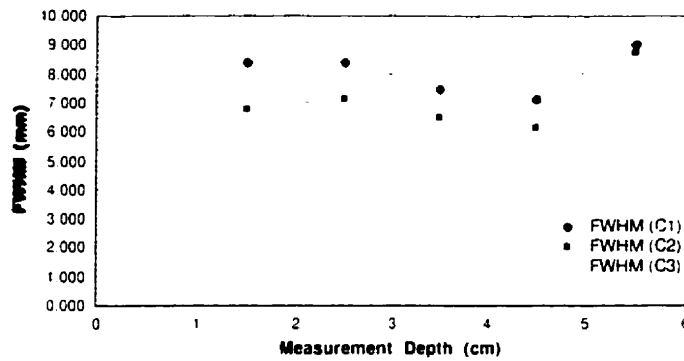
4.4.1. Introduction

As explained in section 2.5.2.2, a calibration procedure is required to determine h_pT , the transformation from the US image space to the tracked tool holder space. Because the “true” value of h_pT is not known, we can only determine the precision of our measurement. In order to measure this precision, multiple repetitions of the calibration procedure were performed ($n=10$) and the measurement variability compared. The values obtained were first tested to ensure that they were consistent with a normal distribution, and finally the translation component of the calibration results were tested for reproducibility by calculating their standard deviation.

US Slice Thickness (FWHM) for MID=5cm



US Slice Thickness (FWHM) for MID=6cm



US Slice Thickness (FWHM) for MID=7cm

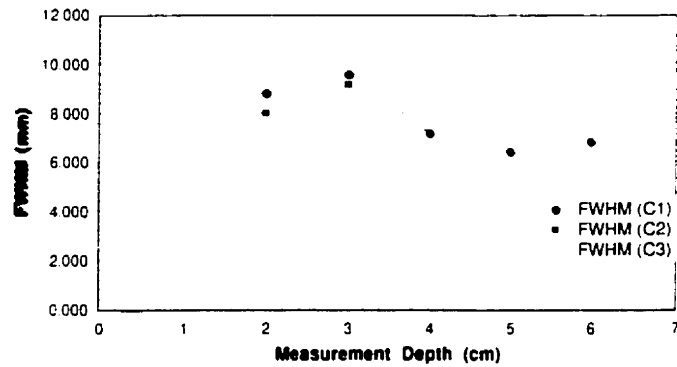


Figure 4-9: Slice thickness measurements expressed as FWHM of profiles takes from images at US MID values of 5, 6 and 7cm. The different lines correspond to different columns measured on the US image (see Figure 4-6).

4.4.2. Materials and Methods

The third generation US calibration phantom (see section 3.5.1.4) was immersed in a water bath of distilled water. The speed of sound of water at room temperature is 1498m/sec, which is sufficiently close to the accepted value of 1510m/sec for brain tissue,¹¹² so that no other correction fluid (e.g. glycerin) was added.

The US transducer was attached to the tracking device via the custom adapter to allow it to be tracked by the IGNS system during image acquisition. The NTSC output of the US machine was connected to the video input of the workstation frame grabber.

The US machine, set to a MID of 5cm, was used to visualize the Z-bar within the phantom. Eight images of the phantom were acquired in such a manner as to vary the location of the Z-bar from image to image. As the images were acquired into the IGNS software, the position and orientation of the tracked rigid body attached to the US transducer was acquired and tagged to the image. Thus, each image file contained the video grab of the US image, along with a 4x4 translation/rotation matrix.

Once acquired, the three markers representing the intersection of each segment of the Z-bar fiducial with the image plane were manually identified. This was performed using the line profiles along the 3 points as a visual aid (Figure 4-11A). With these, the position of the centre marker in the phantom space was calculated for each image. The tracked pointer was then used to identify the eight divot points milled into the phantom frame. These points were used along with their known locations in the phantom space to calculate the phantom-to-tracker transformation. Using this, along with the inverse of the transform from tool holder space to tracker space for each image, the coordinates of the central fiducial point for each image was transformed into the common tool holder space. This yielded a series of homologous points; one set in the tool holder space, and the other

in the US image space, which were used as the input to a least squares algorithm to determine the rigid body transformation from US image to tool holder space.

This procedure of acquiring images, registering the phantom to tracker space, and calculating the final calibration from US image to tracker space was performed ten times. The results were tabulated, and the translation component of the rigid body transformations extracted and compared. These were examined to verify that the samples were consistent with a normal distribution, and the standard deviation of the x, y and z components of the translation were calculated. For reference, the x and z directions correspond to the US image rows and columns respectively, while the y direction corresponds to the direction perpendicular to the US image plane.

The above calibration verification procedure was repeated for MID values of 7 and 9cm. The results are tabulated below along with the results from the 5cm MID experiment.

4.4.3. Results

The standard deviation is an appropriate measure of precision if the measured data form a normal distribution. Since it is being used to evaluate the repeatability of the calibration, it was necessary to ensure that the observed values do correspond to a normal distribution. Figure 4-10 shows a typical probability plot, where the measured values are plotted against their corresponding percentile values. The points lie along a 45° line, which is consistent with a normal distribution. Similar plots were performed for the Y and Z directions, as well as for the data obtained for MID depths of 7 and 9cm. Only the first one shown for brevity.

**Probability Plot of X Translation
for MID=5cm**

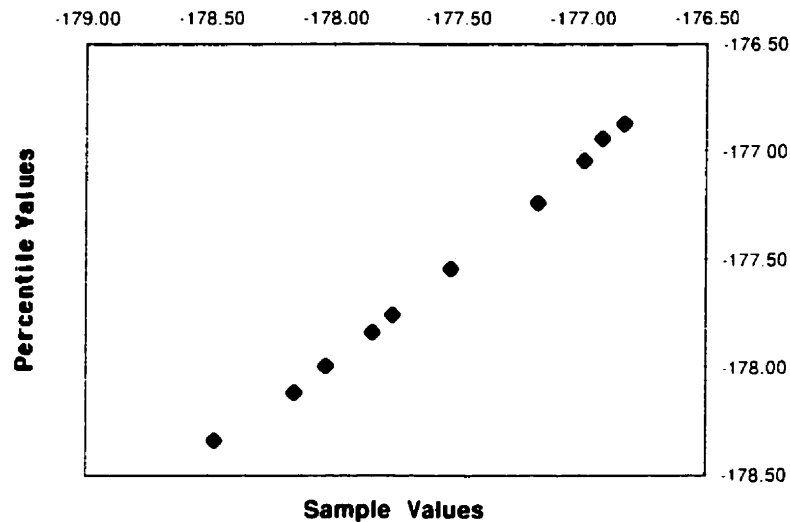


Figure 4-10: Probability plot of the sampled values of the X-translations obtained by repeated calibration trials for MID=5cm. The straight line at 45° is consistent with a normal distribution.

Table 4-2 summarizes the results of the reproducibility trials for the US→tracker calibration. Using the 95% confidence interval, the reproducibility of the calibration procedure is poorest in the Y direction, at $\pm 2.6\text{mm}$. As one would expect from the US

Reproducibility of Translations Obtained from US image→Tracker Calibration (n=10)				
MID		X	Y	Z
5 cm	Mean	-177.57	-37.67	-0.09
	Stdev	0.58	1.17	0.68
7 cm	Mean	-176.61	-35.74	0.28
	Stdev	0.34	0.85	0.35
9 cm	Mean	-176.42	-35.4	0.87
	Stdev	0.41	1.3	0.53

Table 4-2: Reproducibility of the x, y and z translation components of the US→Tracker calibration procedure for MID=5, 7 & 9cm. Mean is the mean value of the translation while the standard deviation is the standard deviation of the component for the 10 trials.

image slice thickness results, the Y direction corresponds to the direction perpendicular to the US image. In the image plane, the calibration repeatability is on the order of $\pm 1.4\text{mm}$.

4.5. Overall System Accuracy

4.5.1. Introduction

The most important measure of the US based IGNS system is its accuracy in mapping features in the US image to homologous features in the pre-operative image space. All the characterization components presented thus far contribute to the overall accuracy measured here. In order to be able to measure the accuracy, one must be able to define a common coordinate space between the "pre-operative" and "intraoperative" image spaces. This is provided by the calibration phantom as demonstrated in the previous section. A volumetric scan of the phantom serves as the "pre-operative" data set, and while US images are acquired, the co-planar images of the volumetric scan are obtained simultaneously. By identifying the fiducial points on both images, the phantom space coordinates of the homologous centre markers can be calculated and compared. The relative distance between these homologous points serves as a measure of the overall accuracy of the system.

4.5.2. Materials and Methods

The hollow Z bar of the calibration phantom was filled with CT contrast used for angiographic imaging (Iothalamate melglumine, U.S.P./ 60%). Additional contrast agent was placed in the divot holes along the top of the phantom and sealed with tape. The phantom was placed in a water bath and CT images were obtained. The scan consisted of

35 slices, 1.5mm thick, with a slice spacing of 1mm. The in-plane pixel size was 0.234mm.

The image data were transferred to the IGNS workstation. The contrast agent in the Z-bar was replaced with distilled water, and the Z-bar itself was placed back in the water bath. The phantom was registered with the CT images by identifying the divot holes as seen on the CT images on the workstation and on the phantom itself using the pointer, and employing the registration algorithm described earlier.

Once a satisfactory registration had been obtained, the US transducer was used to obtain US images of the phantom. The US machine was set to a MID of 5cm, and the transducer was positioned to obtain a clear image of the Z-bar of the phantom. The IGNS software displayed both the US image and the co-planar CT image of the phantom. When a satisfactory image of the Z-bar had been visualized, both the US image and the co-planar CT images were stored. The transducer was moved slightly such that the Z-bar fiducial was visualized in a different portion of the US image. Again, the US/co-planar CT image pair were stored. This process was repeated until a series of 20 image pairs were acquired and stored. The image acquisition sequence was repeated for US MID values of 7 and 9cm. These images were also stored for later analysis.

The US and CT images of the phantom were reloaded in the IGNS software. The calibration tool was then used to position the markers indicating the locations of the intersection of the three segments of the Z-bar fiducial with the image plane, so that the coordinate of the center segment could be calculated in the phantom coordinate system. All the Z-bar segments for all the US and CT images were identified, and the corresponding center marker coordinates were determined and tabulated.

Figure 4-11 shows the US and co planar CT images of the phantom. To aid in proper fiducial identification, the image intensity profiles along the Z-bar line are displayed on the screen (not to scale). The walls of the segments were seen on the US image as peaks in the profiles. The positions of the markers were indicated on the profile, enabling accurate identification of each segment location at the center of the peaks.

Profiles along Z-bar fiducial



Figure 4-11: US image of the phantom with the segments identified with the calibration tool. The profiles at the top of the image serve as a visual aid in correctly identifying the center of the segment B: Co-planar CT image with the same segments identified.

The centre segment coordinates as determined from the US and homologous co-planar CT images were compared for the US MID values noted above.

4.5.3. Results

Table 4-3 presents the results of the accuracy study. The mean is the average distance from the US derived coordinate of the centre segment of the Z-bar to that of the same segment derived from the co-planar CT image.

Recalling that in a typical IGNS configuration, the mapping from patient space to image space has a typical accuracy of 2-4mm, the results shown here imply that the mapping from intraoperative US to the pre-operative image space can be accomplished with comparable accuracy.

Distance from US & Co-Planar CT targets in mm				
MID (cm)	Mean	Min	Max	Stdev
5	0.91	-0.42	1.98	0.75
7	0.83	-0.26	1.73	0.53
9	1.68	0.26	3.56	0.91

n=20

Table 4-3: Summary of the results of the IGNS system accuracy results.

4.6. Summary

This chapter was concerned with the characterization of the US based IGNS system, beginning with the imaging device/computer frame grabber system. The parameters measured were the resolution (FWHM of a line source), US slice thickness and geometric distortion. The axial resolution ranged from approximately 0.8-1.5mm while the lateral ranged from 1-2.6mm. The US slice thickness was found to range from 5-12mm.

The tracker precision was determined by calculating the standard deviation of measured distances between an array of divot holes at known distances from each other. The standard deviation was found to be 0.29mm, leading to a precision of ± 0.58 mm.

The precision of the measurement of h_pT , the transformation from the US image space to the tracked tool holder space was calculated by performing multiple measurements of h_pT , and determining the variability of the translation component of the

result. The calibration precision was measured to be $\pm 1.4\text{mm}$ in the image plane and $\pm 2.6\text{mm}$ in the direction perpendicular to the image.

Finally, the overall system accuracy was determined by employing the calibration tool and the volumetric CT to acquire co-planar US and CT images of the fiducial marker. Identification of the fiducial markers in both images yielded their positions in the calibration tool frame of reference, which were compared. The accuracy was measured to be $0.91\pm 1.5\text{mm}$ for $\text{MID}=5\text{cm}$, $0.83\pm 1.06\text{mm}$ for $\text{MID}=7\text{cm}$ and $1.68\pm 1.82\text{mm}$ for $\text{MID}=9\text{cm}$.

Chapter 5

Deformation Detection and Correction

5.1. Introduction

In the previous chapters the problem of tissue deformation, and its impact on IGNS was described. All the hardware and software that comprise our IGNS system and equipment required to calibrate and validate it were described as well. Further, the imaging system and tracking device were characterized to obtain an estimate of how well the IGNS can be expected to function. This chapter describes the ability of the IGNS system to demonstrate, quantify and to correct brain deformation. This is accomplished by simulating brain deformation using the deformable brain phantom described earlier.

A note about terminology

In the following sections, various data sets are described and compared. In order to avoid confusion, the following terms are used:

- **Non-deformed US (or simply US) images:** Refers to US images of the phantom in the non-deformed state.
- **Deformed US images:** Images of the phantom in the deformed state.
- **Non-deformed MRI:** MR images of the phantom in the non-deformed state.

- **Deformed MRI:** MR images of the phantom in the deformed state.
- **Warped (or corrected) MRI:** MR images of the non-deformed phantom that have been warped to match either the deformed US or deformed MR images of the phantom

We employed the deformable brain phantom described in section 3.5.2. For clarity, the experimental procedure will be described as two distinct experiments performed in succession. In actuality, the two were performed simultaneously interleaved in such a way as to enable the experiments to be performed with only two MRI scans of the phantom. This method of presentation in no way affects the results, but greatly simplifies the description.

In the first experiment, the image warping algorithm was tested by employing coplanar non-deformed and deformed MRI images of the phantom as simulated pre-and intraoperative images. This provided a baseline of how well we can expect the system to perform in the second part of the experiment, which consists of warping an initially non-deformed MRI to the deformed US image.

5.2. Non-deformed MRI vs. Deformed MRI

5.2.1. Set-up

A volumetric MR image data set of the phantom was acquired (T1-weighted gradient echo sequence, TR=14ms, TE=6ms, Flip angle=23 degrees, Averages=5) in the non-deformed state. The phantom was deformed by selectively tightening the support screws (movements ranged from approximately 0.5-1.5cm) as illustrated in Figure 5-1, and imaged a second time using the same protocol. Both image data sets were transferred to the IGNS system.

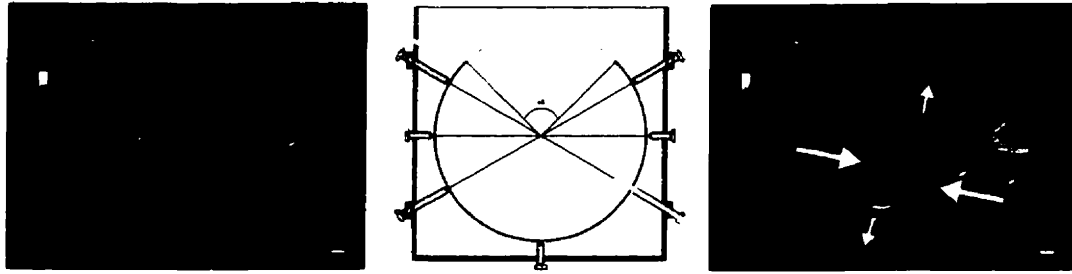


Figure 5-1: Illustration of the deformation applied to the phantom. A: US image of the phantom taken through the imaging window prior to deformation. B: Illustration of the directions of movement of the support screws to apply the deformation. C: US image after deformation. Arrows indicate the general direction of compression, expansion or movement of the structures.

A rigid body transformation between the two data sets was obtained by identifying homologous points in both images, and employing the same least squares fitting tool described earlier for registering the patient to the pre-operative image data. These were points that did not move with the deformation (e.g. the center of the screws as they entered the water bath), which are analogous to skull based points on a patient. Once registered, an arbitrary image orientation (roughly parallel to the face of the phantom) was selected in the non deformed MRI for viewing. The IGNS system allowed the two MRI data sets to be linked such that a co-planar MR image of the deformed phantom was obtained. Figure 5-2 shows the two co-planar MR images of the phantom, before and after deformation.

The point and spline based annotation tools were used to manually delineate homologous structures in both the non deformed and deformed MR images (Figure 5-3). The point structures consisted of the simulated blood vessels and the sulci. The spline curves followed the outlines of the simulated ventricles. The point annotations were used to characterize the deformation by measuring the distance between each homologous point, which ranged from 2.1 to 9.3mm.



Figure 5-2: Co-planar MRI images of the non-deformed and deformed phantoms.

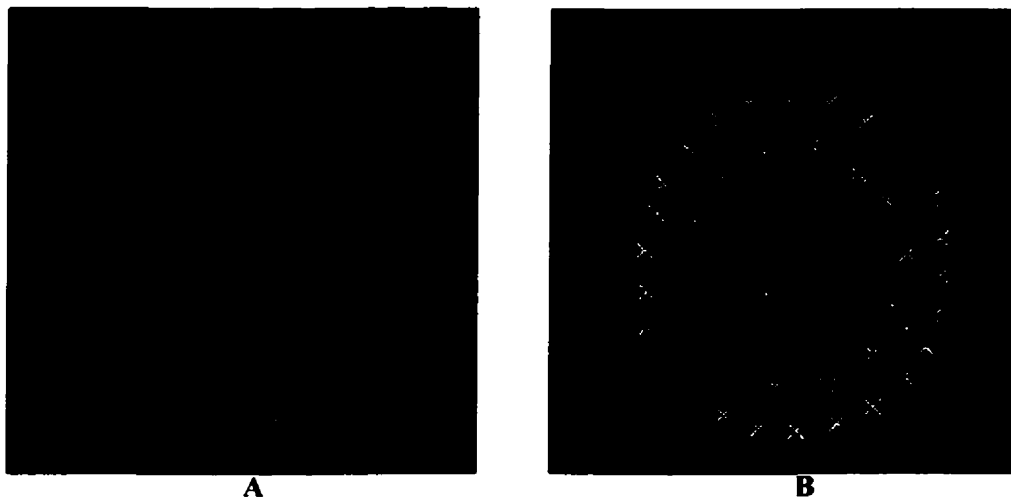


Figure 5-3: Homologous structures identified in both the non-deformed (A) and deformed (B) MRI.

5.2.2. Correcting deformation

The deformation grid tool described in section 3.3.5.8 was employed to define a 64x64 node linearly interpolated deformation grid. As input, the “filled region tool” was used to delineate the outline of the phantom, which served to define a boundary in which

grid nodes were flagged to be movable, while nodes outside the boundary were flagged as fixed. The homologous cortical and blood vessel points were chosen to generate a series of vectors representing the initial deformation condition. The homologous spline curves of the ventricles were selected and sampled parametrically to generate a further series of discrete points and thus end-points for additional initial deformation vectors. Figure 5-4 A shows the grid nodes (in red) flagged as movable after delineation using the “filled region” tool. The closest grid node to each initial displacement vector was determined, and that vector was applied to it, creating the initial condition. Figure 5-4B shows the grid after the initial displacement vectors were applied to the grid (blue lines).

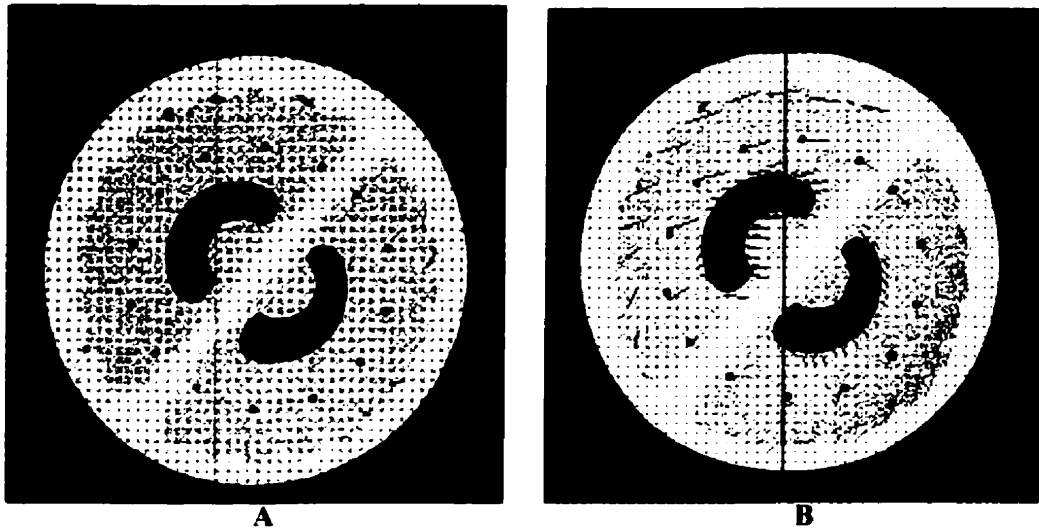


Figure 5-4: A: Displacement node grid superimposed on the non-deformed MRI of the deformable phantom. Small red crosses indicate nodes that are allowed to displace. B: Displacement grid after application of the initial displacement vectors obtained by identification of the simulated blood vessels, cortical landmarks and ventricles shown in Figure 5-3.

The initial displacements were allowed to propagate and relax according to the method outlined in section 3.3.5.8. The iterations were stopped when the maximum displacement of any grid node was below an arbitrary threshold of 0.05mm. The stopping criteria was reached in under 30 iterations. Figure 5-5 shows the results of the iterative

propagation/relaxation procedure. Figure 5-5A shows the displacement grid as vectors, yielding an overall appreciation of the direction of deformation, while Figure 5-5B shows the magnitude of the displacement as a color coded overlay.

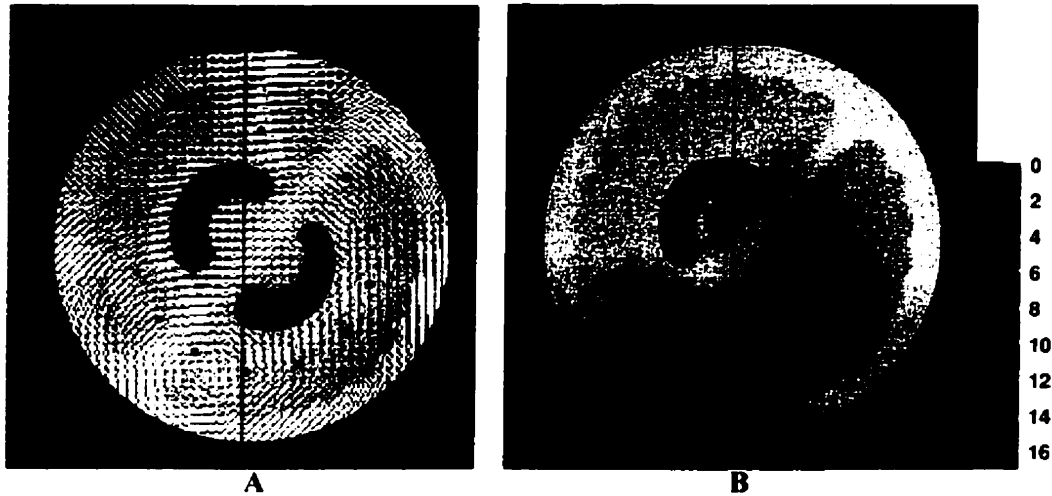


Figure 5-5: A: Vector grid obtained after allowing the initial grid of Figure 5-4A to propagate and relax to a steady state condition. The lines represent the direction of the grid node displacements and thus the measured deformation. B: Magnitude image of the displacement.

The displacement grid was applied to the non deformed MR image of the phantom using linear interpolation between grid nodes, yielding a warped version of the non deformed phantom. For qualitative comparison, Figure 5-6A again shows the MR image of the deformed phantom, while Figure 5-6B shows the warped MR image of the non deformed phantom. Visually comparing the pair with the images of Figure 5-2 shows that the correction has improved agreement between the non deformed and deformed MRIs.

5.2.3. Quantitative Assessment of Restoration Quality

To obtain a quantitative measure of the image restoration method, a rotating “leave one out” strategy was employed. A displacement grid was obtained as above,

except that one of the blood vessel points was deliberately left out as an initial point in the calculation. The same point was identified in the restored image, and its position was compared with that of its homologous point identified on the MR image of the deformed phantom. Ideally, the distance between the two should be 0 since a perfect restoration of the non-deformed MR image should overlay perfectly on the MR image of the deformed phantom. The distance between the actual deformed feature location and the warped MR feature was recorded for each pair of points.

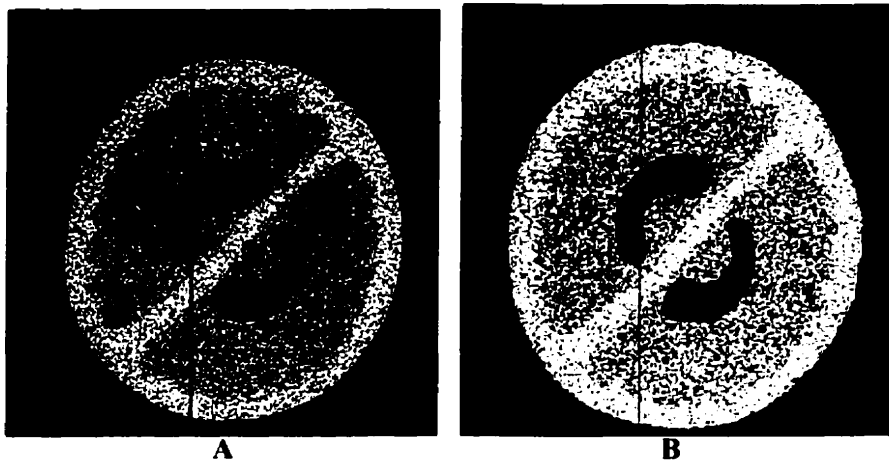


Figure 5-6: A MRI of the deformed phantom (as shown in Figure 5-2B). B: Warped image of the non-deformed MRI for comparison. The warped image contains more noise because it is a 1mm thick slice, while the MR image of the deformed phantom is 5mm thick to improve image quality.

This process of leaving a point out of the grid calculation and comparing the location of the feature on the deformed phantom MR image and the warped MR was repeated for all the blood vessel and cortical point features in the image pair. Table 5-1 presents the results. MR-dMR represents the distance in *mm* between the blood vessel landmarks identified in the non deformed and deformed MR, characterizing the deformation. dMR-Corr is the distance between the landmarks identified in the deformed MR and the warped MR, characterizing the error in the correction.

	MR-dMR	dMR-Corr
Mean	5.6	0.7
Max	9.3	1.1
Min	2.1	0.1
Stdev	2.1	0.3

Table 5-1: Summary of results of the non-deformed vs. deformed MR images of the phantom.

5.3. Non-deformed MRI vs. Deformed US

5.3.1. Imaging and Registration

The phantom was assembled and the tank filled with distilled water. The retaining screws were initially set such that there was no deformation. MR images were obtained (T1-weighted gradient echo sequence, TR=14ms, TE=6ms, Flip angle=23 degrees, Averages=5) and transferred to the IGNS system. The phantom was then fixed on a table, and registered with the MRI data using the IGNS probe. Once an acceptable registration was obtained, US and co-planar MR images were acquired, stored and visualized with the IGNS software.

The US and co-planar MR images were qualitatively compared using the interactive ROI tool to visualize the US superimposed on the MR images (Figure 5-7). Using the mouse, the ROI was moved over the area of the phantom visible to both the US and MRI. No significant discrepancies were noticed.

Following the qualitative evaluation, the annotation tools were used to identify homologous structures in both the US and MR images. The point annotation tool was used to drop markers over the simulated blood vessel points and the bottoms of the sulci when visible in both the MR and US images. The spline drawing tool was used to outline

the ventricles. Figure 5-8 shows the homologous structures used to quantify the registration quality.

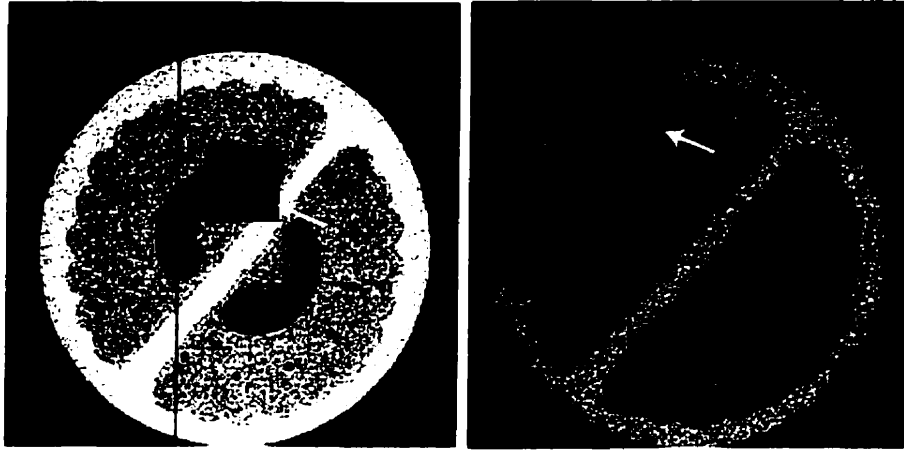


Figure 5-7: MRI images of the phantom after registration and before deformation. The ROI tool (arrows) is used to superimpose the US image onto the co-planar MRI to visually assess the registration by observing the degree of shift between homologous structures.

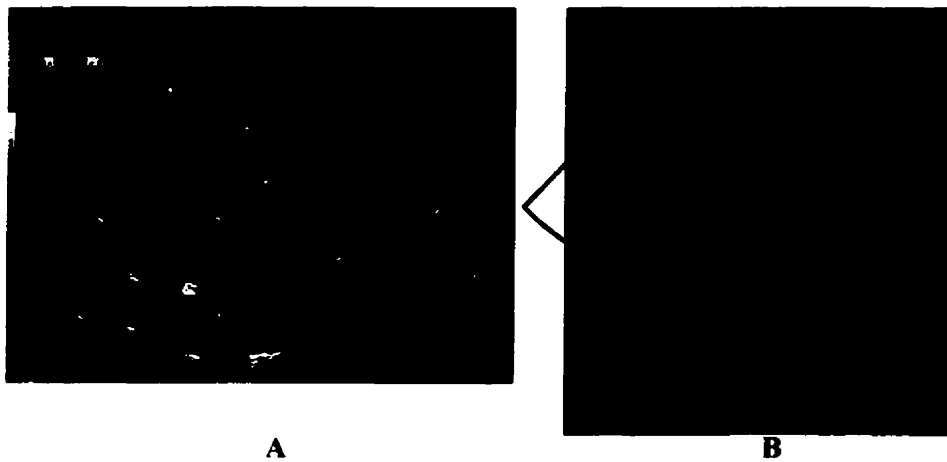


Figure 5-8: Registration accuracy assessment. A: US image of phantom with point and line annotation delineated from both the US and MRI image. B: Co-planar MR image of the phantom with the same annotations superimposed. Note the outline of the US image area in red.

The distances between homologous point annotations (blood vessels and cortical sulci) were compared. The maximum distance between homologous points was 4.5mm, which occurred at the periphery of the US image. The minimum distance was 0.1mm, with the average distance being 2.1mm. The point annotations and ventricle splines were used to create an interpolated grid (64x64 nodes) to estimate the registration error distribution over the image (Figure 5-9). The image shows that after excluding the periphery of the area of interest, the registration error ranges from approximately 0 to 3mm, which is typical in conventional IGNS.

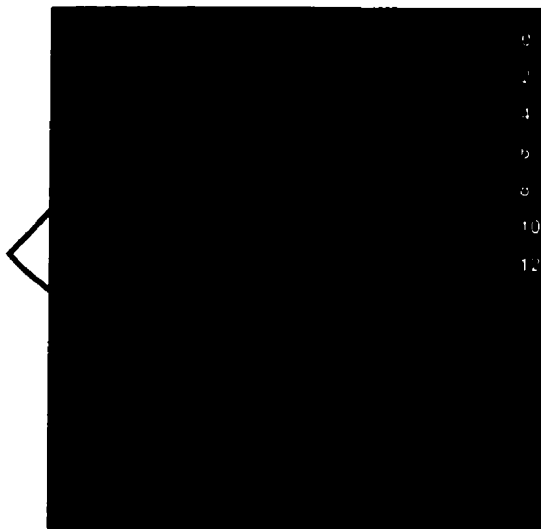


Figure 5-9: Displacement magnitude image showing the registration error distribution over the image area. The red triangle shows the US image boundary, and thus the area of interest.

5.3.2. Applying Deformation

Without moving the phantom holder, the PVA-C disc was deformed by tightening the retaining screws in a diagonal fashion, creating a deformation of the ventricles, and causing movement of the simulated cortical surface and blood vessels. Figure 5-1 illustrates the deformation applied to the phantom. The phantom was imaged again with the US system, and relevant frames stored for analysis.

One of the US images was recalled and compared to the co-planar MRI using the ROI tool. Figure 5-10 shows the post-deformation US image, the co-planar MR image, and enlarged images obtained by moving the interactive ROI over the simulated ventricle and blood vessels. By moving the ROI about the screen, an interactive appreciation of the deformation may be obtained.

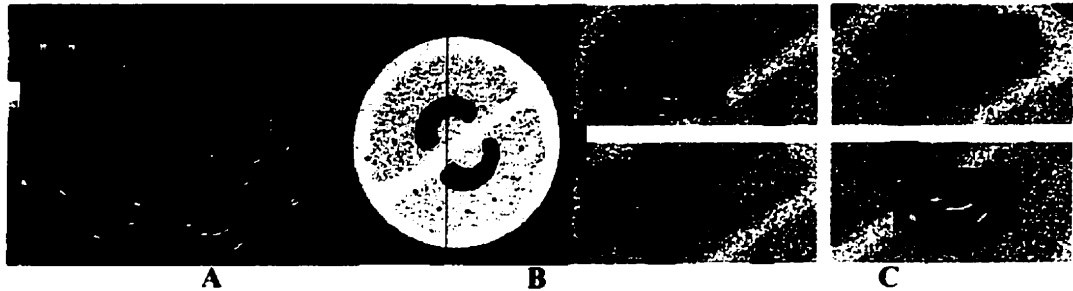


Figure 5-10: Visual assessment of phantom shift. A: US image of the phantom after deformation. B: Co-planar MRI of the phantom. Examining A and B clearly demonstrates a difference between the two. C: The ROI tool used to superimpose the US image on the MRI allowing more detailed visualization and comparison of the deformation.

As performed in the registration evaluation, annotation tools were used to identify the cortical sulci, the blood vessels and the ventricles. The deformation was assessed by measuring the distance from the homologous vessel and cortical points on the MR and US images. The movements of the identified structures (within the US field of view) ranged from 1.0 to 12.2 mm. Figure 5-11 shows the identified homologous points.

5.3.3. Deformation Correction

The same method described in section 5.2.2 was used to create a deformation grid and define a set of initial deformation vectors. The area of the phantom was identified on the MRI image using the area outline tool to define the area of the image where

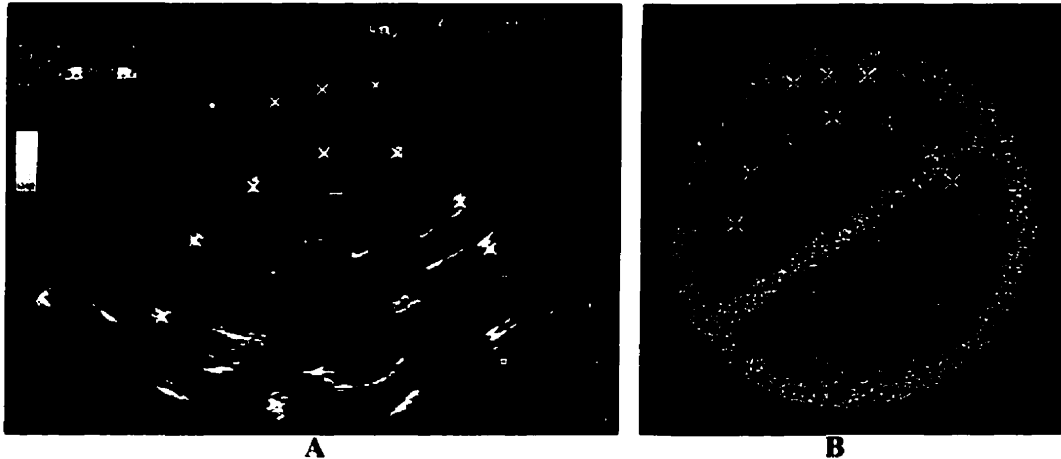


Figure 5-11: Images of the phantom with point annotations (yellow) of homologous cortical and blood vessel points as well as spline curves (green) showing the ventricle outlines. A US image. B: co-planar MR image.

deformation may occur. A 64x64 grid was superimposed on the MR image (Figure 5-12A), and homologous point pairs from the cortical and vessel landmarks (Figure 5-11) were used to define the end-points of a set of deformation vectors. The ventricle spline curves were sampled parametrically to obtain an additional series of end-points pairs and thus additional deformation vectors. The entire vector array was applied to the deformation grid by displacing the grid nodes closest to the vectors. Figure 5-12 B shows the displaced nodes in the grid.

Once the initial conditions were set, the displaced nodes were allowed to propagate. Figure 5-13A shows the resulting displacement grid. The vectors yield an overall view of the deformation. Figure 5-13B shows the displacement magnitudes superimposed on the MR image.

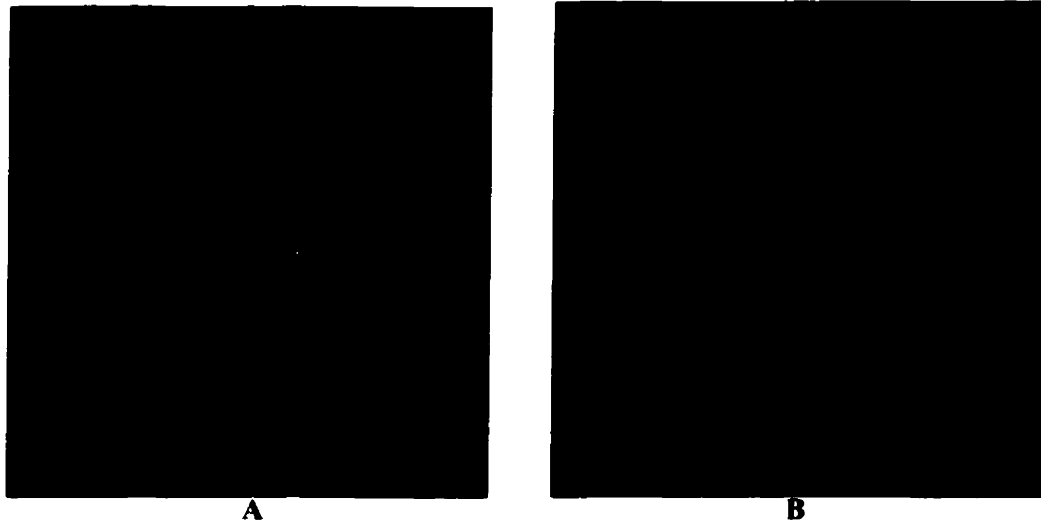


Figure 5-12: A: Deformation grid superimposed on the non-deformed MRI. Red nodes denote nodes within the boundary defining the phantom. B: Initial node displacements from applying deformation vectors calculated from homologous structures defined in Figure 5-11.

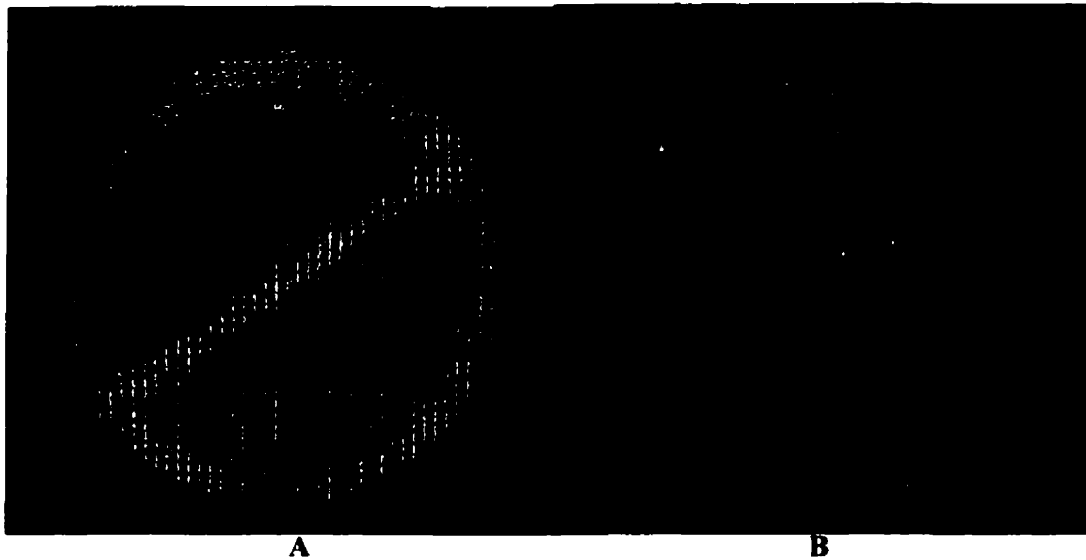


Figure 5-13: A: Interpolated deformation vectors obtained by allowing the initial vectors shown in Figure 5-12B to propagate throughout the grid. B: Magnitude image of the displacements.

5.3.4. Applying Displacement Grid to Non-deformed MRI

After obtaining the deformation grid, it was applied to the MR image. Because the MR image size was 256x256 and the deformation grid was 64x64, linear interpolation was used to calculate the displacements between grid nodes. The ROI tool was used to examine the quality of the restoration of the MRI image by superimposing the US image over the warped MRI (Figure 5-14)

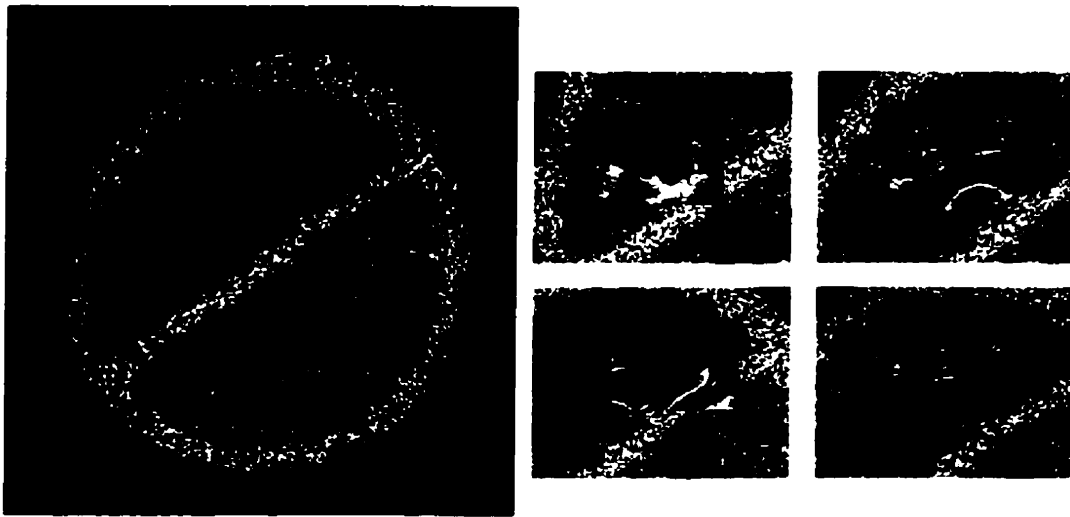


Figure 5-14: Warped MRI obtained by applying the displacement grid shown in Figure 5-13. Closeups of the ROI tool show good agreement between the US and warped MRI in the ventricles and vessels.

5.3.5. Quantitative Analysis of Image Restoration

In order to obtain a quantitative measure of the error in the restoration procedure, the rotating “leave one out” strategy described earlier was employed. Figure 5-15 illustrates one of the vessel points left out. The process was repeated for a second set of US-coplanar MR image pair because the limited field of view of the US only allowed 8 points to be viewed per image pair. A total of 16 homologous point pairs were compared.



Figure 5-15: Homologous points identified from the MR, US and warped (restored) MR images. Just as the US & MR coordinates yielded a vector which defined the deformation at that point, the US & restored MR point yield a measure of the quality of the restoration.

Table 5-2 presents the summary of the point measures for the 16 homologous point pairs. The US-MR comparison provides a quantitative measure of the deformation applied to the phantom, which ranged from 1.1 to 12.2mm. The US-Corr data provides a measure (in *mm*) of how well the correction algorithm functioned. It is worth noting that the max (worst) correction error distance of 4.6mm was far above the other values and occurred in the periphery of the image, where the features used to estimate deformation are sparse. Excluding 2 periphery points, the other 14 out of 16 points have a maximum correction error of 1.9mm.

	US-MR	US-Corr
Mean	7.3	1.3
Max	12.2	4.6
Min	1.0	0.2
Stdev		1.1

Table 5-2: Comparison of point displacements measured (in mm) between homologous US and MR images and US and corrected MR images. The US-MRI column provides a measure of the deformation, while the US-Corr data is a measure of the quality of the correction.

5.4. Discussion

This chapter provided the final checks required to characterize the US based IGNS system. It presented examples of the tools developed to visualize and correct tissue deformation. The non deformed vs. deformed MR analysis demonstrated that the simple iterative propagation/interpolation scheme used to obtain a displacement grid is a reasonable approach, and can yield corrected images with an error on the order of 1mm.

The non deformed MR vs. US images showed that the correction technique can be applied to images of different modalities provided that sufficient homologous landmarks can be found. It is not surprising that the largest correction error encountered was with points on the periphery of the US image. In the periphery of the image, the displacement values obtained are more of an extrapolation from the known points than an interpolation.

Chapter 6

Clinical Use

6.1. Introduction

The previous chapters introduced the concept of image-guided neurosurgery and the various sources of error, the concept of tissue deformation and its impact on IGNS, and finally, our intraoperative ultrasound based IGNS system and its accuracy potential. The final phase of this project was to employ the system in the operating room. This chapter presents the results and experience obtained by using the intraoperative IGNS system in the operating room, by describing several neurosurgical cases where the system was employed.

The potential utility of this system is threefold: First, the surgeon can employ the ROI and annotation tools to quickly compare the intraoperative US images to the pre-operative images to gain a qualitative appreciation of the extent of tissue deformation and monitor the progress of the procedure. Secondly, homologous features may be used to quantify the extent of tissue deformation at any particular time during the procedure, and finally, this information can be used to warp, or correct the co planar pre-operative image.

6.2. Materials and Methods

6.2.1. Operating Room Considerations

Recalling Figure 3-1, the IGNS setup as used in the operating room consisted of two largely distinct systems. This was to ensure that the use of our trial IGNS system in no way affected the natural course of the procedure, and that the usual image guidance tools were always available to the surgeon. In order to use this system in the operating room, it must be relatively unobtrusive physically, and must not interfere with the sterile field.

Figure 6-1 illustrates the positions of the relevant personnel and equipment for most of the procedures where the US based IGNS was used. The physical layout of the equipment and personnel are centralized around the surgeon and the operative field. The

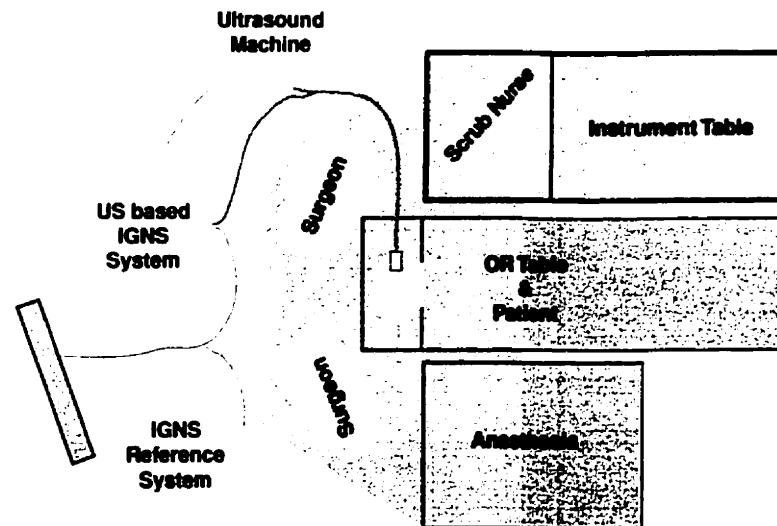


Figure 6-1: Schematic diagram describing the relative positions of the IGNS systems and the operating room staff with respect to the sterile field (green area).

green area represents the sterile field. The surgeons, patient head, scrub nurse and patient end of the anesthetic equipment remain sterile for the duration of the procedure. Equipment that enters the sterile field must also be sterilized.

Due to the limited space around the surgeons and the bulkiness of the equipment, the two IGNS systems and the US machine are placed behind the surgeon. This restriction requires the surgeon to look away from the operative field to examine the images on either IGNS system or the US machine. This has shaped the usage pattern of the IGNS systems in general to be a somewhat off-line approach, where the surgeon places the pointer or US probe to an area of interest and instructs the computer operator to “freeze” the system. This allows the surgeon to put the tool down and turn to view the images of the area of interest.

6.2.2. Patient→Pre-operative Image Registration

Prior to establishing the sterile field, the skull is rigidly fixed to the operating table with a clamp that uses compressed pins that make direct contact with the skull. The reference tracker is attached to the head clamp. The IGNS tracking camera is positioned in such a way as to provide an unobstructed view of the patient’s head.

The non-sterile pointer is used by the surgeon to identify a series of anatomical landmarks on the patient, including the tip and/or bridge of the nose, inner and outer canthi of the eyes and the inter-tragial notch of the ears. As the surgeon delineates each landmark, the computer operator identifies the homologous feature on the pre-operative data on the IGNS workstation. Once identified, the IGNS software calculates and stores the transform.

The registration is verified by using the pointer to identify the scalp surface at various places on the head. As the surgeon places the pointer on the scalp surface, the distance from the cursor location to the scalp surface on the image data is estimated by the computer operator. If the distance exceeds what the surgeon considers acceptable ($\approx 2\text{mm}$), the registration is repeated. Once an acceptable registration has been obtained, the final cleaning of the patient's head is performed, and the sterile field is established using sterile drapes.

6.2.3. Sterilisation of IGNS Tools

All IGNS tools used by the surgeon are either sterilized prior to the procedure or placed in sterile bags. The sterilization method depends on whether the object can tolerate sterilization, and whether it can be kept sterile during all phases of the procedure.

The head reference tracker is attached to the head clamp prior to the application of the sterile drape to allow it to be used for the registration procedure. Once attached, it must remain fixed for the duration of the procedure. To accommodate this, it is placed in a clear sterile bag as the sterile drapes are applied (Figure 6-2 A). The sterile bag is transparent to allow the infrared emissions from the tracker to reach the camera unobstructed.

A non-sterile pointer is used during the initial patient→image registration since the sterile field has not yet been established during the registration phase. After registration, the non-sterile pointer is replaced with a second IGNS pointer which is gas sterilized with Ethylene Oxide prior to surgery. Figure 6-2 A shows the pointer being held by the surgeon in the operative field.

The US transducer used in these experiments is compatible with neither gas nor heat sterilization. Thus, the imaging end of the US transducer is first covered with acoustic gel and then it, and the attached tracker, are placed in a long clear sterile bag (Figure 6-2B). The US transducer end of the bag is kept in the sterile field, while the other end exits the field and allows the cables to be attached to the US machine and the tracking device.

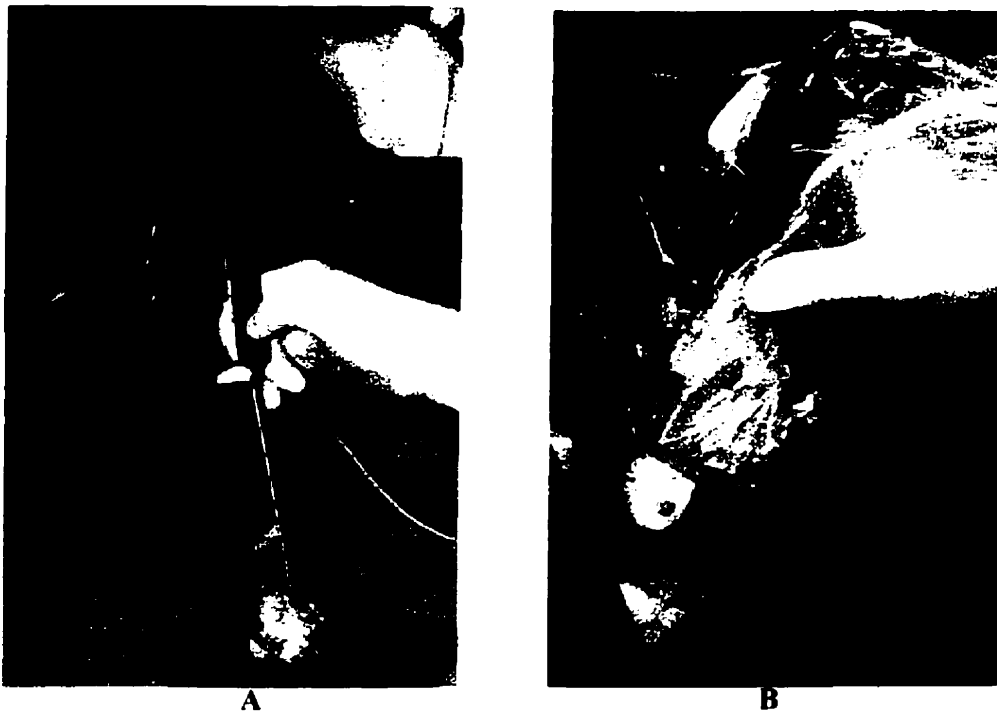


Figure 6-2: A: Intraoperative photograph of the IGNS pointer and head reference tracker. The head reference tracker is in a sterile bag while the probe was gas sterilized, and thus does not require the bag. B: Intraoperative photograph of the US transducer and tracker within the sterile bag.

6.3. Individual Case Reports

The US based IGNS system was used in a variety of cases to assess how well it integrated with the operating room environment, how useful the information would be for different these types of procedures, and to determine where improvements should be

made. This section presents several neurosurgical cases where the US based IGNS system was used. Descriptions of the pathology are provided, as well as observations of the utility of the system for each case.

6.3.1. Syringobulbia and Syringomyelia

The IGNS system was evaluated by using it during procedures where intraoperative ultrasound was already requested. In this first case, ultrasound guidance was required to monitor the IV ventricle and brain stem in a patient with syringobulbia and syringomyelia in the upper cervical spine. A syringo-subarachnoid shunt was inserted, and collapse of the syrinx was monitored by ultrasound. Accoustic coupling was achieved by filling the cavity with saline solution.

6.3.2. Tumour Resection 1

The following example was a neurosurgical case involving extension of a previous tumour resection. The MRI data set was registered with the patient as described above. After US image acquisition, the ROI tool was used to compare the US images to their co-planar MRI equivalents (Figure 6-4). The surgeon was able to qualitatively assess the degree of brain shift by comparing the relative position of homologous structures, including the falx and the tumour boundary. The tumour boundary was manually delineated on the pre-operative MR image using the feature extraction tool, and the resulting curve was overlaid on the US image to further assess the suspected tumour shift.

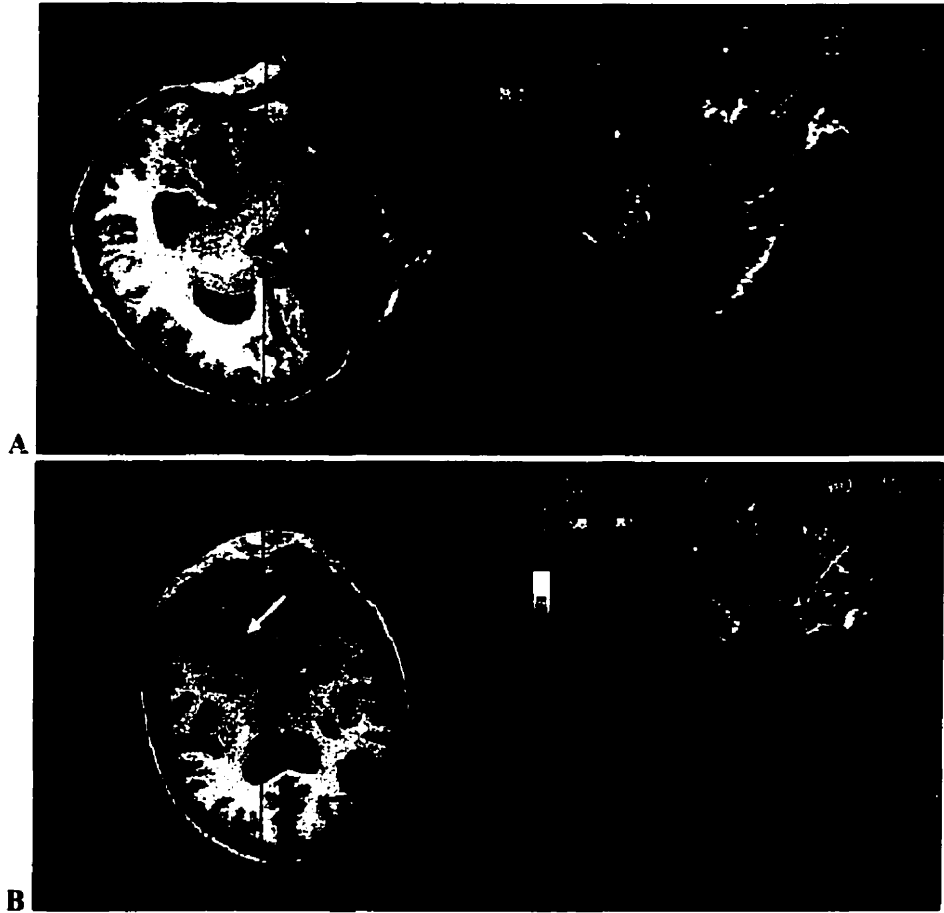


Figure 6-3: A: Coplanar MR and ultrasound images of the IV ventricle. Point annotations help relate the agreement of the boundaries of the ventricle as seen in both images. B: The cerebellum was outlined on the MRI and overlaid on the ultrasound image demonstrating the occurrence of a tissue shift or registration error during the procedure (arrows).

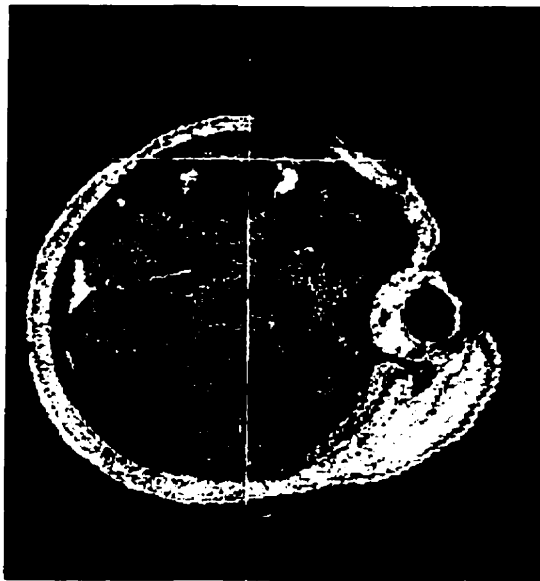
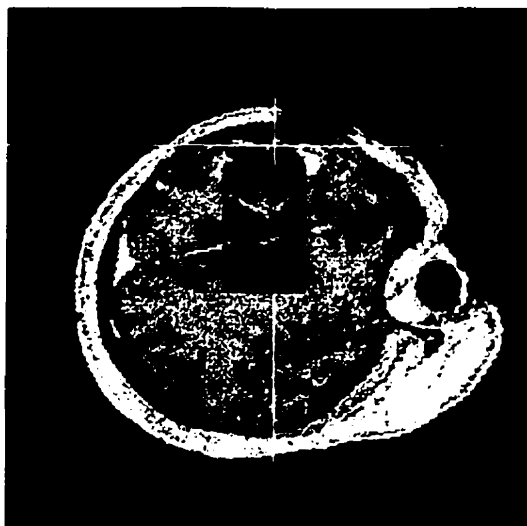


Figure 6-4: Comparison between pre-operative and intraoperative images during a tumour resection. A: Gadolinium enhanced T1 weighted MRI reformatted to match the intraoperative US shown in B.



B: Intraoperative US image showing previous resection boundary and the mid-line (falx, arrow). Light curve (double arrow) indicates resection boundary manually delineated from pre-operative MRI (A)



C: ROI tool display superimposing US onto co-planar MRI. Display shows good agreement in the mid-line while showing a suspected shift in the tumour boundaries.

6.3.3. Tumour Resection 2

This next case involved the resection of a brain metastasis from lung carcinoma in the inferior temporal area. Prior to surgery, a 3D representation of the brain was obtained by performing a curvilinear reconstruction of a pre-operative Gadolinium enhanced T1 weighted MRI.¹¹⁵ Patient→image registration was performed as described above. After the craniotomy, the US transducer was placed on the dura surface and irrigation was applied to ensure good acoustic coupling.

Figure 6-5 shows a screenshot of the US based IGNS software in use during the surgical procedure. The upper images show the transverse and coronal views as well as a 3D surface reconstruction view commonly found in classic IGNS systems. All three views clearly show the tumour enhanced by the Gadolinium contrast agent. The lower left view shows another 3D view of the brain roughly in the same orientation as it was during the surgery. A 3D representation of the transducer (red cylinder) and intraoperative US image (texture-mapped plane) in their orientation at the time of acquisition are also shown. The remaining lower views show the 2D intraoperative US and co-planar MR images respectively.

It was noted that while the tumour was clearly visible in the pre-operative MR images, it could not be viewed in the intraoperative US. Structures surrounding the tumour, including the cortical surface of the temporal lobe could be seen, and its relative position on the US and co-planar MRI evaluated (Figure 6-6A & B). The spline based drawing tool was used to outline the tumour on the MR image, and the resulting curve was displayed on the intraoperative US to aid in interpretation (Figure 6-6C).

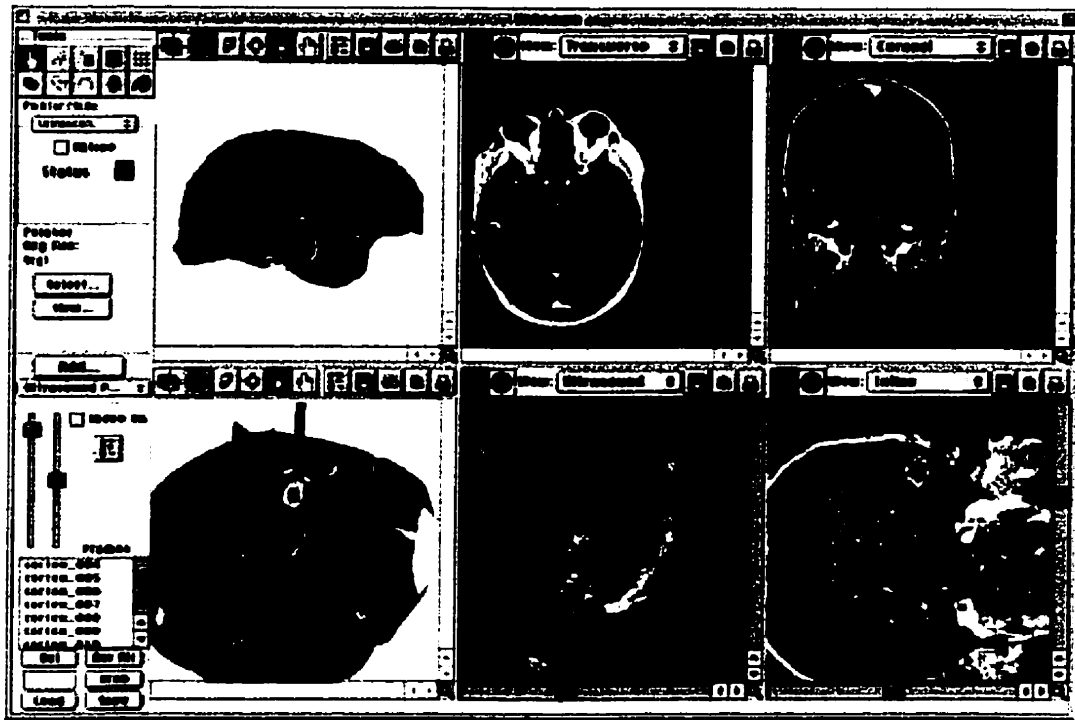
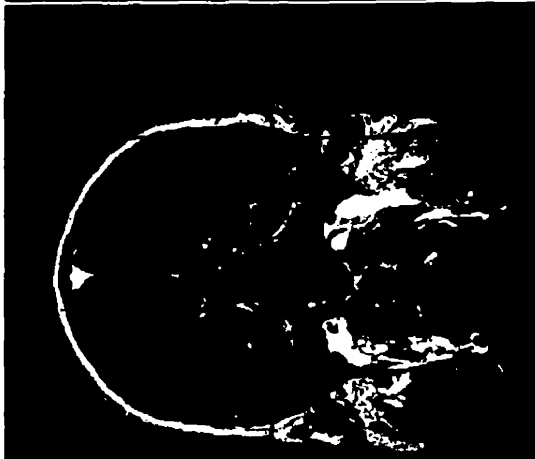


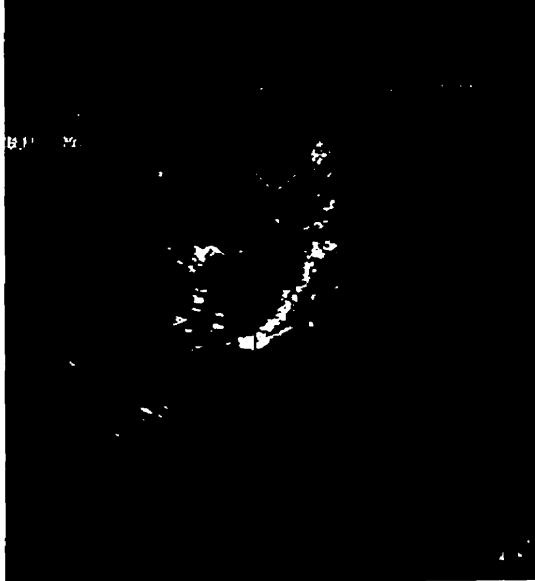
Figure 6-5: Full screen shot of the US based IGNS system. The upper left image shows a 3D surface rendered view of the brain with the probe position of anatomical context. The lower left is the same surface rendered brain and probe, with the addition of skull point samples to delineate the craniotomy and the US image shown in the orientation of its acquisition. The upper right images show the traditional transverse and coronal images, where the tumour can be clearly seen. The lower images show the intraoperative US image and co-planar oblique MRI. The tumour was clearly visible in the MR while it did not enhance well in the US.



Figure 6-6: A: Close-up of the oblique MRI shown in Figure 6-5. The tumour was delineated using the spline drawing tool.



B: Same oblique MRI as in A with the ROI tool overlaying the intraoperative US. The tumour outline from A is also shown.



C: Intraoperative US image with the tumour outlined in A.

6.3.4. Selective Amygdalo- Hippocampectomy

This final example is that of a neurosurgical procedure involving the resection of the hippocampal fomatation (selective amygdalo-hyppocampctectomy) for the treatment of intractable epilepsy. Patient registration and image acquisition were performed as described above, and the Polaris device was used to track the pointer and ultrasound transducer. In this example, we demonstrate the utility of the non-linear warping tool to match the pre-operative MRI to the intraoperative US image.

Figure 6-7 shows relevant images from the case. It can be seen in A, B and C that while there was collapse of the ventricles, the mid-line structures (falx) have remained relatively fixed. Figure 6-7D shows the displacement grid obtained by delineating the ventricles, falx and the skull from the pre-operative MRI and the intraoperative US, and the cortical surface delineated from the pre-operative MRI and the intraoperative sampled surface points. Figure 6-7E shows the deformation magnitude as interpreted from the US image superimposed on the non-deformed MRI. It should be noted that the deformation information is only relevant within the field of view of the US transducer. Finally, Figure 6-7F shows the warped oblique MRI obtained by applying the deformation grid (D). The ventricular collapse as well as the “sinking” of the cortical surface is clearly demonstrated.

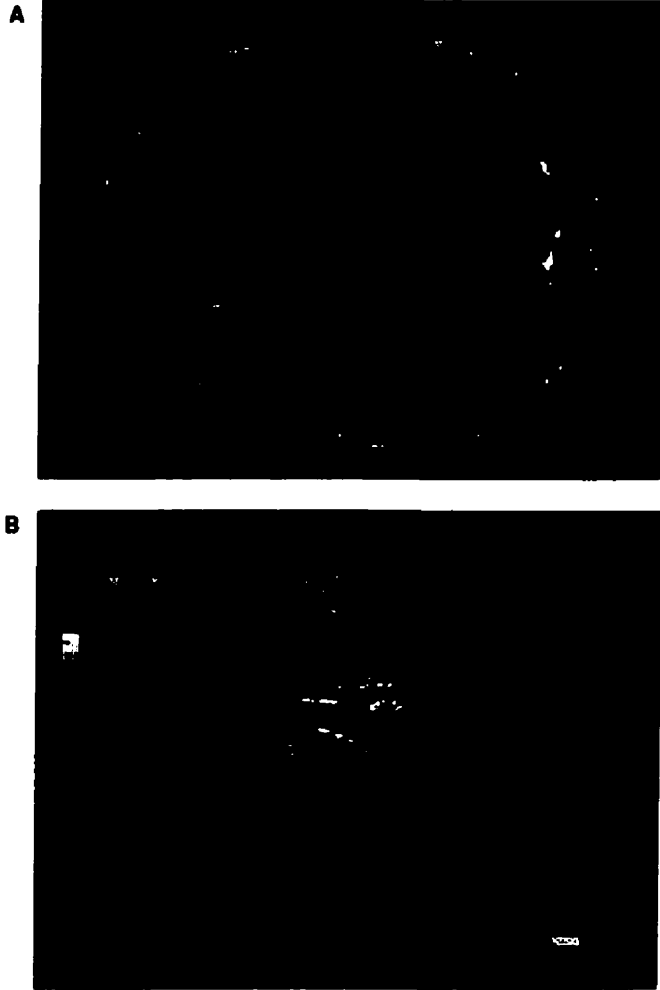
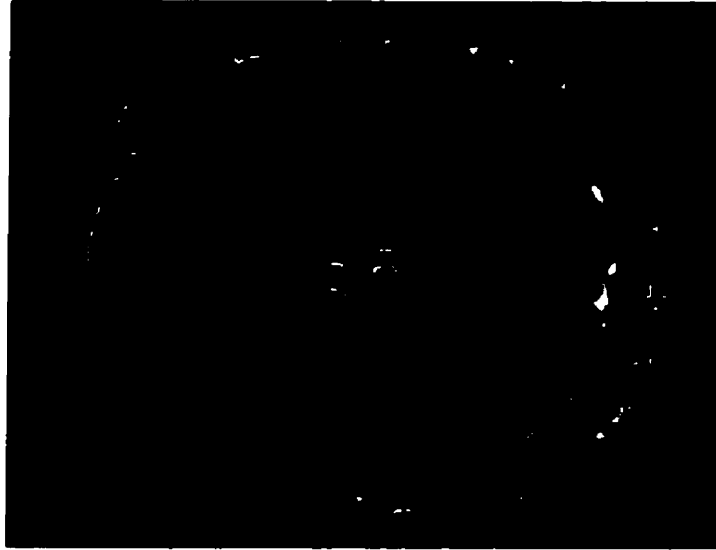


Figure 6-7 A: Oblique MRI view whose orientation is set to match that of the intraoperative ultrasound image (B). The location of the crosshairs indicates the upper center of the ultrasound image, and not the location of the face of the ultrasound transducer. B: Intraoperative ultrasound image of a patient following the craniotomy. The lateral ventricles, falx and brain/dura interface are easily identifiable.

C



D



Figure 6-7 C: Region of interest tool is used to superimpose the ultrasound image over the co-planar MRI. A discrepancy between the pre-operative and intraoperative images is evident in the superior lateral ventricle. D: The spline based drawing tool was used to delineate the ventricle wall, falx and cortical surface. The intraoperative cortical surface was not visible in the ultrasound image, so the surface was derived using the pointer to sample the cortical surface.

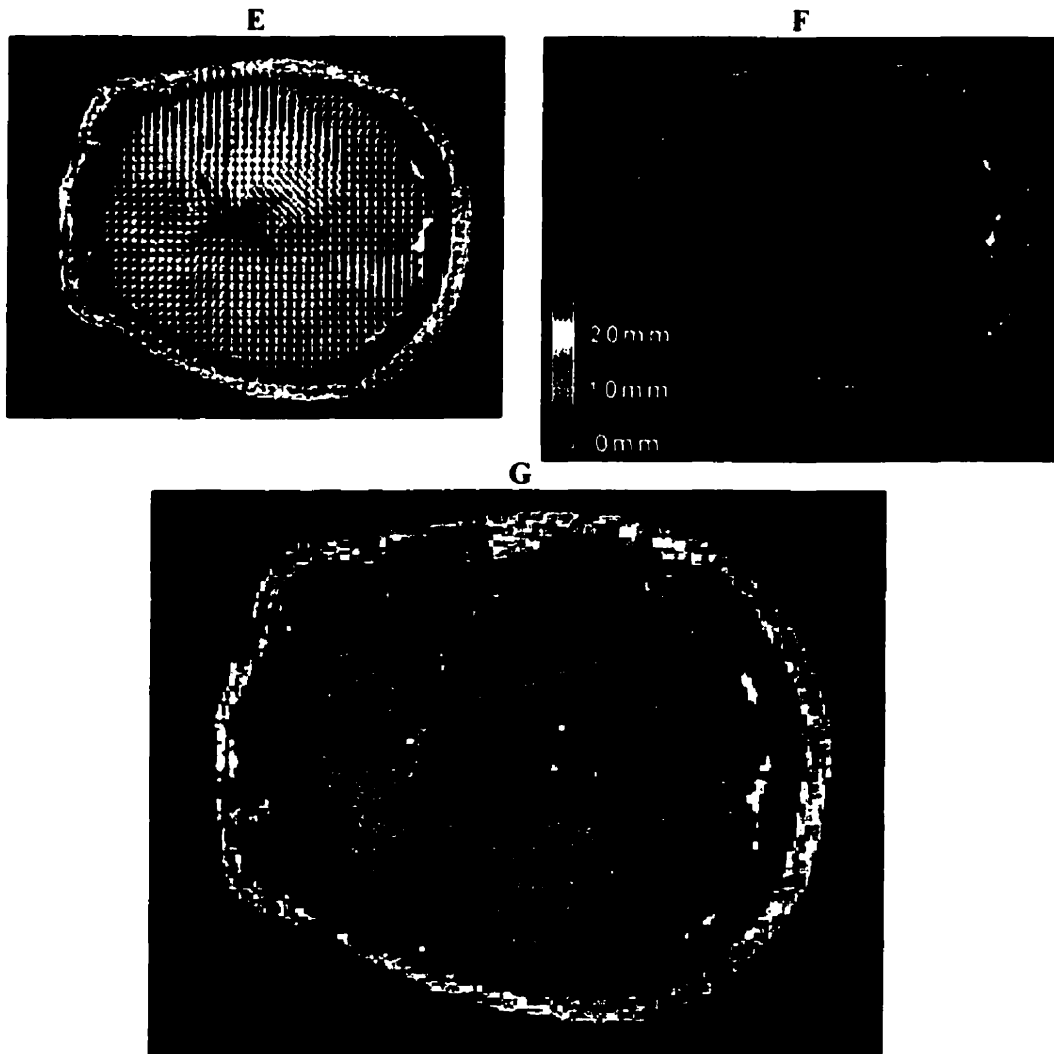


Figure 6-7 E: Deformation grid obtained using the structures outlined in D as an initial condition, and allowed to propagate as described earlier. The lines represent the direction of deformation. F: Superposition of the deformation magnitude over the pre-operative MRI. G: Warped MR image obtained by applying the deformation grid in E to the pre-operative MR.

6.4. Discussion

There are two points of view regarding the integration of intraoperative US and pre-operative MRI for IGNS. One is that intraoperative US is an effective IGNS tool on its own, and incorporation of pre-operative image information enhances its usefulness by providing additional anatomical information to aid in the interpretation of the US images. The other is that pre-operative MRI based IGNS is an effective tool, and that incorporating intraoperative US allows the surgeon to assess and account for the geometrical inaccuracies of the pre-operative MRI caused by tissue movement. The surgical cases described here show that both are true.

Cases one, two and four illustrate where the US aided the surgeon in making better use of the MR images by allowing better appreciation of the nature of the tissue movement. Furthermore the fourth case showed the potential of correction of the geometric inaccuracy caused by the tissue movement. The third case demonstrates where the presence of MRI information augmented the intraoperative US. The tumour was not clearly visible in the US, however, it was possible to superimpose the outline of the tumour derived from the Gadolinium enhanced MRI onto the US, enhancing its usefulness.

6.4.1. Practical considerations

The validation work presented in Chapters 4 and 5 showed the theoretical capabilities and advantages of our intraoperative US based IGNS system. This, in addition to the clinical evaluation trials, shows that the problem of the loss of accuracy due to tissue movement can be successfully addressed with our approach. The clinical setting provides additional challenges in a practical and logistical sense that must be

addressed, if this approach is to evolve from a research topic to a widely accepted, clinical tool.

In our current implementation, the US based IGNS system functions in tandem with a purely pre-operative image based, commercial reference system. While this ensures that the surgeon has a reliable “gold standard” regardless of the performance of our system, it imposes limitations on our set-up that would not otherwise exist. First, the dual system approach requires that the initial patient→image registration be performed twice, adding to the time required for set-up. Secondly, the connections between the tracked tools need to be changed from the reference system to our system each time US based IGNS system is used. This is often difficult as the wires run along the floor by the surgeon’s feet. Thirdly, it is often difficult to fit all the equipment in the space available in the operating room. Presumably, if the intraoperative US functionality were to be built into the reference system, the need for two parallel systems would be eliminated.

We encountered an additional constraint of availability of the US machine itself. Currently, our institution has one machine, which is shared between the radiology department and the neurosurgical operating rooms. Thus, it was often difficult to obtain the US device, or keep it in the operating room for extended periods in case it *might* prove useful, while patients were waiting for scheduled appointments.

While our IGNS system is capable of integrating image information from the US machine with positional information from the tracking device, the overall integration of the system is still sub-optimal. For instance, the only information coming from the US system is video data. The operator is responsible for ensuring that the appropriate calibration (h_pT) for the given US image parameters is used by the IGNS system. In its current form, it would be simple for US images to be acquired with an incorrect

calibration. It would be advantageous therefore, for the IGNS system to be able to query the current state of the imaging parameters that affect the calibration directly from the US device. The IGNS system could then automatically employ the appropriate calibration information without user intervention. Our current US device does not support this type of external communication. It is necessary for US manufacturers to include such an interface into their devices if this improved level of integration is to be achieved.

The ultimate in integration would be to actually combine the US device and IGNS system. This level of integration would allow the IGNS system to take advantage of all the features of the US device and provide a common, simple and efficient interface. In addition, the hybrid US/IGNS device would greatly reduce the space required in the operating room, which as Figure 6-1 shows is already in short supply.

Despite the limitations described above, the system was well received by the neurosurgeons, who are accustomed to the research environment and its idiosyncrasies. If the issues of integration are adequately addressed, intraoperative US will almost certainly become a valuable addition to the standard IGNS system.

Chapter 7

Discussion and Conclusion

7.1. Introduction

The primary goal of this project was to furnish neurosurgeons with an IGNS system having practical intraoperative imaging tools which provide real-time updates of changing tissue morphology during the course of the operation. This is intended to complement the pre-operative image data, which may have richer anatomical and functional information, but may suffer from lower geometric accuracy due to changes in the brain during the operation. The second goal was to develop qualitative and quantitative tools to visualize, measure and correct these geometric distortions on selected pre-operative images. This thesis presents work that achieved the goals stated above, including the development of an intraoperative US based IGNS system, as well as imaging phantoms and calibration tools required to calibrate and validate the system. This chapter summarizes the work described earlier, and attempts to put it in perspective by suggesting areas where future work would be most productive.

Our IGNS system employed US to acquire intraoperative images, and map them to corresponding images derived from the pre-operative data, usually MRI. US was selected over intraoperative MRI because of its acceptable image quality, familiarity in neurosurgical guidance and low intrusion in the operating room. The mapping was

achieved by employing a position sensor to track a pointer and US transducer, and performing a series of calibration steps described in Chapter 2 to determine the affine transformation from US image to pre-operative image space.

7.2. Special Tools and Phantoms

Throughout this project, specialized imaging phantoms were required for calibration, characterization and validation of the intraoperative US IGNS system. While some of these are similar to typical commercial phantoms used for US quality assurance procedures, others constitute a portion of the work that is unique to this project.

7.2.1. Calibration Tool (Phantom)

A novel calibration technique was presented, employing a unique calibration tool using Z-bar fiducial markers. This approach simplified image acquisition, and helped minimize the contribution of image partial volume effects on calibration accuracy. Several versions of the phantom were developed and presented, each having improvements over the previous one. The two criteria evaluated were the geometrical configuration of the fiducial marker(s) and the material used to construct them to provide the desired fiducial marker contrast.

The final calibration tool was ultimately the simplest. While the first two versions used multiple Z-bars in different orientations to increase the number of homologous point pairs per image, the final calibration tool had only one z-bar fiducial marker. It proved to be more difficult to acquire a few calibration images with multiple fiducial markers clearly visible in each image than to acquire several images having one clearly visible fiducial marker.

The Z-bar segments had to be designed to allow high contrast between them and the surrounding medium. Two configurations were evaluated: hollow tubes filled with either water or imaging-modality specific contrast agent, and solid PVA-C strands. The thin hollow tube approach provided images that were easiest to visualize in both US and CT (Figure 7-1). The thin walls provided good contrast as fiducial “rings” in the US images while filling the tubes with Iothalamate meglumine provided excellent solid disc images in CT. Similarly, an MRI contrast agent (e.g. CuSO_4) solution can be used if one wished to generate contrast in MRI.

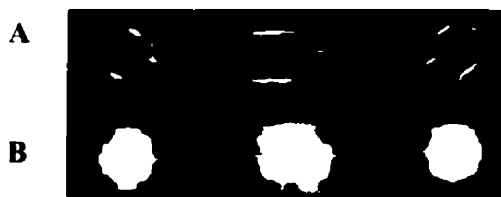


Figure 7-1: Cross section image of the hollow tube Z-bar fiducial marker. A: Filled with water for US imaging, with the tube walls generating contrast. B: Filled with Iothalamate meglumine to generate contrast in CT.

The final design of the calibration tool is similar to other single target calibration tools described in section 2.5.2.2 with a few significant exceptions. The Z-bar fiducial marker provides three benefits: First, the Z-bar is less susceptible to partial volume effects caused by thick US slices than the small targets used by others. Second it is easier to image, as the user need not centre the US slice over a small target. Instead of imaging a target at a known location, the location of the target within the phantom is determined after imaging. Finally, the multimodality imaging capability enables it to be employed to evaluate the overall accuracy of the IGNS system by allowing the locations of targets in simulated pre-operative and intraoperative images to be mapped to a common coordinate space for comparison.

7.2.1.1. Suggested Future Work

While the software and final calibration tool met the goals of the project, improvements can be made to simplify the calibration procedure, particularly if it is to be used in a routine clinical environment.

First, the calibration tool should be built as a sealed block to simplify its handling. This can be accomplished by using a flexible membrane to seal the top of the tool and providing an imaging aperture whose distance from the target can be altered. Second, integration of the tool with the tracking device could be achieved by attaching a tracker to it. This would allow the tool's position and orientation in the tracking device's frame of reference to be obtained without the need for identifying the divot holes on the tool. This would have the added benefit of not having to fix the phantom to a constant location during image acquisition, as each image could be tagged with the tool's position at the time of acquisition. Figure 7-2 illustrates such a design.

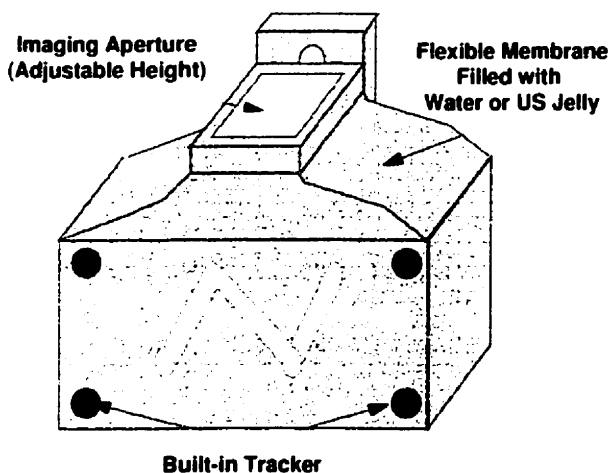


Figure 7-2: Suggested design enhancements for a calibration tool for simpler and more efficient use in a clinical environment. The adjustable height aperture and flexible membrane allow US images to be made of the Z-bar at various heights without adding or removing US jelly.

The software could also be improved to simplify the calibration process. First, machine vision techniques could be employed to automatically extract the fiducial markers in the image. Second, the software could automatically recognize the presence of

the tracker attached to (or embedded in) the tool, eliminating the process of identifying the pivot holes.

7.2.2. Deformable Phantom

While the literature reviewed in chapter 2 described many approaches to the calibration problem, little attention was paid to system validation. Our validation process was performed in two steps. First, the system's static accuracy of mapping points from intraoperative US space to pre-operative image space was measured. Secondly, the system's ability to demonstrate, measure and correct for intraoperative tissue movement was characterized. The former was achieved using the calibration tool described above, while the latter using a deformable multimodality imaging phantom.

The deformable phantom we developed was presented in section 3.5.2. It consisted of a Poly(vinyl alcohol) cryogel (PVA-C) disk containing anatomy mimicking sections of PVA-C of varying concentrations which provided contrast in both material stiffness and in MR relaxation times. The phantom allowed us to obtain MR images that simulated pre-operative images, and then register the phantom to those images as we would with a patient in the operating room. It allowed us to apply pressure to the phantom to deform and move the internal structures. Finally, the phantom could be imaged with US as an intraoperative imaging simulation. This provided the simulated data required for us to evaluate the intraoperative IGNS system's tools to visualize, measure and correct for tissue deformation.

7.2.2.1. Suggested Future Work

The deformable phantom proved to be useful in helping us characterize the intraoperative US based IGNS system. Given that, improvements can be made to make a better phantom. First, the phantom's simulated anatomical parts have only 2 degrees of

variability. That is, one can think of the phantom as an extrusion of a 2D form, with an ambiguity in the axis of the extrusion. This limits the phantom's usefulness in studying potential partial volume effects caused by US image slice thickness when comparing it to MR images. Secondly, while the simulated structures look reasonably realistic in the case of the ventricles and cortical surface, the simulated blood vessels contain no simulated blood flow.

As outlined in section 3.5.2.1, the anatomy mimicking PVA-C pieces were constructed by cutting molds of their shapes out of blocks of Plexiglas using a milling machine. More sophisticated tools can be used to create more complex shapes, eliminating the longitudinal ambiguity of the present phantom. These could also be employed to create shapes that, in a visual sense, better mimic the structures of the brain. This can provide a more realistic anatomical feature set to examine, including more complex convolutions of the sulci and the gray/white matter structures of the cortex.

If the simulated blood vessels were to contain moving blood mimicking fluids, dynamic US imaging, namely Doppler and power Doppler imaging can be used to obtain US images of the simulated brain's vasculature. These can be compared to MR angiography (MRA) images using the vascular tree as a feature set to detect and measure brain deformation.

7.3. System Characterization

Experiments were performed to first characterize the US image/computer frame grabber system, measure the tracking device precision, and then to evaluate the overall system accuracy in mapping intraoperative targets to pre-operative image space.

The parameters used to characterize the US image/computer frame grabber system were the pixel size (FWHM), US image slice thickness, and finally the geometric distortion. These measurements were performed using imaging phantoms whose construction is described in section 3.5, and employing procedures described in 4.2.

The tracking device precision was determined by calculating the standard deviation of the measured distances between a series of divot holes at known locations (and at constant distances from each other) using the tracked pointer.

The overall system accuracy was determined by co-registering the calibration tool with a volumetric CT data set of the tool with the tubes filled with contrast agent, and obtaining a series of US and co-planar CT images of a target (Z-bar fiducial marker). The fiducial marker was identified on each image, and the distances between homologous targets were calculated (described in section 4.5).

Recalling equation 2-3, the total error of the system in mapping points from US image space to pre-operative image space is the sum of the errors from each transformation. With the exception of the patient→image transformation, the precision of each step was measured. The overall system accuracy was also measured using the calibration tool; however the values reported are intended as "best case" figures given that one important source of error, T , the patient→image registration was essentially removed from the method. In this measurement, our registration method used well-defined divot holes on the calibration tool as homologous points for registration. These divots can be accurately identified with the pointer, and when filled with contrast agent, on the images as well. In the operating room, anatomical landmarks on the skin surface are commonly used as homologous points. In practice, these points are not as easily defined, and may also have moved between the time of imaging and surgery, resulting in

inferior registration. As described in section 2.3.4.2, improving registration quality often necessitates use of fixed fiducial markers, which is more laborious and invasive.

7.4. Visualization and Measurement vs. Modeling and Predicting

The emphasis in much of the literature regarding brain deformation has been on measurement, to confirm the presence of this phenomenon, and on modeling, by attempting to correlate the measured movement with various factors. Some of these factors include tumor size or type, blood or CSF pressure, or even patient age, and are combined with finite element model (FEM) approaches to develop predictors of shift.

Given the complexity of such an approach, and the critical importance of the accuracy of the information on surgical outcome, our approach is not to attempt to predict the movement, but to provide simple and effective tools to visualize and measure the movement for every case. This eliminates the need to model and predict tissue movement, since the movement will be known. This necessitates that the equipment required to measure such movement be available in the operating room. This was one reason we selected US, as it is readily available and familiar to the neurosurgical staff.

7.5. Deformation Detection

In the context of this project, detecting deformation refers to the surgeon appreciating that there is a difference between the state of the structures in the skull as displayed in the pre-operative images, and as they are intraoperatively. This detection is performed manually by the surgeon using either the qualitative visualization tools and/or the quantitative feature delineation tools described in section 3.3.5.

7.5.1. Suggested Future Work

Probably the most significant area for future work is to automate the process of feature extraction and deformation detection. The manual feature extraction tools demonstrated here provide a good proof of concept, in that they demonstrate the utility of comparing features between pre- and intraoperative images to evaluate tissue movement. Providing manual feature extraction tools ensures that the operator takes responsibility for the selection of the appropriate features. In order to make these tools more acceptable to the surgeon, as much of the user intervention as possible should be removed from the process. This requires work in image processing and machine vision. Automation of this process should, however, always require user intervention at critical decision making steps to either accept or reject the features detected and employed to assess deformation.

First, examination of the homologous features, as represented on the respective images must be examined. The features that generate diagnostic contrast must be the same (or correlate with each other) for the two modalities employed. Certain structures, including the ventricular wall, the falx, the vessels and cortical folds when visible in US (i.e. tissue/CSF interfaces) may be easily and reliably matched between MR, CT and US. The validity of other features, for example the tumour border as seen in US and infused MRI, must be examined before they can be reliably used as features for movement detection and correction.

In order to extract features from an image, the structures must first be classified. Automatic tissue classification from MRI data of the brain is a complex problem, and a field of great interest in our institution. A direction that may be promising is to apply atlas- and model-based segmentation tools to automatically segment the MRI data. The structural classification may be used to query atlas information, allowing one to convert from MRI intensity information to their corresponding US response information, yielding

an MRI derived image whose features are more compatible for comparison with the intraoperative US.

Image processing may be performed on either the raw MR image or a pre-processed image as proposed above to try to create images with more similar features suitable for matching. The concept is illustrated in Figure 7-3, where a steerable gradient filter, whose direction was set to a fan pattern simulating the US beam, was applied to the MR image. The resulting image is edge-enhanced in a manner that mimics the tissue interfaces as portrayed by the US image. This approach may yield images more amenable

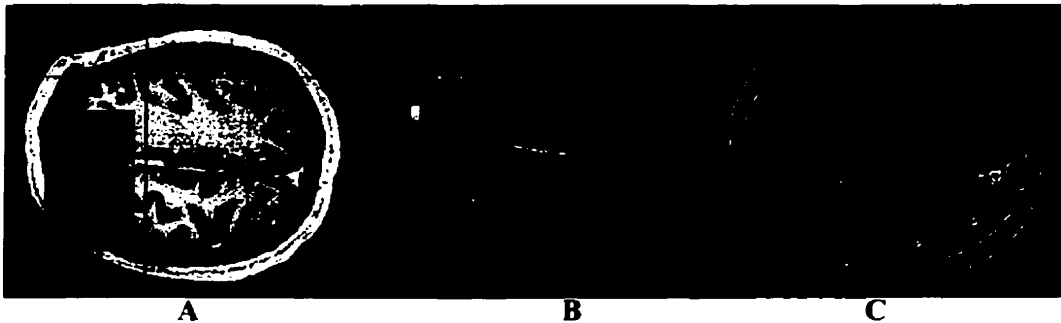


Figure 7-3: Simple example of image processing to alter the MRI data to better resemble the US data for comparison. A: Oblique MRI (with no filtering) with co-planar US displayed in the ROI box. B: US image. C: Steer-able gradient filtered MRI with co-planar US shown in the ROI box.

to automatic feature matching.

7.5.2. Research Utility-Deformation Measurement of Multiple Cases

While performing correlation analysis of multiple cases for modeling purposes is not a stated goal of this project, it is of considerable interest in our laboratory as a tool for model validation.¹⁰⁰ This intraoperative based IGNS system can be employed to obtain

deformation data on both the surface of the dura or the cortex by using the pointer to sample the surface with a cloud of points, and under the surface using US.

As an example, data were collected during four operating room cases with a similar protocol. For each case, after registration and skin incision, a series of points ($n \approx 25$) were sampled with the pointer on the skull surface. The skull points can be used to further evaluate the registration quality, although no correction of registration is possible at that point. Following the craniotomy, a second set of points was acquired to sample the dura surface. After the dura had been opened, an additional point set was acquired over the surface of the cortex. Ultrasound images were also acquired by lightly placing the transducer on the dura and later on the cortical surface and applying irrigation for acoustic coupling.

The shortest distance from each sampled point to its respective surface was obtained using the distance measurement tool. The spline based drawing tool was used to delineate the ventricle wall and the falx on appropriate US and co-planar MR images. The spline curves of these homologous structures were sampled parametrically to obtain a series of discrete vectors representing the direction of movement of the delineated structures. The lengths of these vectors were noted. Table 7-1 summarizes the measurements for the four cases.

While the number of cases is insufficient to draw any concrete conclusions, it is interesting to note that in 3 of the 4 cases, the predominant direction of motion of the cortical surface is opposite to the predominant direction of the skull movement (shift is not due to registration error). In contrast, the direction of movement of the falx is similar to that of the skull, suggesting it may be more due to registration error than movement of the brain tissue. This agrees with intraoperative MRI studies as well as personal observations of the surgical staff. This finding may suggest that a convenient boundary

Patient		S.A.	B.C.	M.D.	J.L
Skull	Mean	1.09	0.60	1.32	1.09
	Max	2.30	2.50	4.50	4.20
	Min	0.30	0.00	-0.90	-2.10
	Stdev	0.54	0.74	1.62	1.44
Dura	Mean	0.60	-1.15	-1.59	-1.41
	Max	4.40	0.70	0.60	3.70
	Min	-1.20	-3.50	-4.00	-7.30
	Stdev	1.41	1.27	1.33	2.98
Cortex	Mean	-0.61	-2.44	-3.60	-4.80
	Max	0.50	0.00	-1.40	-1.10
	Min	-4.90	-4.50	-5.00	-10.80
	Stdev	1.43	1.59	1.22	3.01
Ultrasound (Ventricle Wall)	Mean	2.65	1.73	1.47	6.46
	Max	3.94	2.56	3.05	7.42
	Min	0.70	1.05	0.34	4.77
	Stdev	1.09	0.51	0.82	0.88
Ultrasound (Falx)	Mean	2.51	1.98	1.59	2.87
	Max	2.80	2.69	2.99	3.76
	Min	1.71	1.23	0.82	0.93
	Stdev	0.36	0.43	0.63	1.04

Table 7-1: Data collected from 4 operating room cases performed using the same data acquisition protocol.

condition may be employed in the deformation process, restricting the calculations to the hemisphere affected by the surgery. If this proves to be consistent, it will have to be accounted for in current finite element model based approaches to characterizing the deformation. The dynamics of tissue movement are less clear in procedures involving the falx itself.

7.6. Clinical Utility

The ultimate measure of success of this project lies in its clinical utility. Our intraoperative US based IGNS system was found to be of benefit on several levels.

- The simple ability to view oblique MRI images alongside their US counterparts improved the appreciation of the US images
- The visualization tools, which enabled direct comparison of the pre- and intraoperative images, were useful in evaluating the effects of registration error, brain tissue shift and tissue removal on the overall accuracy of the system
- The ability to use homologous features manually identified by the operator to quantify and correct for tissue shift shows promise in the concept of warping pre-operative image information to correct for this shift
- As with other investigators, the information gathered to measure and correct for shift for each case can be accumulated over several cases to determine broad factors that influence this shift, or as a validation tool for other methods of correction

7.6.1. Integrated US Guidance

All the visualization and measurement tools developed to compare the intraoperative and pre-operative image information rely on the availability of co-planar US and MR images. This simple integration of the two modalities as side-by-side images is a significant improvement over purely pre-operatively based IGNS systems or US imaging alone. One complaint often heard regarding US images is the difficulty in orienting the oblique slice within the volume, and thus recognizing the structures in the image. The presence of the co-planar MR image gives the surgeon (and radiologist) an additional image from which to determine orientation, making the US more recognizable.

In addition to the co-planar views, the surgeon can use the 3D reconstruction derived from the MR images as a guide (see lower 3 images of Figure 6-5).

7.6.2. Deformation Visualization and Measurement

The visualization tools, particularly the movable ROI tool, provide the surgeon with the most relevant information with little required interaction with the computer. It allows the surgeon to rapidly compare the relative positions of homologous anatomical features without having to explicitly identify them. It requires only a few seconds and can be performed on any co-planar image data set. The manual feature extraction tools, while requiring more work than the ROI tool, provide a more quantitative method of comparing homologous features.

7.6.3. Image Warping

In its current implementation, the image warping tools are cumbersome to perform in the operating room during a procedure. Still, they can be performed in an off-line fashion during surgery and reviewed retrospectively by the surgeon. As described above, the image warping tool will become more valuable as more automated methods of feature extraction and matching are developed.

7.7. Conclusion

Ultrasound imaging has had a prominent past as an invaluable tool in many neurosurgical procedures. While initially it seemed that the emergence of pre-operative MRI or CT based IGNS tools threatened this prominence, it is interesting to see that the two strategies have converged to complement each other instead. While as described in 6.4.1, many of the practical limitations encountered in IGNS lie in the lack of integration,

we can begin to see with this work the potential that integration offers. While this project has investigated the integration of intraoperative US, the general notion of integration of other modalities should be considered in the context of IGNS, notably intraoperative CT, fluoroscopes and microscopes.

Finally, this work serves as a foundation for future work in improving the integration of ultrasound into IGNS as a valuable tool for real-time automatic image based monitoring of surgical procedures.

Glossary of terms

IGS: Image guided surgery

IGNS Image guided neurosurgery

MRI Magnetic resonance imaging/images

CT: Computed tomography (formerly known as CAT scan)

US: Ultrasound

MID: Maximum imaging depth: The maximum imaging depth represents the distance from the transducer face to the most distal tissue displayed at the bottom of the screen.

MINC: Medical Image NetCDF. Multidimensional image file format developed at the Montreal Neurological Institute

DICOM: Common medical image transfer and file storage protocol.

ACR/NEMA: Medical image file format (precursor to DICOM) defined by the American College of Radiology (ACR) and the National Electrical Manufacturers Association (NEMA).

References

- 1 A. Olivier, G. Bertrand and C. Picard, "Discovery of the first human stereotactic instrument," *Applied Neurophysiology* **46** (1-4), 84-91 (1983).
- 2 R. L. Jensen, J. L. Stone and R. Hayne, "Use of the Horsley-Clarke stereotactic frame in humans," *Stereotactic & Functional Neurosurgery* **65** (1-4), 194-7 (1995).
- 3 A. Olivier, G. Bertrand and T. Peters, "Stereotactic systems and procedures for depth electrode placement: technical aspects," *Applied Neurophysiology* **46** (1-4), 37-40 (1983).
- 4 M. P. Heilbrun, T. S. Roberts, M. L. Apuzzo, T. H. Wells, Jr. and J. K. Sabshin, "Preliminary experience with Brown-Roberts-Wells (BRW) computerized tomography stereotaxic guidance system," *Journal of Neurosurgery* **59** (2), 217-22 (1983).
- 5 L. A. Rees Ramos, G. H. Barnett, C. P. Steiner and D. W. Kormos, "Modifications of the compass stereotactic magnetic resonance localizer: technical note," *Stereotactic & Functional Neurosurgery* **60** (4), 205-9 (1993).
- 6 M. Levivier, S. Goldman, B. Pirotte and J. Brotchi, "First year experience using the Fischer ZD-Neurosurgical Localizing Unit with particular reference to the development of PET-guided stereotactic biopsy," *Acta Neurologica Belgica* **93** (1), 5-22 (1993).
- 7 E. R. Cosman and T. H. Wells, Jr., "Combined use of a new target-centered arc system with the BRW floor stand and phantom base for a wider range of approaches and

applications in stereotaxy of the head and neck." *Applied Neurophysiology* **50** (1-6), 119-26 (1987).

8 D. Dormont, M. Zerah, P. Cornu, F. Parker, B. Aubert, R. Sigal, J. P. Francke, A. Zouaoui and C. Marsault, "A technique of measuring the precision of an MR-guided stereotaxic installation using anatomic specimens," *American Journal of Neuroradiology* **15** (2), 365-71 (1994).

9 G. Bertrand, A. Oliver and C. J. Thompson, "The computerized brain atlas: its use in stereotaxic surgery," *Transactions of the American Neurological Association* **98**, 233 (1973).

10 M. S. Goldman and P. J. Kelly, "Stereotactic thalamotomy for medically intractable essential tremor," *Stereotactic & Functional Neurosurgery* **58** (1-4), 22-5 (1992).

11 R. L. Alterman, B. Kall, A. Beric, D. Sterio and P. J. Kelly, "Pallidal targeting with the COMPASS system," *Stereotactic & Functional Neurosurgery* **69** (1-4 Pt 2), 69-72 (1997).

12 P. St-Jean, A.F. Sadikot, L. Collins, D. Clonda, R. Kasrai, A.C. Evans and T.M. Peters, "Automated Atlas Integration and Interactive Three-Dimensional Visualization Tools for Planning and Guidance in Functional Neurosurgery," *IEEE Transactions on Medical Imaging* **17** (5), 672-680 (1998).

13 B. S. Carter and G. R. Harsh, "Diagnosis of suspected intracranial metastases. Role of direct tissue examination," *Neurosurgery Clinics of North America* **7** (3), 425-33 (1996).

14 I. Fedorcsak, L. Sipos, F. Slowik and E. Osztie, "[The role and importance of CT-guided stereotaxic brain biopsy in neurosurgery. Experiences with 523 cases]," *Orvosi Hetilap* **139** (9), 475-8 (1998).

15 D. A. Ross, J. A. Brunberg, I. Drury and T. R. Henry, "Intracerebral depth electrode monitoring in partial epilepsy: the morbidity and efficacy of placement using magnetic resonance image-guided stereotactic surgery," *Neurosurgery* **39** (2), 327-33; discussion 333-4 (1996).

16 E. A. Popovic and P. J. Kelly, "Stereotactic procedures for lesions of the pineal region," *Mayo Clinic Proceedings* **68** (10), 965-70 (1993).

17 J Craig, "More on representation of orientation," in *Introduction to Robotics, Mechanics and Control* (Addison-Wesley, Don Mills, ON, 1989), pp. 43-56.

18 E. Watanabe, Y. Mayanagi, Y. Kosugi, S. Manaka and K. Takakura, "Open surgery assisted by the neuronavigator, a stereotactic, articulated, sensitive arm," *Neurosurgery* **28** (6), 792-9; discussion 799-800 (1991).

19 R. L. Galloway, Jr., R. J. Maciunas and C. A. Edwards, "Interactive image-guided neurosurgery," *IEEE Transactions on Biomedical Engineering* **39** (12), 1226-31 (1992).

20 T. Takizawa, "Neurosurgical navigation using a noninvasive stereoadapter," *Surgical Neurology* **40** (4), 299-305 (1993).

21 L. Zamorano, Z. Jiang and A. M. Kadi, "Computer-assisted neurosurgery system: Wayne State University hardware and software configuration," *Computerized Medical Imaging & Graphics* **18** (4), 257-71 (1994).

22 P. K. Doshi, L. Lemieux, D. R. Fish, S. D. Shorvon, W. H. Harkness and D. G. Thomas, "Frameless stereotaxy and interactive neurosurgery with the ISG viewing wand," *Acta Neurochirurgica - Supplementum* **64**, 49-53 (1995).

23 Andrei State, Mark A. Livingston, William F. Garrett, Gentaro Hirota, Mary C. Whitton, Etta D. Pisano and Henry Fuchs, "Technologies for augmented reality systems: Realizing ultrasound-guided needle biopsies," *Proceedings of the ACM SIGGRAPH Conference on Computer Graphics* **1996**, 439-446 (1996).

24 R. Rohling, P. Munger, J. M. Hollerbach and T. Peters, "Comparison of relative accuracy between a mechanical and an optical position tracker for image-guided neurosurgery," *Journal of Image Guided Surgery* **1** (1), 30-4 (1995).

25 S. J. Goerss, P. J. Kelly, B. Kall and S. Stiving, "A stereotactic magnetic field digitizer," *Stereotactic & Functional Neurosurgery* **63** (1-4), 89-92 (1994).

26 W. K. Doyle, "Low end interactive image-directed neurosurgery. Update on rudimentary augmented reality used in epilepsy surgery," *Medicine Meets Virtual Reality. Health Care in the Information Age. Proceedings of Medicine Meets Virtual Reality* **4**, 1-11 (1996).

27 W. Birkfellner, F. Watzinger, F. Wanschitz, G. Enislidis, C. Kollmann, D. Rafolt, R. Nowotny, R. Ewers and H. Bergmann, "Systematic Distortions in Magnetic Position Digitizers," *Medical Physics* **25** (11), 2242-2248 (1998).

28 L. J. Zamorano, L. Nolte, A. M. Kadi and Z. Jiang, "Interactive intraoperative localization using an infrared-based system," *Neurological Research* **15** (5), 290-8 (1993).

29 R. L. Galloway, R. J. Maciunas, W. A. Bass and D. Crouch, "Optical device for interactive, image-guided neurosurgery," Proceedings of the Annual Conference on Engineering in Medicine and Biology. Publ by IEEE, IEEE Service Center, Piscataway, NJ, USA **15**, 954-955 (1993).

30 L. Adams, A. Knepper, D. Meyer-Ebrecht, R. Ruger and W. van der Brug, "An optical navigator for brain surgery," Computer **29** (1), 48-54 (1996).

31 C. Schaller, B. Meyer, D. van Roost and J. Schramm, "Image guided microsurgery with a semifreehand neuronavigational device," Computer Aided Surgery **2** (3-4), 162-71 (1997).

32 K. Roessler, K. Ungersboeck, M. Aichholzer, W. Dietrich, H. Goerzer, C. Matula, T. Czech and W. T. Koos, "Frameless stereotactic lesion contour-guided surgery using a computer-navigated microscope," Surgical Neurology **49** (3), 282-8; discussion 288-9 (1998).

33 K. Holton-Tainter, J. Zhao and A. C. F. Colchester, "Accuracy of the VISLAN intra-operative pointer in localising markers from pre-operative images," Second Annual International Symposium on Medical Robotics and Computer Assisted Surgery. MRCAS '95. Wiley Liss **83** (2) (1995).

34 T. M. Peters, C. J. Henri, P. Munger, A. M. Takahashi, A. C. Evans, B. Davey and A. Olivier, "Integration of stereoscopic DSA and 3D MRI for image-guided neurosurgery," Computerized Medical Imaging & Graphics **18**, 289-299 (1994).

35 E. Alexander 3rd, H. M. Kooy, M. van Herk, M. Schwartz, P. D. Barnes, N. Tarbell, R. V. Mulkern, E. J. Holupka and J. S. Loeffler, "Magnetic resonance image-directed

stereotactic neurosurgery: use of image fusion with computerized tomography to enhance spatial accuracy," *Journal of Neurosurgery* **83** (2), 271-6 (1995).

36 K. J. Burchiel, T. T. Nguyen, B. D. Coombs and J. Szumoski. "MRI distortion and stereotactic neurosurgery using the Cosman-Roberts-Wells and Leksell frames," *Stereotactic & Functional Neurosurgery* **66** (1-3), 123-36 (1996).

37 T. S. Sumanaweera, J. R. Adler, G. H. Glover, P. F. Hemler, P. A. van den Elsen, D. Martin and S. Napel, "Method for correcting magnetic resonance image distortion for frame-based stereotactic surgery, with preliminary results," *Journal of Image Guided Surgery* **1** (3), 151-7 (1995).

38 C. R. Maurer Jr., G. B. Aboutanos, B. M. Dawant, S. Gadamsetty, R. A. Margolin, R. J. Maciunas and J. M. Fitzpatrick, "Effect of geometrical distortion correction in MR on image registration accuracy," *Journal of Computer Assisted Tomography* **20** (4), 666-79 (1996).

39 P. Munger. "Accuracy Considerations in MR Image-guided Neurosurgery," M.Sc., McGill University, 1994.

40 J. West, J. M. Fitzpatrick, M. Y. Wang, B. M. Dawant, C. R. Maurer, Jr., R. M. Kessler, R. J. Maciunas, C. Barillot, D. Lemoine, A. Collignon, F. Maes, P. Suetens, D. Vandermeulen, P. A. van den Elsen, S. Napel, T. S. Sumanaweera, B. Harkness, P. F. Hemler, D. L. Hill, D. J. Hawkes *et al.*, "Comparison and evaluation of retrospective intermodality brain image registration techniques," *Journal of Computer Assisted Tomography* **21** (4), 554-66 (1997).

- 41 Y. L. Yamamoto, C. J. Thompson, M. Diksic, E. Meyer and W. H. Feindel, "Positron emission tomography," *Neurosurgical Review* **7** (4), 233-52 (1984).
- 42 A. Hartov, S. D. Eisner, D. W. Roberts, K. D. Paulsen, L. A. Platenik and M. I. Miga, "Error analysis for a free-hand three-dimensional ultrasound system for neuronavigation," *Neurosurgical Focus* **6** (3), Article 5 (1999).
- 43 R. M. Comeau, A. Fenster and Peters T. M., "Intraoperative US in Interactive Image-guided Neurosurgery," *Radiographics* **17** (4), 1019-1027 (1998).
- 44 J. Koivukangas, Y. Louhisalmi, J. Alakuijala and J. Oikarinen, "Ultrasound-controlled neuronavigator-guided brain surgery," *Journal of Neurosurgery* **79** (1), 36-42 (1993).
- 45 J. W. Trobaugh, W. D. Richard, K. R. Smith and R. D. Bucholz, "Frameless stereotactic ultrasonography: Method and applications," *Computerized Medical Imaging & Graphics* **18**, 235-246 (1994).
- 46 C. Giorgi and D. S. Casolino, "Preliminary clinical experience with intraoperative stereotactic ultrasound imaging," *Stereotactic & Functional Neurosurgery* **68** (1-4 Pt 1), 54-8 (1997).
- 47 R Rohling, A Gee and Berman L, "Automatic registration of 3D ultrasound images," *Ultrasound in Medicine and Biology* **24** (6), 841-854 (1998).
- 48 J. M. Fitzpatrick, J. B. West and C. R. Maurer Jr., "Predicting Error in Rigid-Body Point Based Registration," *IEEE Transactions on Medical Imaging* **17** (5), 694-702 (1998).

49 M. A. Audette, K. Siddiqi and T. M. Peters, "Level-Set Surface Segmentation and Fast Cortical Range Tracking for Computing Intrasurgical Deformations," MICCAI'99 **1679**, 788-797 (1999).

50 K. S. Arun, T. S. Huang and S. D. Blostein, "Least-Squares Fitting of Two 3-D Point Sets," IEEE Transactions of pattern Analysis and Machine Intelligence **PAMI-9** (5), 698-700 (1987).

51 E. Cuchet, J. Knoploch, D. Dormont and C. Marsault, "Registration in neurosurgery and neuroradiotherapy applications," Journal of Image Guided Surgery **1** (4), 198-207 (1995).

52 M. S. Alp, M. Dujovny, M. Misra, F. T. Charbel and J. I. Ausman, "Head registration techniques for image-guided surgery," Neurological Research **20** (1), 31-7 (1998).

53 S Schreiner, J. T. Lewis, G. S. Allen and R. L. Jr. Galloway, "Technique for the three-dimensional localization of implanted fiducial markers," Proceedings of SPIE The International Society for Optical Engineering **2431**, Photo-Optical (1995).

54 C. R. Maurer, Jr., J. M. Fitzpatrick, M. Y. Wang, R. L. Galloway, Jr., R. J. Maciunas and G. S. Allen, "Registration of head volume images using implantable fiducial markers," IEEE Transactions on Medical Imaging **16** (4), 447-62 (1997).

55 J. T. Lewis, R. L. Galloway, Jr. and S. Schreiner, "An ultrasonic approach to localization of fiducial markers for interactive, image-guided neurosurgery--Part I: Principles," IEEE Trans Biomed Eng **45** (5), 620-30 (1998).

56 C. R. Maurer, Jr., J. M. Fitzpatrick, M. Y. Wang, R. L. Galloway, Jr., R. J. Maciunas and G. S. Allen, "Registration of head volume images using implantable fiducial markers," *IEEE Transactions on Medical Imaging* **16**, 447-462 (1997).

57 F. C. Vinas, L. Zamorano, R. Buciu, Q. H. Li, F. Shamsa, Z. Jiang and F. G. Diaz, "Application accuracy study of a semipermanent fiducial system for frameless stereotaxis," *Computer Aided Surgery* **2** (5), 257-63 (1997).

58 M. A. Howard, 3rd, M. B. Dobbs, T. M. Simonson, W. E. LaVelle and M. A. Granner, "A noninvasive, reattachable skull fiducial marker system. Technical note," *Journal of Neurosurgery* **83** (2), 372-6 (1995).

59 R. J. Bale, M. Vogele, W. Freysinger, A. R. Gunkel, A. Martin, K. Bumm and W. F. Thumfart, "Minimally invasive head holder to improve the performance of frameless stereotactic surgery," *Laryngoscope* **107** (3), 373-7 (1997).

60 P. J. Edwards, A. P. King, C. R. Maurer Jr., D. A. de Cunha, D. J. Hawkes, D. L. G. Hill, R. P. Gaston, M. R. Fenlon, S. Chandra, A. J. Strong, C. L. Chandler, A. Richards and M. J. Gleeson, "Design and Evaluation of a System for Microscope-Assisted Guided Interventions," *MICCAI '99* **1679**, 842-851 (1999).

61 T. Peters, B. Davey, P. Munger, R. Comeau, Evans A. and A. Olivier, "Three-Dimensional Multimodal Image-Guidance for Neurosurgery," *IEEE Transactions on Medical Imaging* **15** (2), 121-128 (1996).

62 H. Hirschberg and O. J. Kirkeby, "Interactive image directed neurosurgery: patient registration employing the Laitinen stereo-adaptor," *Minimally Invasive Neurosurgery* **39** (4), 105-7 (1996).

63 T. M. Peters, R. Comeau, P. Munger, B. L. K. Davey, L. Pisani, A. Sadikot and A. Olivier, "Image-guided Neurosurgery at the Montreal Neurological Institute," Proceedings of the Annual International Conference of the IEEE Engineering in Medicine and Biology, **2**, 635-636 (1996).

64 W. E. L. Grimson, G. J. Ettinger, S. J. White, T. Lozano-Perez, W. M. Wells, III and R. Kikinis, "An automatic registration method for frameless stereotaxy, image guided surgery, and enhanced reality visualization," IEEE Transactions on Medical Imaging **15** (2), 129-40 (1996).

65 R. Evans, "VISLAN computer-aided surgery," IEEE Review **41**, 51-54 (1995).

66 B. A. Kall, S. J. Goerss, S. O. Stiving, D. H. Davis and P. J. Kelly, "Quantitative analysis of a noninvasive stereotactic image registration technique," Stereotactic & Functional Neurosurgery **66** (1-3), 69-74 (1996).

67 S. Nakajima, H. Atsumi, R. Kikinis, T. M. Moriarty, D. C. Metcalf, F. A. Jolesz and P. M. Black, "Use of cortical surface vessel registration for image-guided neurosurgery," Neurosurgery **40** (6), 1201-8; discussion 1208-10 (1997).

68 J. West, M. Fitzpatrick, M. Y. Wang, B. M. Dawant, C. R. Maurer, Jr., R. M. Kessler, R. J. Maciunas, C. Barillot, D. Lemoine, A. Collignon, F. Maes, P. Suetens, D. Vandermeulen, P. A. van den Elsen, S. Napel, T. S. Sumanaweera, B. Harkness, P. F. Hemler, D. L. G. Hill, D. J. Hawkes *et al.*, "Comparison and evaluation of retrospective intermodality brain image registration techniques," Journal of Computer Assisted Tomography **21** (4), 554-66 (1997).

69 C. R. Maurer, M. Fitzpatrick, M. Y. Wang and R. J. Maciunas, "Correction of geometrical distortion MR image registration," Proceedings of the Annual Conference on Engineering in Medicine and Biology. Publ by IEEE, IEEE Service Center, Piscataway, NJ, USA **15**, 122-123 (1993).

70 A. Olivier, "Surgery of epilepsy: methods," Acta Neurologica Scandinavica. Supplementum **117**, 103-113 (1988).

71 D. L. G. Hill, C. R. Maurer, R. J. Maciunas, J. A. Barwise, J. M. Fitzpatrick and M. Y. Wang, "Measurement of Intraoperative Brain Surface Deformation under a Craniotomy," Neurosurgery **43** (3), 514-28 (1998).

72 D. W. Roberts, A. Hartlov, F. E. Kennedy, M. I. Miga and K. D. Paulsen, "Intraoperative Brain Shift and Deformation: A Quantitative Analysis of Cortical Displacement in 28 Cases," Neurosurgery **43** (4), 749-760 (1998).

73 A. Hamadeh, S. Lavallee and P. Cinquin, "Automated 3-dimensional computed tomographic and fluoroscopic image registration," Computer Aided Surgery **3** (1), 11-19 (1998).

74 A. Gueziec, P. Kazantzides, B. Williamson and R. H. Taylor, "Anatomy-based registration of CT-scan and intraoperative X-ray images for guiding a surgical robot," IEEE Transactions on Medical Imaging **17** (5), 715-28 (1998).

75 T. C. Kriss and V. M. Kriss, "History of the operating microscope: from magnifying glass to microneurosurgery," Neurosurgery **42** (4), 899-907; discussion 907-8 (1998).

76 L. J. Zamorano, L. Nolte, A. M. Kadi and Z. Jiang, "Interactive intraoperative localization using an infrared-based system," *Neurol Res* **15** (5), 290-8 (1993).

77 D.W. Roberts, J.W. Strohbehn, J.F. Hatch, W Murray and H. Kettenberger, "A frameless stereotaxic integration of computerized tomographic imaging and the operating microscope.." *Journal of Neurosurgery* **65** (4), 545-549 (1986).

78 N. Kiya, C. Dureza, T. Fukushima and J. C. Maroon, "Computer navigational microscope for minimally invasive neurosurgery," *Minim Invasive Neurosurg* **40** (3), 110-5 (1997).

79 L. J. Pisani, R. Comeau, B. L. K. Davey and T. M. Peters, "Incorporation of stereoscopic video into an image-guided neurosurgery environment". Proceedings of the 17th Annual Conference on Engineering in Medicine and Biology. Publ by IEEE, IEEE Service Center, Piscataway, NJ, USA 365-6 (1995).

80 W. E. Butler, C. M. Piaggio, C. Constantinou, L. Niklason, R. G. Gonzalez, G. R. Cosgrove and N. T. Zervas, "A mobile computed tomographic scanner with intraoperative and intensive care unit applications," *Neurosurgery* **42** (6), 1304-10; discussion 1310-1 (1998).

81 C. R. Wirtz, V. M. Tronnier, M. M. Bonsanto, M. Knauth, A. Staubert, F. K. Albert and S. Kunze, "Image-guided neurosurgery with intraoperative MRI: update of frameless stereotaxy and radicality control," *Stereotactic & Functional Neurosurgery* **68** (1-4 Pt 1), 39-43 (1997).

82 P. M. Black, T. Moriarty, E. Alexander, 3rd, P. Stieg, E. J. Woodard, P. L. Gleason, C. H. Martin, R. Kikinis, R. B. Schwartz and F. A. Jolesz, "Development and

implementation of intraoperative magnetic resonance imaging and its neurosurgical applications," *Neurosurgery* **41** (4), 831-42; discussion 842-5 (1997).

83 C. R. Maurer Jr., D. L. G. Hill, A. J. Martin, H. Liu, M. McCue, D. Rueckert, D. Lloret, W. A. Hall, R. E. Maxwell, D. J. Hawkes and C. L. Truwit, "Investigation of Intraoperative Brain Deformation Using a 1.5T Interventional MR System: Preliminary Results," *IEEE Transactions on Medical Imaging* **17** (5), 817-825 (1998).

84 G. R. Sutherland, T. Kaibara, D. Louw, D. I. Hoult, B. Tomanek and J. Saunders, "A mobile high-field magnetic resonance system for neurosurgery," *Journal of Neurosurgery* **91** (5), 804-13 (1999).

85 G. J. Dohrmann and J. M. Rubin, "Dynamic intraoperative imaging and instrumentation of brain and spinal cord using ultrasound," *Neurol Clin* **3** (2), 425-37 (1985).

86 L. M. Auer and V. van Velthoven, "Intraoperative ultrasound (US) imaging. Comparison of pathomorphological findings in US and CT," *Acta Neurochir* **104** (3-4), 84-95 (1990).

87 L. M. Auer, "Ultrasound stereotaxic endoscopy in neurosurgery," *Acta Neurochir Suppl* **54**, 34-41 (1992).

88 J. Godard, G. Jacquet, R. Steimle and A. Czorny, "[Peroperative echography in neurosurgery. Its value and applications 10 years later]," *Neurochirurgie* **39** (3), 182-7 (1993).

- 89 A. Gronningsaeter, G. Unsgard, S. Ommedal and B. A. Angelsen, "Ultrasound-guided neurosurgery: a feasibility study in the 3-30 MHz frequency range," *Br J Neurosurg* **10** (2), 161-8 (1996).
- 90 P. M. Jokich, J. M. Rubin and G. J. Dohrmann, "Intraoperative ultrasonic evaluation of spinal cord motion," *J Neurosurg* **60** (4), 707-11 (1984).
- 91 J. E. Knake, R. A. Bowerman, T. M. Silver and S. McCracken, "Neurosurgical applications of intraoperative ultrasound," *Radiol Clin North Am* **23** (1), 73-90 (1985).
- 92 P. Kumar, R. Sukthankar, B. J. Damany, J. Mishra and A. N. Jha, "Evaluation of intraoperative ultrasound in neurosurgery," *Ann Acad Med Singapore* **22** (3 Suppl), 422-7 (1993).
- 93 K. Yamakawa, T. Kondo, M. Yoshioka and K. Takakura, "Application of superfine fiberscope for endovasculectomy, ventriculoscopy, and myeloscapy." *Acta Neurochir Suppl* **54**, 47-52 (1992).
- 94 B. L. Bauer and D. Hellwig, "Minimally invasive endoscopic neurosurgery--a survey," *Acta Neurochirurgica - Supplementum* **61**, 1-12 (1994).
- 95 L. W. Harris, "Endoscopic techniques in neurosurgery," *Microsurgery* **15** (8), 541-6 (1994).
- 96 D. Hellwig, L. Benes, H. Bertalanffy and B. L. Bauer, "Endoscopic stereotaxy--an eight year's experience," *Stereotactic & Functional Neurosurgery* **68** (1-4 Pt 1), 90-7 (1997).

- 97 R. L. Galloway, Jr., W. A. Bass, H. Senel and S. Schreiner, "Enhanced interactive surgical guidance using both preoperative and intraoperative imaging," Proceedings of SPIE The International Society for Optical Engineering. Publ by Society of Photo Optical Instrumentation Engineers, Bellingham, WA, USA **1897**, 69-77 (1993).
- 98 J. C. Chen, K. Moffitt and M. L. Levy, "Head-mounted display system for microneurosurgery," *Stereotactic & Functional Neurosurgery* **68** (1-4 Pt 1), 25-32 (1997).
- 99 N. L. Dorward, O. Alberti, B. Velani, F. A. Gerritsen, W. F. Harkness, N. D. Kitchen and D. G. Thomas, "Postimaging brain distortion: magnitude, correlates, and impact on neuronavigation," *Journal of Neurosurgery* **88** (4), 656-62 (1998).
- 100 M. Audette and T. M. Peters, "Level-set segmentation and registration for computing intrasurgical deformations.," *SPIE Image Processing* **3661** (1999).
- 101 R. D. Bucholz, D. D. Yeh, J. Trobaugh, L. L. McDurmont, C. D. Sturm, C. Baumann, J. M. Henderson, A. Levy and P. Kessman, "The correction of stereotactic inaccuracy caused by brain shift using an intraoperative ultrasound device." CVRMed MRCAS '97. First Joint Conference, Computer Vision, Virtual Reality and Robotics in Medicine and Medical Robotics and Computer Assisted Surgery Proceedings. Springer Verlag (1997).
- 102 P. J. Edwards, D. L. Hill, J. A. Little and D. J. Hawkes, "A three-component deformation model for image-guided surgery," *Medical Image Analysis* **2** (4), 355-67 (1998).

103 M. J. Miga, K. D. Paulsen, J. M. Lemery, S. D. Eisner, A. Hartov, F. E. Kennedy and D. W. Roberts, "Model-Updated Image guidance: Initial Clinical Experiences with Gravity-Induced Brain Deformation," *IEEE Transactions on Medical Imaging* (1999).

104 Fred L. Bookstein, "Principal warps: Thin-plate splines and the decomposition of deformations," *IEEE Transactions on Pattern Analysis & Machine Intelligence*. p 11 (6), 567-585 (1989).

105 F.W Kremkay, *Diagnostic Ultrasound Principles and Instruments* (W.B. Saunders Company, Philadelphia, 1993), pp. 411.

106 J. W. Trobaugh, P. Kessman, D. Dietz and R. Bucholz, "Ultrasound in image fusion: A framework and applications," *Proceedings of the IEEE Ultrasonics Symposium* 2, 1393-1396 (1997).

107 P. R. Detmer, G. Bashein, T. Hodges, K. W. Beach, E. P. Filer, D. H. Burns and D. E. Strandness, Jr., "3D ultrasonic image feature localization based on magnetic scanhead tracking: in vitro calibration and validation," *Ultrasound in Medicine & Biology* 20 (9), 923-36 (1994).

108 R. W. Prager, R. N. Rohling, A. H. Gee and L. Berman, "Rapid calibration for 3-D freehand ultrasound," *Ultrasound in Medicine & Biology* 24 (6), 855-69 (1998).

109 J. Foley, A. van Dam, S. Feiner and J. Hughes, "Parametric Cubic Curves," in *Computer Graphics Principles and Practice*, edited by K. Wollman (Addison Wesley, Don Mills, ON,), pp. 478-516(1990).

110 D. W. Roberts, M. I. Miga, A. Hartlov, S. Eisner, J. M. Lemery, F. E. Kennedy and K. D. Paulsen, "Intraoperatively Updated Neuroimaging Using Brain Modeling and Sparse Data," *Neurosurgery* **45** (5), 1199-1207 (1999).

111 K.C. Chu and B.K. Rutt, "Polyvinyl alcohol cryogel: an ideal phantom material for MR studies of arterial flow and elasticity," *Magnetic Resonance in Medicine* **37** (2), 314-19 (1997).

112 F.W. Kremkau, in *Diagnostic Ultrasound Principles and Instruments* (W.B. Saunders Company, Philadelphia), pp. 18 (1993).

113 M. M. Goodsitt, P. L. Carson, S. Witt, D. L. Hykes and J. M. Kofler, Jr., "Real-time B-mode ultrasound quality control test procedures Report of AAPM Ultrasound Task Group No. 1," *Medical Physics* **25** (8), 1385-406 (1998).

114 R.M. Comeau, D.G. Gobbi, A. Fenster, A.F. Sadikot and T.M. Peters, "Detecting and Correcting Brain Tissue Deformation Using Intra-Operative Ultrasound Imaging in Interactive Image Guided Neurosurgery," presented at the 44th Annual Scientific Meeting of the Canadian Organization of Physicists in Medicine, London, Ontario, 1998.

115 A. C. Bastos, R. M. Comeau, D. Melancon, D. Tampieri, F. Dubeau, T. Peters and F. Andermann, "Image analysis of gyral architecture in cortical dysgenesis by using curvilinear reformatting of 3D MRI," presented at the Annual Meeting of the American Epilepsy Society, Boston, Massachusetts, 1997.

116 P. Neelin, J. Crossman, D. Hawkes, Y. Ma and A.C. Evans, "Validation of an MRI/PET Landmark Registration Method Using 3D Simulated PET Images and Point Simulations," *Computerized Medical Imaging and Graphics* **17** (4), 351-356 (1993).

117 R Sibson, "Studies in the Robustness of Multidimensional Scaling: Procrustes Statistics," *J. R. Statist. Soc. B.* **40** (2), 134-238 (1978)

118 G.H. Golub and C. F. Van Loan, "Matrix Computations," in *Matrix Computations*, (JHNU Press, 1996), Vol. 1, pp. 425-426.